Ytterbium Atom Interferometry Within an Optical Lattice

Tahiyat Rahman

A dissertation
submitted in partial fulfillment of the
requirements for the degree of

Doctor of Philosophy

University of Washington

2025

Reading Committee:

Subhadeep Gupta, Chair

Boris Blinov

Sara Mouradian

Program Authorized to Offer Degree:
Physics

University of Washington

Abstract

Ytterbium Atom Interferometry Within an Optical Lattice

Tahiyat Rahman

Chair of the Supervisory Committee:
Job and Gertrude Tamaki Endowed Chair Subhadeep Gupta
Department of Physics

Matterwave interferometers utilizing atoms and optical lattices are subject to the instabilities and systematics associated with lattice dynamics. We apply a Bloch band approach to atom optics to understand the systematic effects on interferometric phases. In particular, we examine the effects of the coherent quantum passage of atoms accelerating in different lattice bands—also known as Bloch oscillations—in a vertically oriented optical lattice for atom interferometry. This work details observations of multi-path Landau-Zener-Stückelberg-Majorana interference effects, used to measure phases *within* an optical lattice due to Bloch oscillations. We expound on their relevance towards next-generation atom interferometers employing many Bloch oscillations for improved sensitivity. Optical lattices are also a promising tool for trapped atom interferometry, the matterwave analog for optical interferometry with fiber optics. We demonstrate the first lattice-trapped atom interferometer with a Bose-Einstein condensate. The effect of the choice of band on the visibility of lattice-trapped interferometers has been hitherto unexplored. We show improvements in the visibility of the interferometer fringes by trapping at the so-called “magic depths” of excited bands, where lattice-induced phases are first-order insensitive to variations in lattice depth. We showcase excited-band lattice-trapped interferometers and trapped interferometers for ytterbium for the first time and use them for gravitational sensing.

ACKNOWLEDGMENTS

If I have ever come off as rebellious, it's because I needed to question everything. This thesis is dedicated to all those who were gracious enough to allow me to question. It was only possible to reach this milestone with a tremendous amount of support. Without the nourishment of my curiosity, I don't believe my spirit could have survived the weathering of a Ph.D. program.

In the lab, I had the privilege of meeting many wonderful coworkers and colleagues. I was welcomed by Katie McAlpine and Daniel Gochnauer who were senior graduate students at the time. I thank them for being patient with me and for teaching me about atom interferometry and the experimental apparatus. I've also been privileged to work alongside two brilliant and talented junior graduate student workers during my time here, Anna Wirth-Singh and Emmett Hough. There were many undergraduates and post-bachelor students that I've had a prominent role in mentoring, including Aidan Kemper, Andrew Ivanov, Charles Skinner, Aruku Senoo, and Pasha Bullock, who have since moved on to bigger things. Finally, I need to thank my advisor, Subhadeep Gupta, or Deep for short. Deep has been a driving force throughout my Ph.D. and really helped me come into my own as a researcher and learn to contain my curiosity for productive research. He left an impact on how I investigate and diagnose questions that come up during day-to-day research and lab work.

There are also so many outside my research program that have made this possible. I've had a lot of fulfillment volunteering as a union organizer to secure improved rights for researchers and teaching assistants at the University of Washington. Working alongside other conscientious colleagues has been a very exhilarating experience. I felt that I was doing my part in improving the working conditions of researchers and teaching assistants, and it was wonderful to meet and work with such thoughtful, passionate, and prescient people along the way. At the present time, I feel that there is a growing resurgence in academia that these issues are of primary importance.

I would not have been able to do this without my family and loved ones. My parents have always been supportive of my curiosity, albeit even when my rebelliousness was not always welcome. But fundamentally, they always believed in my potential. My brothers shared a lot of the wonder I have for the world, and it was always a pleasure to explain physical phenomena as plainly as possible. My sister and I had camaraderie as we battled through our respective graduate programs. Dispirited by loss and grief, I am empowered again through my loved ones and colleagues.

Studying physics and doing research is an incredibly humbling experience. Research often felt as if I was making a continuous series of mistakes and somehow miraculously arriving at a correct—or rather correct enough—conclusion. A simple minus sign, a factor of π, a plumbing mishap, or even one loose electrical connection is all it takes for you to confront your own ignorance. Above all, I learned to be okay with stepping into the unknown, without having all of the answers. Thankfully, I didn't have to step into it alone.

TABLE OF CONTENTS

LIST OF FIGURES

GLOSSARY OF ACRONYMS

AO(M): Acousto-optic modulator

BEC: Bose-Einstein condensate

BO: Bloch oscillation—a method for large momentum transfer.

DDS: Digital direct synthesizer—used to generate radio frequency waveforms with frequency and amplitude control.

ECDL: External cavity diode laser, typically in a Littrow configuration.

LMT: Large momentum transfer—a class of techniques used to increase the sensitivity of atom interferometric measurements by increasing the space-time area enclosed by interferometer arms.

LTAI: Lattice-trapped atom interferometry

MLTAI: Magic lattice-trapped atom interferometry

MOT: Magneto-optical trap

MPSI: Multi-path Stückelberg interferometry

ODT: Optical dipole trap, typically used in pairs in either a folded or orthogonal configuration.

X-BEAM: Second stage laser cooling in a crossed configuration.

Chapter 1

INTRODUCTION

1.1 Quantum Interference (What Is It Good For)?

Interference is a ubiquitous phenomenon of nature, with often stunning and counter-intuitive behaviors. Interference allows for waves to be greater than the sum of their parts. This is seen from the trivial example of the sum of two electric field plane waves $\mathbf{E} = E_0 \exp(-ikx)\hat{x}$. While each field has peak intensity $|E_0|^2$, the sum has a total peak intensity of $4|E_0|^2$. At first glance, this appears to be an odd example of $1 + 1 = 4$, but this is simply a consequence of electric fields obeying a wave equation, which allows for linear superposition[1]. Just as there can be constructive interference where the total intensity is greater than the sum of its parts, there can also be destructive interference where the total field is less.

Famously, Young's double slit experiment confirmed the electromagnetic wave behavior of light through the interference fringes of waves traveling on different paths. Later, the wave behavior of quantum matter, such as electrons or neutrons, was established through interference experiments [1, 2]. Indeed, this is a consequence of the fact that massive quantum particles obey the dynamics of another wave equation (the Schrödinger equation). Consequently, massive particles behave as de Broglie waves $\psi \sim \exp(-ipx/\hbar)$, where $[\hat{x}, \hat{p}] = i\hbar$ is the canonical commutation relation. Here, the square norm of the wavefunction $|\psi|^2$ is interpreted as the probability density. Therefore, interference fringes for matterwaves are observed as the periodic modulation in the likelihood of the particle's position or momentum. But what can we do with it?

---

[1] Don't worry, we have not created free energy! The energy of a simple harmonic oscillator needed to generate the superposition would need to quadruple compared to the oscillator for one of those waves—not double. There are no perpetual motion machines.

An interferometer is a device that exploits the interference behavior of waves to detect a fringe pattern. The fringe pattern—its period and phase—is sensitive to changes in the different paths that waves propagate through before interfering. Therefore, by detecting a fringe, we measure the differential effect on the interfering waves due to the local environment and the diffraction gratings. For example, laser interferometers have been used to confirm the existence of gravitational waves [3], measured through the different length contraction between the interferometer paths. Similarly, atom interferometers have been used to measure inertial effects [4] to sensitively measure forces [5], gravitational acceleration [6], and perform tests of fundamental physics [7, 8, 9].

1.2 Light-Pulse Atom Interferometry

The first atom interferometers consisted of thermal atoms passing through diffractive elements, such as nano-fabricated gratings [10, 11] or optical pulses [12]. The latter is called a light-pulse atom interferometer, such as when pulsed optical lattices are pulsed on to diffract atoms. Optical lattices are a good example of electromagnetic interference. We generate them by manipulating two counterpropagating laser beams of the same frequency. The electric field forms a standing wave, which is a periodic intensity profile—a diffraction grating for atoms.

To understand how we make precise measurements with atom interferometers, consider how you would measure the thickness of a sheet of paper. Certainly, you would need a very fine ruler to be able to do so. Not only that, you could stack $N \gg 1$ identical sheets of paper together and measure the thickness of the pile of paper. After dividing your measurement by N, you could tell me how thick one sheet is on average. Of course, there is some imprecision in the measurement because the sheets are not completely identical to each other.

Lasers, with their coherent and monochromatic light, provide us with excellent rulers for our atoms. Our optical lattices have a ruler spacing $d \approx 278\,\mathrm{nm}$, corre-

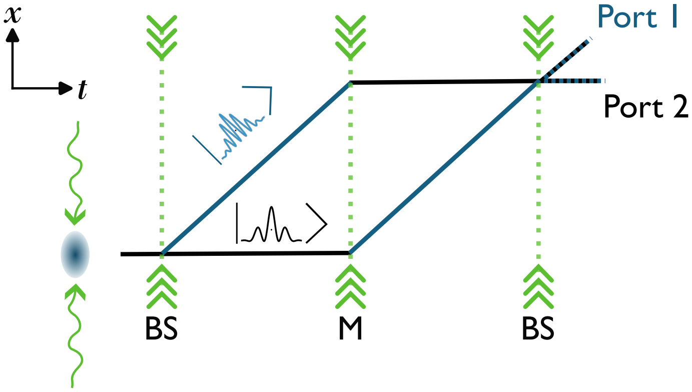

Figure 1.1: A simple example of a light pulse atom interferometer space-time diagram. Left: Laser beams of similar frequency are used to construct an optical lattice, which diffracts atomic matterwaves in an atom cloud. Right: The light pulses split the matterwave into several paths using beamsplitters (BS). This Mach-Zehnder interferometer scheme also has a mirror (M) pulse. Ports 1 and 2 contain a combination of the interfering paths.

sponding to 2π phase difference. Of course, a ruler is only as precise as the size of the object you measure, but cold atom gas clouds can have large thermal de Broglie wavelengths $\lambda_{\mathrm{db}} \sim 1/T^{3/2}$, where T is the temperature of thermal atoms. For all of our experiments, we use Bose-Einstein condensates, which are macroscopic quantum coherent states with $\sim 50\,\mu$m cloud sizes. The coherence of the laser light and the coherence of the matterwave go hand in hand for precision measurements. Chapter 2 contains information about this and other experimental details. We illustrate a basic interferometer diagram in Fig. 1.1 showing the matterwave split into different paths and interfering at the output ports.

Light-pulsed atom interferometers are sensitive to the phase difference

$$\Phi \approx \phi_{\mathrm{prop}} + \phi_{\mathrm{laser}} \,, \tag{1.1}$$

where the total phase Φ has two main contributions. The first ϕ_{prop}, is due to the difference in wave propagation. The laser phase is due to the change in phase of the optical lattice grating. The key to sensitive measurements with a light-pulsed interferometer is to use the laser phase to cancel out the propagation phase with high precision. The uncertainty in how well we can nullify the phase $\delta\phi$, together with the propagation phase, gives us a phase imprecision $\delta\phi/\phi_{\text{prop}}$—which we would like to be small. The strategy for precision measurements always involves reducing $\delta\phi$ and increasing ϕ_{prop}. Firstly, since phase is periodic modulo 2π we require $\delta\phi \ll \pi$ to be able to observe a fringe. This also means that $\phi_{\text{prop}} = 2\pi \times N + \theta$, where $\theta = \phi_{\text{prop}} \bmod 2\pi$ and N is the number of full fringe periods. For a high-resolution measurement, we require N to be large, i.e., we need a large propagation phase.

A paradigmatic example of a light-pulse atom interferometer shown in Fig. 1.1 is a Mach-Zehnder interferometer. For a vertically oriented lattice, the beamsplitter diffracts the atoms against the direction of gravity, splitting the matterwave into a superposition of $|p_0 + \hbar k_{\text{eff}}\rangle$ and $|p_0\rangle$ momentum for the respective top and bottom paths. The phase for the Mach-Zehnder geometry is $\Phi = k_{\text{eff}} g T^2 - \alpha T^2$ where the first and second terms correspond to the propagation and laser phases, respectively. The frequency chirp $\alpha = 2k \cdot a_{\text{lat}}$ controls the laser phase of a lattice with wavenumber $k = \pi/d$ accelerating at a_{lat}. In this way, gravity is determined by precisely balancing the phase due to propagation for an interferometer time T in a uniform gravitational field of strength g with the laser phase.

1.2.1 Large momentum transfer with Bloch oscillations

One class of techniques for increasing the propagation phase is called large momentum transfer. These involve imparting a large acceleration in one of the interferometer arms relative to the other, increasing k_{eff} and the space-time area inside the interferometer. The result is a larger propagation phase, if not simply because the matterwaves in different paths experience larger separations for the same amount of time. For example, large momentum transfer techniques have been used to precisely test the weak equivalence principle < 10 ppt in dual atom interferometers [7].

One method for large momentum transfer utilizes Bloch oscillations (BOs) in an optical lattice [13, 14]. Bloch oscillations happen when particles in optical lattices experience a constant external force. BOs have become a powerful tool in quantum metrology. For example, local gravity measurements [15] and equivalence principle tests [16] rely on sensing an external force through measurement of the Bloch oscillation frequency. Bloch oscillations have also been implemented in atom interferometers for tests of quantum electrodynamics [8, 17], where two interferometers are accelerated with equal and opposite Bloch oscillation pulses to achieve < 100 ppt measurement of the fine structure constant.

However, Bloch oscillations come with systematics that affect each interferometer phase similarly. Those systematic shifts can be made common-mode among two interferometers, so they are canceled up to first order. The implementation of BOs as large momentum transfer optics has been limited when used for a single interferometer. In Chapter 3, we observe multi-path Landua-Zener-Stückelberg-Majorana interference resulting from atomic matterwaves traversing through more than one Bloch band. Using this interference effect, we probe the coherence of many Bloch oscillations, crucial for large momentum transfer applications because successive Bloch oscillations transfer more units of momentum.

1.3 Bloch-Band Picture for Atom-optics

We find it useful to consider the dynamics of atoms in optical lattices through a Bloch band approach. What happens when you put an electron in an ionic crystal and apply a constant electric field gradient? This question led Felix Bloch to the discovery of Bloch oscillations. In general, quantum particles inside a periodic potential are, as Bloch put it [18], "de Broglie waves which are modulated in the rhythm of the lattice." In our case, we have neutral ytterbium atoms in an optical lattice.

For a simple 1D case, we consider a periodic potential with average intensity $U_0/2$

for a particle with mass m. The Schrödinger eq is:

$$E\psi = \left(\frac{-\hbar^2}{2m} \frac{d^2}{dx^2} + \frac{U_0}{2} \cos(2kx) \right) \psi \, , \tag{1.2}$$

$$\psi(x) = u(x) \exp(-iqx) \, , \tag{1.3}$$

where we used the Ansatz (1.3) as suggested by Bloch. The envelope for the de Broglie wave $\exp(iqx)$, is periodic $u_q(x) = u_q(x+d)$, where $d = \pi/k$ is the spatial periodicity of the lattice. Plugging (1.3) into (1.2) results in

$$\begin{aligned} Eu(x)e^{-iqx} &= \frac{U_0}{4} u(x) e^{-i(q-2k)x} + \frac{U_0}{4} u(x) e^{-i(q+2k)x} \\ &+ \frac{\hbar^2 q^2}{2m} u(x) e^{-iqx} - e^{-iqx} \frac{\hbar^2}{2m} \frac{d^2}{dx^2} u + iq e^{-iqx} \frac{\hbar^2}{m} \frac{d}{dx} u \, . \end{aligned} \tag{1.4}$$

Then, after we integrate in space, which takes a Fourier transform—we arrive at

$$\begin{aligned} Ea(q) &= \frac{U_0}{4} a(q-2k) + \frac{U_0}{4} a(q+2k) \\ &+ \frac{\hbar^2 q^2}{2m} a(q) - \frac{(iq)^2 \hbar^2}{2m} a(q) + (iq)^2 \frac{\hbar^2}{m} a(q) \, , \end{aligned} \tag{1.5}$$

where $a(q)$ are the Fourier amplitudes of $u(x)$ and the last three terms sum to zero. It appears that the energy of de Broglie waves $|k\rangle$ that are $2k$ apart in wavenumber couple to each other. We can then rewrite the solutions of the Bloch wavefunctions as $|\psi\rangle = \sum_b a_b(q) \, |q + 2nk\rangle$ where we require $-1 < q < 1$ so as not to have redundant states. Plugging back into (1.2) we get that the Hamiltonian is $\hat{H} = \sum_n \hat{H}_n(q)$, where each term is given by

$$\begin{aligned} \hat{H}_n(q) = \frac{U_0}{4} \, & |q + 2(n+1)k\rangle \langle q + 2nk| \\ & + \frac{U_0}{4} \, |q + 2(n-1)k\rangle \langle q + 2nk| \\ & \qquad + \frac{\hbar^2 (q + 2nk)^2}{2m} \, |q + 2nk\rangle \langle q + 2nk| \, . \end{aligned} \tag{1.6}$$

Figure 1.2 shows the first few eigenenergies $E_b(q)$, known as Bloch bands, where we have redefined $q \to \hbar q$ as the "crystal momentum" or "quasimomentum". A useful energy scale for Bloch bands is $E_r \equiv \hbar^2 k^2 / (2m)$, called the "recoil energy".

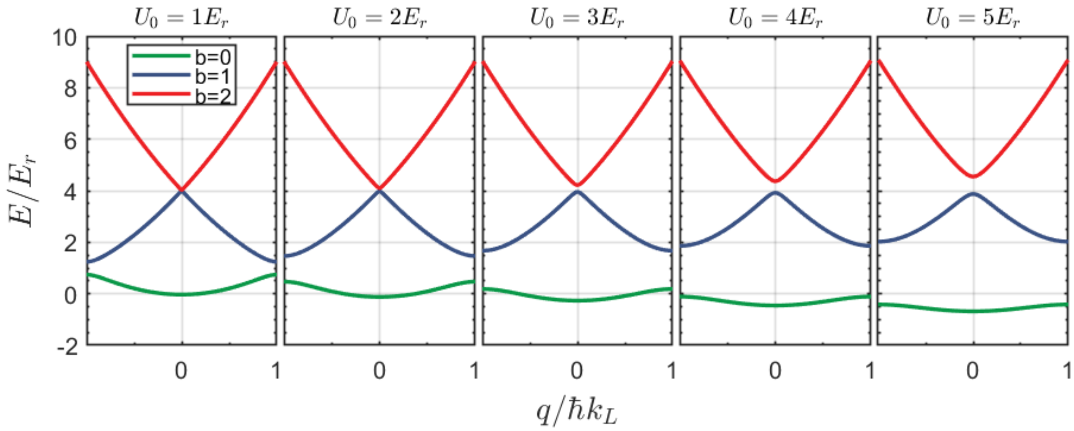

Figure 1.2: The first three Bloch bands $b = 0$–2, for atom-optics with varying lattice depth U_0. From left to right: $U_0/E_r = 1$–5 in ascending order. Gaps between bands form at the avoided crossings, and bandgaps grow monotonically with the lattice depth.

1.3.1 *Limiting cases in lattice depth*

I've found it helpful to consider the limiting cases of the Bloch band picture for small and large lattice depths to guide our intuition. Let's consider the simple case of a two-level system of just the first two bands with coupling terms $U_0/4$ whose energy bands are exactly solvable. The Hamiltonian represented in the free-particle basis in the center of mass frame is

$$\hat{H} = E_r \begin{pmatrix} \delta/2 & \epsilon/2 \\ \epsilon/2 & -\delta/2 \end{pmatrix} , \tag{1.7}$$

where we have defined $\epsilon \equiv (U_0/2)/E_r$ and $\delta \equiv 2[q/(\hbar k) + 1]$. The energy bands are exactly solvable

$$E_\pm(q) = \pm\frac{E_r}{2}\sqrt{\delta^2(q)^+\epsilon^2} , \tag{1.8}$$

and we will particularly look for solutions for which $\delta(q) \to 0$ where the energy levels would cross if not for the coupling arising from the perturbation ϵ. Then the bandgap

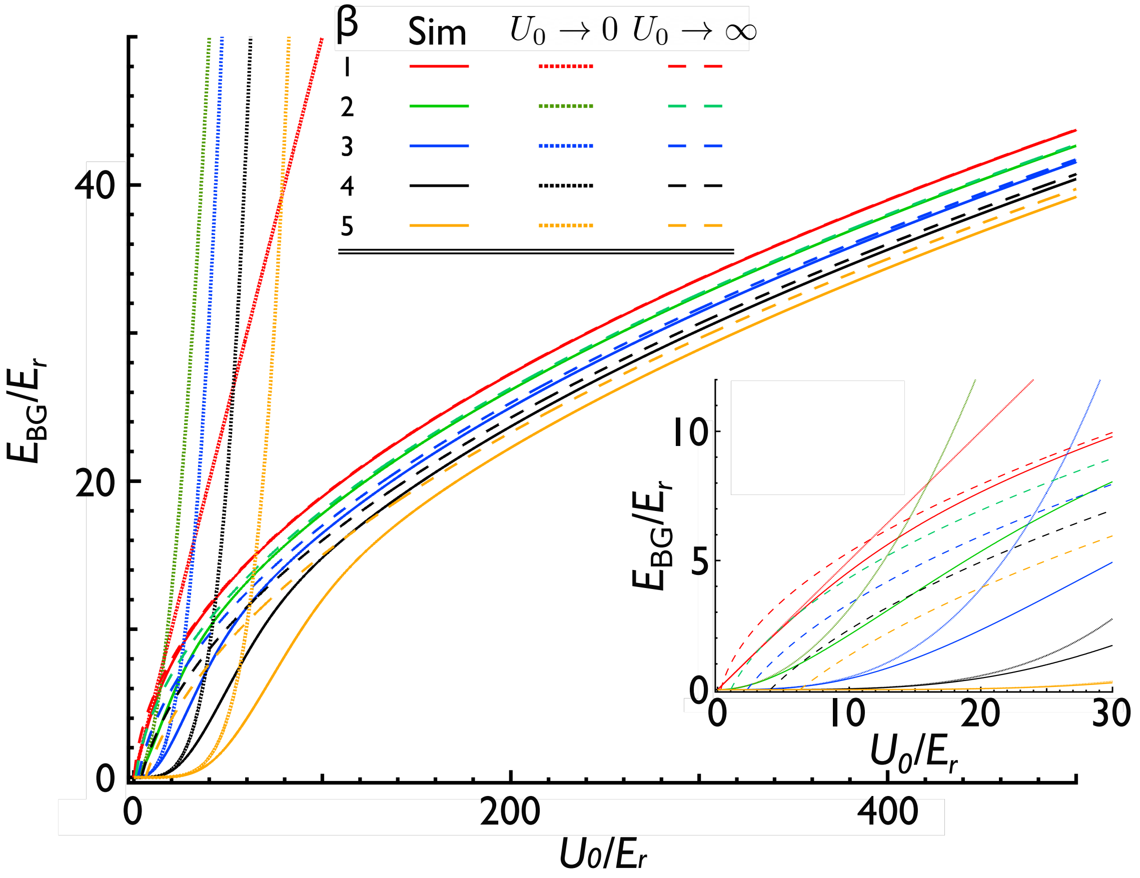

Figure 1.3: Bandgaps between $b = \beta$ and $b = \beta - 1$ for β up to 5 and for lattice depths up to $U_0 = 500E_r$. The solid lines show numerical solutions. The dotted lines show the free-particle limit, and dashed lines show the harmonic oscillator limit. Inset: A zoom in for depths in the range $U_0 \leq 30E_r$.

at the “avoided crossing” is exactly $E_{\text{BG}} = E_+ - E_- = \epsilon E_r = U_0/2$, which is the average strength of the potential.

In Figure 1.3, we show the bandgaps as a function of lattice depth for the first few bands. The solid lines are the exact numerical calculations. The dotted lines in the inset are an analytical model

$$E_{\text{BG}}/E_r = \frac{\epsilon^\beta}{8^{\beta-1}\left[(\beta-1)!\right]^2}\,, \tag{1.9}$$

where β is the larger of the two adjacent bands in an avoided crossing. The exponential scaling of the lattice depth with β is due to the simple formula[2] for the Rabi frequency of multi-photon Bragg resonances, valid at shallow depths [20]. The formula agrees for small lattice depths and recovers the expected value calculated above for $\beta = 1$ in a two-level system. What we mean by “small depths” depends on the band number. For the $\beta - 1$ band, the bandwidth is $\Delta E/E_r = 2\beta - 1$ in the limit that the lattice depth goes to zero. For larger β, we see that the lattice depth needs to be larger ($U_0 \gg \Delta E$) for the numerical solutions to deviate.

The other limiting case is when the lattice depth becomes large. Our intuition tells us that a very deep lattice means $U_0 \gg \beta^2 E_r$. When this happens, the particle would be approximately in a quantum harmonic oscillator state. We wouldn’t expect there to be any dependence of the eigenenergy on the momentum anymore, i.e., the “bands” are now flat. For a harmonic oscillator, we expect that the atoms are close to the bottom of the trap, which means that they mostly see the peak depth $\sim 2\epsilon$, instead of an average depth. The dashed lines are an analytical model

$$E_{\text{BG}}/E_r = \sqrt{8\epsilon} - \beta\,, \tag{1.10}$$

where the first term comes from a quantum particle in a harmonic oscillator potential with U_0 strength. The second term is a correction, akin to a quantum defect for

---

[2] For each avoided crossing, β describes the Bragg diffraction order whose Rabi frequency can be calculated [19] assuming a far-detuned 2β photon process.

atomic orbitals, since higher bands deviate more than lower bands from the harmonic oscillator levels at any given large depth. We see that the harmonic oscillator limit agrees with the numerical solution as long as the depth is large enough.

1.3.2 Magic depths for phase stability

One source of noise from Bloch oscillations is due to the intensity fluctuations from the lattice depth. As is evident from Fig. 1.2, the average energy of any given band varies with the lattice depth. Every excited band has a "magic depth." When expressed in terms of the recoil energy E_r, this is a unique depth for which the average band energy is first-order insensitive to variation in the lattice depth. In Chapter 4, we explore the magic depth concept in more detail and its utility towards interferometric measurements.

1.3.3 Trapped atom interferometry

Finally, we consider some implications for trapped atom interferometry, a burgeoning paradigm for precision measurement using atom interferometers. In these interferometer schemes, the matterwaves are held in trapping potentials for a portion of their interferometer paths. The trapping fields for matterwaves are analogous to fiber optical waveguides for light interferometers [21] and can be used to measure the local acceleration due to gravity [22]. In Chapter 5, we demonstrate a trapped atom interferometer with Bose-Einstein condensates trapped in an optical lattice. These matterwaves undergo Bloch oscillations while in the lattice. Whereas fiber optic light interferometers contend with the thermal noise of fiber optics [23], lattice-trapped atom interferometers are plagued by intensity noise due to inhomogeneity and fluctuations in the lattice beam(s) [24]. We compare the performance of the trapped atom interferometer with and without the magic depth. We find preliminary evidence for an overall enhancement of the interferometer signal, but further investigation is needed.

Chapter 2

EXPERIMENTAL APPARATUS

Steering an ultracold atom interferometer machine can be described as a labor of love. Often in our experiments, preparing a Bose-Einstein Condensate (BEC) is simply the starting point of our scientific pursuits. For our purposes, the low temperature of our matterwaves, i.e., narrow momentum distribution, is the key benefit of a Bose-Einstein Condensate. However, it comes at the cost of added complexity. Many individual components are timed and tuned appropriately to ensure the reproducibility of our BEC. Likewise, the coherent control of the BEC requires great consideration. In this chapter, I'll describe some of the basic ingredients demanded of us for the BEC production, and our atom manipulation tools. Many more details of the experimental apparatus can be found in the thesis work from an earlier generation of workers [25, 26, 27].

The basic overview of the experimental apparatus is as follows. A ytterbium ingot is sublimated in a 365 C oven inside a stainless steel vacuum system. The hot atoms then go through a pair of small apertures to form an atomic beam with a narrow transverse velocity distribution. The atomic beam traverses a Zeeman slower stage, followed by a crossed-beam slowing stage just before a magneto-optical trap (MOT). After loading atoms into the trap for 5–10 s, the MOT is compressed. The compressed MOT is turned off after being loaded into an optical dipole trap (ODT). The atoms are further processed by evaporative cooling in the ODT. After the evaporative cooling stage, the atoms are typically a quantum degenerate gas—in our case, a BEC. Finally, the BEC is manipulated via optical lattice pulses for our interferometry experiments and scientific campaigns [1].

2.1 Cool Ytterbium

Neutral ytterbium (Yb) is a Lanthanide element that has a closed-shell electron configuration ([Xe]$4f^{14}6s^2$) with a $6s^2\,{}^1S_0$ ground state. Its closed divalent electron shell structure makes it similar to Group II elements such as Calcium (Ca) or Strontium (Sr). For this reason, Yb is considered an Alkaline Earth-like element.

Ytterbium has several appealing characteristics for interferometry, making it our atom of choice. Ytterbium hosts numerous stable isotopes listed in Table 2.1, all of which can be laser cooled. This makes it a suitable element for systematic cross-checks in various precision measurements involving cold atoms or ions. All the bosonic isotopes of neutral Yb have zero nuclear spin, making their ground state ($I = 0$, $L = 0$, $S = 0$) highly insensitive to magnetic fields[2]. Fermionic ytterbium in its ground state is still fairly insensitive to magnetic fields up to its *nuclear* magnetic moment ($\mu_B/\mu_N \sim 2000$), where $\mu_{B(N)}$ is the Bohr (nuclear) magneton. Furthermore, degenerate fermions are protected against s-wave collisions. Because ^{174}Yb is the most abundant and has a convenient scattering length for evaporative cooling, we work with this bosonic isotope for experiments described in later chapters. The relevant cycling transitions for ^{174}Yb, illustrated in Figure 2.1, are the violet ($\lambda_V = 398.9\,\mathrm{nm}$) and green ($\lambda_G = 555.8\,\mathrm{nm}$) atomic transitions.

The violet transition (${}^1S_0 \to 6s6p\,{}^1P_1$) is fairly wide ($\Gamma_V = 2\pi\times 28\,\mu\mathrm{s}^{-1}$), while the green transition (${}^1S_0 \to 6s6p\,{}^3P_1$) is a narrow ($\Gamma_G = 2\pi\times 182\,\mathrm{ms}^{-1}$) intercombination line. While such a transition would be dipole forbidden ($\Delta S = 0$ selection rule), a spin-orbit coupling perturbation from relativistic considerations of the Coulomb po-

---

[1] We use the Cicero Word Generator software to control our sequence timings and various analog, digital, and RS232 outputs.

[2] Small perturbative effects from magnetic fields may exist. For example, relativistic considerations of atoms moving with velocity $\mathbf{v}$ in a magnetic field $\mathbf{B}$ produce an electric field $\mathbf{E} = \mathbf{v}\times\mathbf{B}$ in the frame of the atoms, which causes a motional Stark effect [28].

tential in the electron's frame breaks this symmetry. The resulting narrow transition has several benefits, including a lower Doppler-limited temperature during the MOT stage and a smaller spontaneous scattering rate for off-resonant potentials such as a dipole trap. In particular, the small spontaneous scattering rate eases constraints for atom-optics beam detunings, opening the way for matterwave interferometry with long interrogation times.

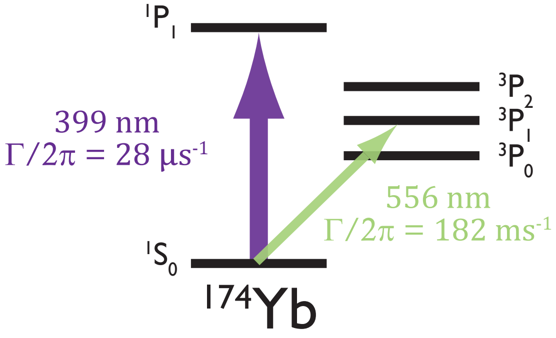

Isotope	Abundance (%)	Nuclear Spin
^{168}Yb	0.12	0
^{170}Yb	2.98	0
^{171}Yb	14.09	1/2
^{172}Yb	21.69	0
^{173}Yb	16.10	5/2
^{174}Yb	32.03	0
^{176}Yb	13.00	0

Figure 2.1 & Table 2.1: Properties of ytterbium. On the left, we show the narrow (green) transition and the broad (violet) transition utilized in our experiments. The table on the right summarizes some properties of the stable isotopes of ytterbium.

Throughout my PhD, experimental platforms involving Yb have also generated sustained excitement for quantum sensing and quantum information applications due to the wide selection of laser accessible transitions offered by ytterbium isotopes. Notably, the yellow (578.4 nm) $^1S_0 \rightarrow 6s6p\,^3P_0$ transition has a linewidth of $2\pi \times 10^{-3}\,s^{-1}$. This makes neutral Yb suitable for precision timekeeping, such as optical lattice clock experiments [29], while other transitions are utilized in ion and Coulomb crystal clocks

[30]. Spectroscopic studies of the isotope shifts in long-lived states are also used to produce generalized King plots [31, 32] which serve beyond Standard Model searches for new particles. The narrow linewidth provided by ytterbium complexes [33] also promises highly sensitive magnetic field detection. Finally, several platforms for quantum computation with neutral Yb and singly ionized Yb^+ have been developed [34] where the implementation of quantum error correction codes [35] or non-abelian topological order [36] offer an exciting route for the prospect of fault-tolerant computation.

2.2 Vacuum System

The stainless steel ultra high vacuum (UHV) system remains essentially unchanged since the writing of Ben Plotkin-Swing's Thesis, and as such, Ref. [25] contains many more details. I can speak for the rest of the interferometer crew that the robustness of the vacuum apparatus is much appreciated. A gate valve separates the oven and the science chamber. The ion gauge near the science chamber consistently measures UHV pressures on the mid $10^{-11}\,\mathrm{Torr}$ level while the flange is closed, and low $10^{-10}\,\mathrm{Torr}$ pressures while the flange is open. These background pressures are sufficient for our current and near-term experimental goals. The vacuum pressure may be improved by running the titanium sublimation pump that is already connected to the vacuum system.

The vacuum-limited lifetime of the atoms in the science chamber was measured by extracting the decay rate from a fluorescence trace of atoms inside the MOT. This was done using a photomultiplier Tube (Thorlabs PMM02) and transimpedance amplifier (SRS SR570). We first capture atoms in the MOT until the fluorescence signal saturates, after which the Zeeman slowing beam and the X-beam are shuttered. This allows the MOT atom number to exponentially decay through background gas collisions. The resulting decay rate of $\sim 45\,\mathrm{s}$ is much larger than the time scale of any of our experimental sequences.

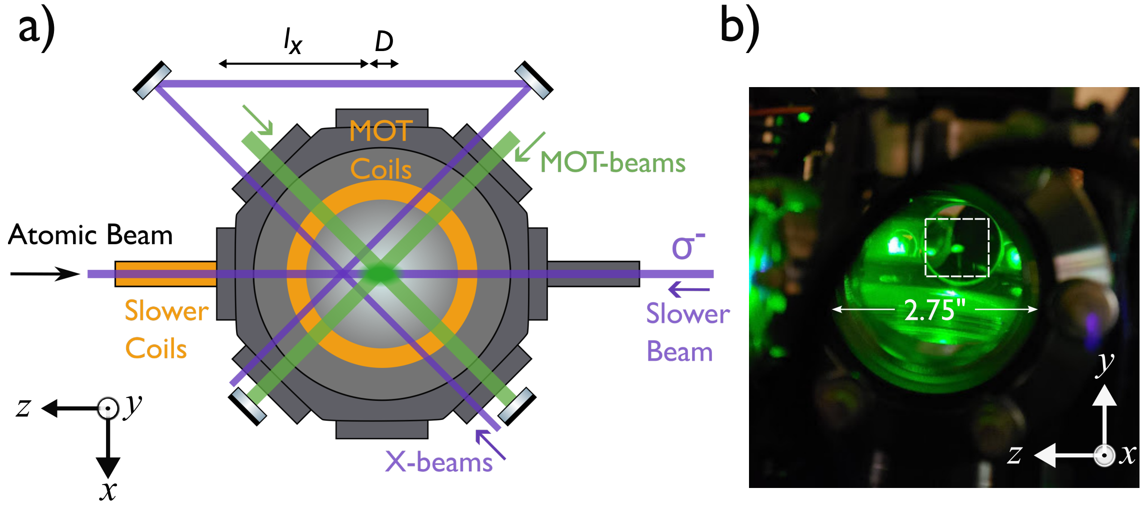

Figure 2.2: MOT chamber with fields. (a) Birds-eye schematic. An increasing field Zeeman slower is followed by the X-beam slower before the MOT. (b) Side view roughly coinciding with side imaging (see Section 2.7). A dashed rectangular region highlights a MOT fluorescing with $> 10^8$ ytterbium atoms.

2.3 *Laser Cooling and Trapping*

2.3.1 Zeeman slowing

The first stage of laser cooling is done by Zeeman slowing coils and cooling via the violet transition. The radiation force from the violet transition is used to push against the atomic beam while keeping the beam on resonance ($\Delta \sim 0$ in Eq. (2.1)) for an initial velocity class of the atoms. We choose this velocity class to be near the most probable velocity of our thermal ensemble ($v_i \sim 300\,\mathrm{m/s}$). The radiation force

$$F_{\mathrm{rad}} = \frac{1}{2}\hbar k \Gamma \frac{s}{1 + s + (2\Delta/\Gamma)^2}\,, \tag{2.1}$$

depends on the beam intensity $s = I/I_{\mathrm{sat}}$, the laser detuning Δ, the wavenumber $k = 2\pi/\lambda$ and the transition linewidth Γ. The saturation intensity is $I_{\mathrm{sat,V}} = (2\pi^2/3) \cdot \hbar \Gamma_V c/\lambda_V^3 \approx 58\,\mathrm{mW/cm^2}$ for the violet transition, where $\hbar$ is the reduced Planck's constant and c the speed of light.

The microscopic picture is that atoms absorb photons from the Zeeman slower beam as they move through the Zeeman slower region. Each absorption event slows the atoms down by one photon recoil. Then the atom spontaneously scatters a photon in a random direction so that the average velocity of an atomic ensemble would remain unchanged from spontaneous scattering with the net effect of the atoms slowing down along the Zeeman slower direction. It takes $\sim 50,000$ absorption events to slow down atoms from the atomic beam to zero velocity using the radiative force of a violet beam.

The slower region is comprised of a σ^- polarized slower beam and the hand-wound magnetic coils [27], which produce the slower field. As the atomic beam decelerates due to the radiation force, the change in Doppler shift is balanced by the change in the Zeeman shift via a spatially varying magnetic field gradient. The resulting detuning $\Delta = \delta_{\text{AOM}} - k_V v_z + g_F \mu_B m_F B_z/\hbar$, is kept at 0, where $v_z(z)$ is the velocity of the atomic beam, and $B_z(z)$ is the magnitude of the slower magnetic field. The g-factor, Bohr magneton, and magnetic quantum number are, respectively, g_F, μ_B, and m_F. For the increasing slower field in Eq. (2.2), $m_F = -1$ and atoms ideally experience a constant deceleration, which implies that slower coils must produce an inhomogeneous magnetic field of the form

$$\vec{B}(z) = -\hat{z}\frac{\hbar k_V}{g_F \mu_B} v_i \sqrt{1 - \frac{2F_{\text{rad}}}{v_i^2 M_{\text{Yb}}} z}\,. \tag{2.2}$$

The length of an ideal Zeeman slower would be $L_0 = v_i^2 M_{\text{Yb}}/(2F_{\text{rad}})$, where M_{Yb} is the mass of ytterbium, so that the atoms with initial velocity class v_i, have zero exit velocity. The increasing field design is advantageous because it ensures that the slower beam is never resonant with the near-zero velocity class atoms at the MOT. For our experiment, we generate additional fields from offset coils and reverse slower coils, which are used to null the magnetic field from the slower at the location of the MOT.

In practice, slower parameters are adjusted to optimize the loading rate into the magneto-optical trap. We tune the slower beam frequency detuning, ($\delta_{\text{slower}}/(2\pi)$), through an acousto-optic modulator (AOM), which fixes the initial velocity class v_i of the atoms that are on-resonance with the slower beam. The length of the slower region is fixed by the physical length of the current-carrying coils. The slower field current is also adjusted to tune the radiation force, which controls the exit velocity of the atoms. We don't see much improvement of the loading rate into the magneto-optical trap for slower beam intensities above $\sim 60\,\text{mW}$ power with a $\sim 0.5\,\text{cm}$ spot size.

2.3.2 Crossed-beam slowing

One of my predecessors, Benjamin Plotkin-Swing, developed the concept for a crossed-beam (X-beam) slower [25]. While a key advantage of a narrow-line MOT is the small Doppler-limited temperature, this also means that the MOT can only capture atoms with a small enough kinetic energy. By energy conservation we have

$$\frac{1}{2}M_{\text{Yb}}v_c^2 \simeq \frac{1}{2}\hbar k_G \Gamma_G D\,. \tag{2.3}$$

The resulting capture velocity v_c depends on the natural linewidth Γ_G, of the MOT transition, the diameter D, of the MOT beams, and $k_G = 2\pi/\lambda_G$, which is the wavenumber of the green transition. The Doppler-cooling limit is $T_D = 0.5\hbar\Gamma/k_B \approx 5\,\mu\text{K}$, where k_B is the Boltzmann constant, and the capture velocity is $v_c \approx 10\,\text{m/s}$ for a $2\,\text{cm}$ MOT. The small capture velocity necessitates more time for deceleration before the MOT stage. In other words, more spontaneous scattering events in the Zeeman slower region are required which increases the transverse velocity spread.

Here lies the problem with a narrowline MOT. There is a region between the Zeeman coils and the MOT ($l_X \approx 3\,\text{in}$), in which the atoms should travel with velocity $v_z \lesssim v_c$ towards the MOT region. The transverse velocity component $v_\perp$ after the atoms exit the slower region is significant compared to the longitudinal exit velocity v_z, causing some atoms to miss the MOT region entirely. This phenomenon is called blooming and results in poor MOT loading rates. The following conditions

$$\frac{v_\perp}{v_z} l_X \leq D \ , \tag{2.4}$$

$$v_z \leq v_c \, , \tag{2.5}$$

should be satisfied, constraining the velocity v_z of the atoms out of the slower, where D and v_c are defined the same as in Eq. (2.3). Condition (2.4) forces v_z to be large enough so that there is no significant blooming, and condition (2.5) forces it to be small enough so that the atoms don't escape the MOT.

The crossed-beam eases the tension between the capture velocity and blooming. This pre-MOT violet laser cooling stage relaxes the amount of cooling needed during the Zeeman slower, so that the atoms have a smaller exit velocity and angular spread out of the Zeeman slowing region. The X-beam makes up for the larger longitudinal exit velocity with one final push against the atoms to slow them down. Another aspect of X-beam slowing is that there is a small amount of cooling along one of the axes transverse to the Zeeman slower.

The radiation force from the X-beam can be tuned with both the beam power and the beam frequency. In practice, we optimize the loading rate into the MOT region by tuning the X-beam power and the slower field current, since the latter controls the exit velocity, and consequently, the Doppler shift of the atoms to the X-beam light. We find that only a few milliwatts of power is needed for the X-beam light because it is close to the bare atomic resonance. The X-beam also benefits from a highly elliptical beam shape. The sheet-like beam encompasses more atoms in the cone of the blooming region than a circular Gaussian shape would, while not overlapping with the MOT beams.

We achieve a factor of 8 improvement in the MOT loading rate for the optimized settings, with and without crossed-beam slowing [37]. The X-beam slower is the most bespoke part of our cold atom experiment. However, two-stage angled beam slowing has been adopted by other experimental platforms [38, 39], including with Lanthanide atoms.

2.3.3 Magneto-optical trapping

The magneto-optical trap (MOT) is the first stage of trapping for atoms. The MOT region is comprised of a magnetic field gradient produced from a pair of coils in an anti-Helmholtz configuration and six (3×2) laser beams, which are near resonant with the green transition. Without the magnetic field, the MOT beams would constitute an optical molasses, which offers a damping force to atoms moving through it. The magnetic field gradients in a MOT, combined with the laser beams, provide a restoring force *and* a damping force. This makes the MOT a damped harmonic oscillator ($F = -\alpha \frac{dB}{dz} z - \beta k_G v$) in the limit of small displacements and small velocities. Small here means that we can approximate differential Doppler shifts by small changes in velocity ($(k_G v/\Gamma_G)^2 \ll 1$), and differential Zeeman effects just by first-order changes in the magnetic field strength.

In the experiment, we typically tune the laser beam frequencies with an AOM before the beams are split by pairs of polarizing beam splitters and waveplates. We dither the laser beam frequency by modulating the drive frequency of the AOM, whose center frequency puts the MOT beams $\approx 5\,\mathrm{MHz}$ red-detuned from the atoms at rest. The quick dithering rate (350kHz) artificially broadens the transition wavelength. This enables an effectively larger capture velocity of the MOT beams.

For our MOT beams, we are typically satisfied with $\approx 60\,\mathrm{mW}$ of power before the beams are split into three 2 cm MOT beams. After being split into a vertical beam and two horizontal beams, the beams are circularly polarized before they enter the vacuum chamber, and then retro-reflected with the opposite circular polarization before going through the chamber again, such that the atoms always see σ^+ polarized light. This way they are low-field seekers, which are trapped at the minimum of the magnetic field.

In typical experimental sequences, we let the MOT load for 6 to 10 seconds before compressing the MOT by increasing the magnetic field strength and decreasing the laser beam detuning and intensity. After compression, the MOT atoms are $\approx 40\,\mu$K in temperature. Compensation coils for the $\hat{x}$,$\hat{y}$, and $\hat{z}$ directions are used to fine-tune the alignment between the center of the MOT and the optical dipole trap.

2.3.4 Optical dipole trap loading

In the limit of a far-off resonant beam ($|\Delta|/\Gamma \gg 1$) we see that the radiation force in Eq. (2.1) is vanishingly small. Another kind of light force called the dipole force dominates instead. The dipole force, defined in Eq. (2.6) below, vanishes in the opposite limit, where light is near resonant ($|\Delta|/\Gamma \ll 1$):

$$F_{\text{dip}} = -\frac{\hbar\Delta\Gamma^2}{2}\frac{s}{1+s+(2\Delta/\Gamma)^2}\frac{ds}{dz}\,, \tag{2.6}$$

$$U_{\text{dip}} = \frac{\hbar\Gamma}{8}\frac{\Gamma}{\Delta}s\,. \tag{2.7}$$

The total light force is $F_{\text{rad}} + F_{\text{dip}}$. Notably, the sign of the detuning and the gradient determine whether this is a restoring force. The corresponding dipole potential in Eq. (2.7) is correct for a far-off resonant beam. For a dipole *trap*, we utilize a red-detuned ($\Delta < 0$) Gaussian laser beam. The combination of a red-detuned beam with an intensity profile that has a global maximum provides a stable trapping region with a local minimum in the dipole potential.

While the magento-optical trap compresses, we turn on the optical dipole trap (ODT). The dipole trap captures the atoms while the magnetic fields from the MOT are slowly decreased. At this point, we load up to 10^7 atoms into the ODT, which are now $\approx 140\,\mu$K in temperature. The temporary increase in temperature at this stage is made up for by the fact that the number density is larger. After all, the phase space density is the true figure of merit for evaporative cooling. This last stage of cooling typically lasts $\lesssim 5\,$s after which we produce a Bose-Einstein Condensate. In Section 2.4, the evaporative cooling scheme is described in greater detail.

For effective evaporation, we always use two tightly focused laser beams with an angle between them. A single beam would trap in the transverse directions due to its Gaussian shape, but the axial direction would be weakly trapped. A second beam should be used to trap in all three directions effectively. In the following section, we describe two alternative configurations that we have utilized. We use 532 nm laser beams (see Section 2.6) for evaporative cooling, which works as a trap because it is red-detuned from the *violet* transition. The dipole force from the green transition creates a repulsive contribution to the dipole force that is $\approx 16\%$ of the total dipole force. The potential depth is $\approx s \times h \times 8\,\mathrm{mHz}$, i.e., approximately 8 kHz (400 nK) trap depth per $10\,\mathrm{W/mm^2}$ intensity in the 532 nm beam(s).

Orthogonal beam trap

The typical configuration in which we employ optical dipole traps is by first trapping in a horizontal beam and then sequenrially adding an orthogonal, vertically oriented beam to form an orthogonal beam trap (OBT). The horizontal and vertical beams are along the $\hat{x}$ and $\hat{y}$ directions in Fig. 2.2, respectively. The sequential hand-off has a few benefits. Firstly, the two beams can be independently controlled. In particular, we use AOMs and waveplates to control the polarization, frequency, and power of each beam. Since the AOMs also deflect the beam, control over the RF drive frequency allows for careful fine-tuning of the trap centers. The beam shapes are also independently controlled by separate telescope systems. Our horizontal beam has a waist of $\approx 30\,\mu$m and the vertical beam has a waist of $\approx 80\,\mu$m, which were measured by imaging the beams on a camera. Towards the end of evaporation, the horizontal beam power is lowered, and the vertical beam power is increased. When this happens, without the vertical beam, the gravitational sag would cause atoms to spill out of the trap, when the gravitational energy $M_{\mathrm{Yb}} g w_0 / k_B \approx 6\,\mu\mathrm{K}$ is comparable to the trap depth of the horizontal beam. The vertical beam helps suspend the atoms against gravity. Alternative solutions to the gravitational sag problem involved employing a gravity-compensation beam [40, 41].

The drive frequency of each AOM may also be modulated to “paint” a customized potential using the beams. We employ a 50 kHz triangle waveform dithering on the RF drive so that the shape of the horizontal beam can be artificially broadened. Painting involves synthesizing a time-average potential with a dithering rate much larger than the trap frequencies [42], and is used primarily before and after our evaporation sequence. Before evaporation, painting helps to load more atoms because it increases the effective overlap of the horizontal optical dipole trap with the MOT. For the OBT, we find an optimal ODT load from the compressed MOT with 10.35 W of power in a painted horizontal beam, elongated approximately three times the waist of the unpainted beam. The resulting load number is between 7×10^6–1×10^7 before evaporation. At the end of evaporation painting the trap helps lower the density of the atoms, reducing the chemical potential from interactions in the BEC.

Folded beam trap

An alternate configuration used for almost all of the experiments done in Chapter 3 involves using just one Gaussian beam that is recycled back onto itself. The atoms feel two different beams, with the first pass of the beam going to the atoms and the second pass of the beam folded back onto the atoms. Here we employ a folded beam trap (FBT) with a 52° angle created by the intersection of the first pass of the beam with the second pass of the beam. The major advantage of this configuration is that there is a massive enhancement in the effective trap depth in the ODT. The first pass waist is $\approx 30\,\mu$m and the second pass waist is $\approx 20\,\mu$m where the choice of lenses is mostly determined by spatial constraints to refocus the 2nd pass beam back onto the atoms.

With this configuration, we lose the independence of the two beams, but we gain an effectively larger U_{dip}, for an equivalent beam power. For the FBT, we typically used 7.5 W of beam power to load a comparable amount of atoms as with the OBT.

We painted the beam with a 30 kHz dithering rate before evaporation as well. We found that painting at the end of evaporation was much more delicate since both the second and first pass paint the trap. Despite the relatively simple construction of the FBT, we found that having independent control of the beams was more favorable[3] and changed back to the OBT when a laser with more power was available (see Section 2.6).

2.4 Producing a Bose Condensed Gas

The evaporation scheme is typically split into several stages. For our experiments, we employ five stages of varying duration. Splitting up an evaporation sequence into multiple steps allows for more opportunities to diagnose unideal evaporation and for easier tunability in an evaporation scheme. Furthermore, since evaporation is more sensitive at the lowest intensities (see Section 2.8), we create more evaporation steps at lower powers. For the orthogonal beam trap geometry described above, the different stages also facilitate the trade-off between the horizontal and vertical beam trap depths. Figure 2.3(a,b) shows a trace of a typical evaporation sequence using the orthogonal beam trap via monitoring pick-offs of both the horizontal and vertical beams. All together, the evaporation sequence lasts $\approx 4\,\mathrm{s}$ in five stages followed by a short time ($< 0.5\,\mathrm{s}$) where the atoms are held in a constant trap so that they can equilibrate. By the start of Stage III, the intensity of the vertical beam becomes necessary to suspend the atoms against gravity, and number density is influenced by both traps. In Table (2.2), we describe typical atom numbers and temperatures after each evaporation step. Temperatures are extracted from the ballistic expansion of the waist and height of the atomic cloud as a function of TOF. Unlike a thermal gas,

---

[3] Another disadvantage of the folded beam trap is that a narrow laser line cannot be used. Otherwise, a malignant optical lattice is easily formed, disturbing the evaporation process. It is possible to get around this by introducing an AOM after the second pass. While another AOM introduces some independence between the beams, it also cuts some of the power in the second pass, and is not easily compatible with the painting technique.

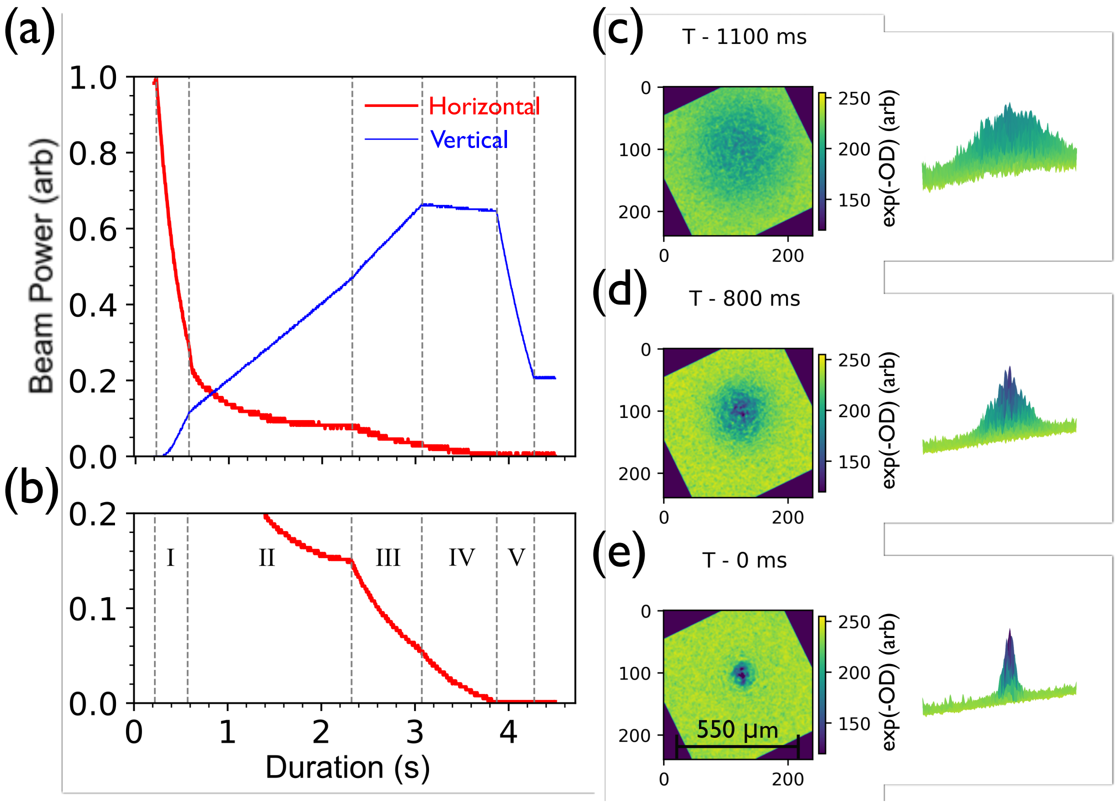

Figure 2.3: Evaporation trajectory for Bose condensation using the orthogonal beam trap. (a,b) The beam power during evaporation is monitored by a photodiode(s) for the horizontal (vertical) beam shown in the thick (thin) line of (a). The power is normalized to 10.35 W, the peak power used during evaporation. Vertical dashed lines indicate evaporation stages used in the sequence. After stage V when evaporation ends at time T, the trap is held constant for 400 ms to stabilize transients in the condensate. (b) is a zoom-in of (a) with a more sensitive photodiode. (c) Left panel shows an averaged TOF image of the atoms 1.1 s before evaporation ends. The x-y axes are the pixel grid of our camera, and the transmission $\exp(-\mathrm{OD})$, is normalized to 255, the max value of each pixel. Right panel is a projected 3d surface plot of the left panel. (d) same as (c) but 0.8 s before evaporation ends at which point the atoms form a partial condensate. (e) same as (c) but at the end of evaporation when we produce a BEC.

a BEC expands anisotropically, and the temperature quoted for Stage V in the table is for the axis with faster expansion.

During the penultimate evaporation step (stage IV) the atoms undergo a phase transition from a thermal ensemble to a Bose-Einstein condensate. Figure 2.3(c–e) shows average atomic images after holding the atoms in the trap for 400 ms so that the temperature can equilibrate and 12 ms time of flight (TOF) to allow atoms to expand. At the start of stage IV, Fig. 2.3(c), the atoms are thermal. In the middle of stage IV, Fig. 2.3(d), the atoms are a mixture of thermal and condensed atoms. During the last evaporation step (Stage V) ending at time T, we paint the horizontal optical dipole trap to decompress the BEC in the trap, useful for lowering the chemical potential of the condensate. Figure 2.3(e) shows an image of the resulting condensate. Apparent from the atomic absorption images is the change from isotropic expansion in TOF for a thermal ensemble to an anisotropic expansion for the BEC. This is due to the chemical potential inside the OBT when the BEC is more tightly confined in one of the axes of the trap, resulting in a $\approx 50\,\mu$m BEC cloud after 12 ms time of flight.

2.5 Optical Lattice Generation

We use a dipole potential composed of two counter-propagating laser beams with wavenumber $k_L = 2\pi/\lambda_G$ to generate an optical lattice. The form of the resulting periodic potential is

$$U(y) = \frac{U_0}{2}\left[1 + \cos\left(2ky\right)\right] \ , \tag{2.8}$$

$$k = \frac{\pi}{\lambda_G/2}\sin\left(\theta/2\right) . \tag{2.9}$$

Here, U_0 is called the lattice depth and k is the reciprocal lattice vector. The angle between the beams is $\theta = \pi$ in our case. Using two beams derived from separate AOMs and directed to separate optical fibers, we acquire independent control of each beam's power, frequency, polarization, and waist size. The spatial periodicity of the

Evaporation	Atom Number	Temperature (μK)
Stage I	3.5×10^6	82
Stage II	1.3×10^6	16
Stage II	7.0×10^5	7.0
Stage IV	1.3×10^5	0.9
Stage V & Hold	7×10^4	0.027

Table 2.2: Typical atom counts and temperatures after each stage of evaporation. These benchmarks were taken *without* a hold step other than for Stage V with the atoms released from the OBT. Temperatures were extracted by measuring the size of the cloud after various TOF. Before evaporation starts the 7×10^6 atoms in the ODT have $140\,\mu$K temperature.

lattice is given by $d = \pi/k \approx 278\,\text{nm}$. This and other quantities to keep in mind for optical lattices are collected in Table (2.3).

We utilize lenses on Thorlabs cage-mounting optics and a translation stage to carefully reshape the beams after the fiber output. By profiling both beams on a camera at two different spots we ensure that the beams are well collimated. The beam profiling procedure results in lattice beams of $\approx 550\,\mu$m waists. To ensure that the beams are indeed counter-propagating, we optimize the back-coupling of one beam back through the output fiber coupler of another. We achieve as much as 70% efficiency for the back-coupling from fiber outputs whose beam paths are $> 1\,\text{m}$ apart. We also align the optical lattice against gravity by examining the retro reflection from a cup of water to ensure $< 1\,\text{mrad}$ deviation from vertical. We optimize the initial alignment of the optical lattice to the atoms by maximizing Kapitsa-Dirac diffraction.

The laser light can be detuned from the optical lattice as much as $\Delta = -2\pi \times 24\,\text{GHz}$ and as a low as $\sim -250\,\text{MHz}$ from the laser line. Although this may not

Quantity, Symbol	Expression	SI value
Recoil momentum, p_r	$\hbar k$	1.2×10^{-27} kg·m/s
Recoil velocity, v_r	$\hbar k/M_{\mathrm{Yb}}$	4.1 mm/s
Recoil energy, E_r	$p_r^2/(2M_{\mathrm{Yb}})$	2.46×10^{-30} J
Recoil temperature, T_r	E_r/k_B	178 nK
Recoil frequency, $\omega_r/(2\pi)$	E_r/h	3.71 kHz
Recoil time, τ_r	h/E_r	271 μs
Spatial period, d	π/k	277.9 nm
Gravity Bloch oscillation rate, ν_g	$M_{\mathrm{Yb}}gd/h$	1.2 kHz

Table 2.3: A handy set of quantities convenient for experiments involving ^{174}Yb in an optical lattice generated from a pair of 555.8 nm counterpropagating laser beams.

seem like much, for a narrow-linewidth of the $^1S_0 \rightarrow {}^3P_1$ transition, this ranges between $\sim (1.3\times10^2)\Gamma_G$ and $\sim (1.3\times10^5)\Gamma_G$. Large detuning is especially important for interferometers so that atom-optics pulses don't decohere interferometric signals through spontaneous scattering effects. The scattering rate R_s is written in Eq. (2.10) in a convenient form with recoil units in mind:

$$\frac{R_s}{\omega_r} = \frac{U_0}{E_r}\frac{\Gamma}{\Delta} \tag{2.10}$$

In this form, the scattering rate is easily computed per recoil unit of lattice depth. The range of scattering rates for our lattice beams is then $0.18\,\mathrm{s}^{-1} \leq R_s(U_0/E_r)^{-1} \leq 17\,\mathrm{s}^{-1}$ for the range of detunings mentioned above.

2.5.1 Radio frequency drive

Both beams are derived from separate AOMs with a $\sim$ 200 MHz radio frequency (RF) drive. Independent control of the frequency of each beam allows for a frequency difference $\delta/(2\pi)$, between beams that can be controlled to generate standing waves, walking waves, and accelerating waves in the lab frame. For a walking wave with velocity v relative to the atoms, we apply a difference of $\delta = 2k \cdot v$. In the trivial case of $v = 0$, we have a standing wave when the two beams are the same frequency. For an accelerating wave, we require that $\dot{\delta} = 2k \cdot \dot{v}$, where the frequency difference is chirped.

This level of control is achieved by employing two direct digital synthesizers[4] (DDSes), one for each laser beam. One of the DDSes, which we will call DDSdisc, operates in discrete frequency mode, where up to eight (2^3) different RF drive frequencies can be stored to drive an AOM. The other DDS, which we will call DDSramp, operates in a frequency ramp mode, in which the RF drive can be up-chirped, down-chirped, or held still. A detailed guide for programming the DDS is included in Ref. [27]. Each DDS frequency is referenced to the same Cesium clock standard (Symmetricom 5071A) to ensure frequency stabilization of the RF drive. The ultimate frequency resolution is limited by the 32-bit phase accumulator, which yields a $\lesssim 50\,\mathrm{mHz}$ resolution for a $\sim 200\,\mathrm{MHz}$ drive.

In particular, our optical lattice is oriented in the vertical direction, where atoms accelerate due to gravity. The resulting chirped Doppler shift is an intrinsic problem for such experiments. We reserve the down-chirp rate of DDSramp to compensate for the gravitational-induced Doppler shift. The up-chirp rate of DDSramp is utilized for accelerating waves in Bloch oscillation pulses. The role of DDSdisc in our experiments sets a frequency difference which is used for generating standing waves or walking waves in Kapitsa-Dirac or Bragg pulses, respectively.

---

[4] The direct digital synthesizers are from the Analogue Devices model AD9910. They are bought with the Eval board for ease of use and programmed via an Arduino. The Arduino is capable of receiving serial commands via the RS232 channels in the Cicero Word Generator software.

2.5.2 A guide to setting atom-optics pulses

Here, we will describe how to set both the RF drive frequencies in a vertical lattice. There are three frames of reference to consider. The experimenter typically privileges the *lab frame*, while the Bloch band picture privileges the *lattice* frame. The atomic physics depends on the relation between the lattice frame and the atom frame. For the rest of the section, I will translate between the lab frame, the lattice frame, and the atom frame. The subsection titles represent the lattice as seen by the *atom* frame.

Standing lattice

As mentioned earlier, a necessary condition for a Kapitsa-Dirac pulse is to create a standing wave of light. However, this is not necessarily a standing wave in the lab frame! The optical lattice must be stationary in the frame of the atoms instead. In the lab frame, we generate an accelerating wave moving down with the atoms.

For a vertically oriented lattice, this is where the ramp function of the DDS comes in handy. One must first set the frequency of the DDSdisc so that it is equal to DDSramp at some initial time t_0. Then we apply the down-chirp from DDSramp. For a nominal acceleration of $g = 9.8\,\mathrm{m/s}$, the down-chirp rate is $\dot{\delta} = 2\pi \times 35.3\,\mathrm{kHz/ms}$. For any time after t_0, the down-chirp guarantees that a stationary optical lattice will be seen by the atoms.

Walking lattice

For Bragg diffraction, a useful mnemonic is that a frequency shift of $4\omega_r = 2\pi \times 14.8\,\mathrm{kHz}$ puts the velocity of that lattice at a velocity of $v = v_r$. This is easily verified by solving for v, with a Doppler shift $2kv = 4\omega_r$. In the Bloch-band picture, which gives us a view in the co-moving frame of the lattice, the quasimomentum of the atoms is shifted from $q = 0$ to $q = -p_r$.

This result is easily generalized for any N_B^{th} order Bragg pulse. For an arbitrary order Bragg pulse, we generate a lattice that moves at a relative velocity of $v = N_B v_r$ away from the atoms by setting the difference between DDSdisc and DDSramp at $4N_B\omega_r/(2\pi)$ when t_0 is the start of the Bragg pulse. We simultaneously apply the down-chirp of DDSramp to provide the gravity compensation ramp for the duration of the pulse. In the lattice frame, we see that the atoms have a momentum of $q = -N_B p_r$. In terms of the reduced Bloch band zone scheme, the atoms are in at an avoided crossing of the N_B^{th} Bloch-band with a quasimomentum of either $q = 0$ for even Bragg orders, or $q = \pm p_r$ for odd Bragg orders.

Accelerating lattice

Finally, we consider the Bloch-oscillation pulse. For Bloch oscillations, we use the up-chirp to control the Bloch oscillation rate. First, let's consider what the Bloch oscillation rate would be if we set the up-chirp rate to zero. For this case, the optical lattice would be stationary, and the atoms are accelerating due to gravity in the lab frame. In the atom frame, the lattice accelerates *upward*, at a rate of g, which means the Bloch oscillation rate would be $\nu_g = 1.2\,\text{kHz}$. In the lattice frame, the atoms undergo an adiabatic sweep in the quasimomentum across the Bloch bands. The choice between the lab and the atom frame is a gauge choice analogous to gauge fixing in electricity and magnetism. The Hamiltonian for the atom frame (Eq. (2.11)) and for the lattice frame (Eq. (2.12)) are written explicitly as

$$H_{\text{atom}} = \frac{p^2}{2M} + Mgy + U_0 \cos^2(ky)\,, \tag{2.11}$$

$$H_{\text{lat}}(t) = \frac{(p - Mgt)^2}{2M} + U_0 \cos^2(ky)\,, \tag{2.12}$$

for a cosine lattice with potential depth U_0 and acceleration due to gravity. We have assumed adiabatic $(Mgt/p_r \ll 1)$ changes. For a more accurate description of adiabatic transport in Bloch-bands see Chapter 3.

The Hamiltonian is easily generalizable to arbitrary constant acceleration. If we set the up-chirp ramp rate to an arbitrary $\dot{\delta}/(2\pi)$, we will see a lattice accelerating at the rate of $a_{\rm lab} = \dot{\delta}/(2k)$ in the lab frame. Equivalently, we have a lattice that is accelerating at the rate of $a_{\rm atom} = (\dot{\delta} + \dot{\delta}_g)/2k$ in the atom frame. Lastly, in the lattice frame, the quasimomentum sweeps with a rate of $\dot{q} = -Ma_{\rm atom}$, inducing Bloch oscillations of the atoms.

We may also load into an arbitrary initial quasimomentum q_0 in an arbitrary Bloch band b, with DDSdisc. We set DDSdisc so that the frequency difference is $[b + q_0/(\hbar k)]4\omega_{\rm rec}/(2\pi)$ from DDSramp at the start of the Bloch oscillations. The quasimomentum here is defined modulo $2\hbar k$ in the range between $-\hbar k$ and $+\hbar k$. For adiabatic transport, the atoms remain in the $b^{\rm th}$ Bloch-band and return to the initial quasimomentum q_0 with a period of $T_{\rm BO} = 2\hbar k/|Ma_{\rm atom}|$.

Trapping lattice

The trapping lattice is a special case of the standing lattice described above. We use red-detuned lattice beams to ensure confinement of the atoms in the transverse directions to the lattice axis. (Similar to the principle behind the optical dipole trap described earlier). The function of this optical lattice pulse is to trap atoms against gravity for a duration $\tau_{\rm hold}$ where the velocity of atoms is almost stationary. Since gravity induces Bloch oscillations with a rate of ν_g the atom's velocity ranges between $-v_r$ to $+v_r$ inside the trap. Typically, we apply the trapping lattice after launching atoms up with another atom-optics pulse. This can be done with Bragg pulses, Bloch oscillations, or some combination. Using this approach, it is possible to trap the atoms in an arbitrary Bloch band, with an arbitrary initial quasimomentum q_0. We catch the atoms in the trapping lattice at a time $t_{\rm catch}$ around when the atom cloud approaches the apex at time $t_{\rm apx}$ in its trajectory.

The simplest case is if we trap atoms at the apex point where the lattice is stationary in all three frames ($t_{\rm catch} = t_{\rm apx}$). In this case, the atoms are trapped with

$q_0 = 0$ in the ground band ($b = 0$). After the atoms have been launched up and are in free fall, the down-chirp of the ramping DDS is applied so that the lattice would be in the co-moving frame of the atoms, and DDSdisc is set so that the frequencies of both beams are equal at the catch time. Following that, we set DDSramp so that its frequency is held for a time T_{hold} while the atoms undergo Bloch oscillations induced by gravity. We control the timing of t_{catch} to load the atoms based on the condition in Eq. (2.13) above. We solve for t_{catch} in Eq. (2.14) to select the initial state of the atomic wavepacket in the trapping lattice:

$$Mg(t_{\text{apx}} - t_{\text{catch}}) = bp_{\text{rec}} + q_0 \,, \tag{2.13}$$

$$t_{\text{catch}} = t_{\text{apx}} - \frac{bv_{\text{rec}} + q_0/M}{g} \,. \tag{2.14}$$

The determination of the apex time limits the resolution of intial quasimomentum. Ideally, we require $q_0/p_r \ll 1$, so that the initial quasimomentum is strictly between any avoided crossings to a high precision. We employ a course and fine method to determine the apex time. The course method involves tracking the trajectory of the atomic fountain in free fall after it is accelerated by the BO launch pulse. The resulting apex of the parabolic trajectory is determined by a quadratic fit to the time of flight after the launch. The fine method utilizes the high-resolution velocimetry of Bragg spectroscopy [43] to determine the time for which the BEC is resonant with a second-order Bragg pulse. The limiting factor in the determination of t_{apx} is the resolution of the sequence generator clock speed. The $5\,\mu$s resolution limits the Bragg resonance precision to 177 Hz or $\delta q_0/p_r < 1.2\%$.

2.5.3 Alignment of the lattice

One of the most strenuous aspects about utilizing vertical optical lattices for gravitational sensing with BECs is that optical lattice needs to be aligned to itself, to the atoms, and to gravity simultaneously. This highly constrained system requires a lot of diligence to get right. We have developed several progressive fine-tuning procedures for this alignment. We walk two mirrors ($\mathrm{M_a}$ and $\mathrm{M_g}$), which are used to align the beam to the atoms and to gravity, respectively. We use the back reflection of the beam from a cup of water to align the beam vertically to gravity. We also track the position of the top fiber output by looking at a pick-off of the beam on an Allied Visions Mako CCD camera $\sim 1\,\mathrm{m}$ away from the fiber output. We always end our walking with a last iteration on $\mathrm{M_a}$ because it is less sensitive than the gravity alignment.

The course alignment procedure involves blasting the BEC with resonant light by coupling in a pick-off beam from the MOT light into the top diffraction fiber instead of the lattice beams. This method involves just one fiberized output beam and the atoms. We set the MOT light so that it is close to resonance, i.e., similar to the MOT AOM setting during the compressed MOT stage. We only need to couple $\sim 200\,\mu\mathrm{W}$ of power and apply a short square pulse of varying duration of the pulse. Then the beam is walked by iterating on $\mathrm{M_a}$ to optimize the displacement of the BEC center of mass, and $\mathrm{M_g}$ to align to gravity. When gravity is aligned within $1\,\mathrm{mrad}$ and the position of the top beam has converged within $400\,\mu\mathrm{m}$, we consider this alignment converged.

The next alignment procedure involves using both lattice beams. We use $\mathrm{M_a}$ to optimize Kapitsa-Dirac (KD) diffraction and $\mathrm{M_g}$ to optimze the alignment to gravity. The KD alignment is most sensitive near when $|J_0(x)|^2$ and $|J_1(x)|^2$ cross, where $J_n(x)$ is the n^{th} Bessel function and x is the pulse area. We tune the square pulse duration ($\sim 10\mu\mathrm{s}$) and power so that the pulse area is near the crossing point. When walking the mirrors, for each iteration, care should be taken to ensure that the bottom fiber output from the other lattice beam is counterpropagating. When gravity is aligned within $1\,\mathrm{mrad}$ and the position of the top beam has converged within $100\,\mu\mathrm{m}$, we consider this alignment converged.

The last alignment procedure measures the center of mass modulation by observing the trap oscillation of the BEC in the lattice. We measure the oscillations by holding the atoms in the lattice for a variable amount of time. We minimize the amplitude of these oscillations with $\mathrm{M_a}$ to adjust the top beam position, and use $\mathrm{M_g}$ for alignment to gravity. Again, we ensure that the counterpropagation of the bottom beam is optimized after every iteration. When gravity is aligned within 1 mrad and the position of the top beam has converged within 50 μm, we consider this alignment converged. A last optional fine-tuning method can be used to minimize the oscillation amplitude by adjusting the AOM frequency of the horizontal beam to move the atoms.

2.6 Laser Sources

2.6.1 Violet light

The violet light is sourced from a commercial external cavity diode laser (ECDL) from Toptica, the DL Pro (Bluemode). These are typically available at common blue wavelengths, e.g., 405 nm, but ours is on the violet transition (398.9 nm) when the diode is near room temperature. We typically get $\gtrsim 30$ mW out of the ECDL. Some of the light is used for saturated absorption spectroscopy, imaging, and seeding the injection diodes for the slower beam and X-beams. Figure 2.4 shows the optics layout for the violet beams, and Table 2.5 lists the AOM frequencies for various beams.

Injection locking

To supplement the relatively low power of our Toptica violet laser source, we use two more laser diodes that are injection locked. The free-running mode of these injection diodes are broad at ~ 2 nm, but they are seeded with frequency-stabilized light, which is narrower than the violet transition linewidth.

The slower beam is produced by an injected laser diode. A high-power (300 mW) single-mode violet Nichia diode (NDV4B16) was originally used. After about three and a half years of operation, we noticed a degradation of the mode quality of the diode and poor injection mode matching. Because the ytterbium lines demanded that the diode be stabilized at much lower than room temperatures (12 C-16 C), excessive water condensation was a concern. We suspected that the diode had gotten damaged during the humid season during the summer months, and indeed, we observed water condensation when we opened the diode mount.

Instead of ordering a replacement for this diode, we purchased a single-mode Nichia UV Laser Diode (NDU4316). Despite the nominally lower max power (120 mW) of this diode compared to its predecessor, we have gotten our most efficient Zeeman slowing with this new diode. Furthermore, this diode is temperature stabilized at 22.5 C, dramatically alleviating concerns over water condensation when dew points are high. The improved efficiency is owed to the improved injection quality because the free-running diode is much closer to the ytterbium absorption spectral lines at room temperature. In fact, we typically operate the diode with < 90 mW of output power which is at most 60 mW by the time it reaches the atoms[5]. Some fine tuning of the temperature using a temperature controller (Thorlabs TED 200C) is still required, with Nichia diodes typically having a 0.06 nm/K tunability. A current controller (Thorlabs LDC 200 series) is also used to stabilize the diode's free-running wavelength to tune it closer to the seed light wavelength. During the course of a day, the slow drift of the diode wavelength is corrected for by manually adjusting the current.

Our second injection-locked diode is for the crossed-beams. We shift the frequency of the seeded light for the X-beams with an AOM. We require only $\lesssim 10$ mW for the X-beams since these beams are close to resonance and the violet transition is relatively strong.

---

[5] Nichia offers wavelength selection for several of their diodes in the UVA to blue wavelengths. For the range of wavelengths and powers needed for a Yb Zeeman slower beam, this makes their diodes preferred over diodes from other manufacturers.

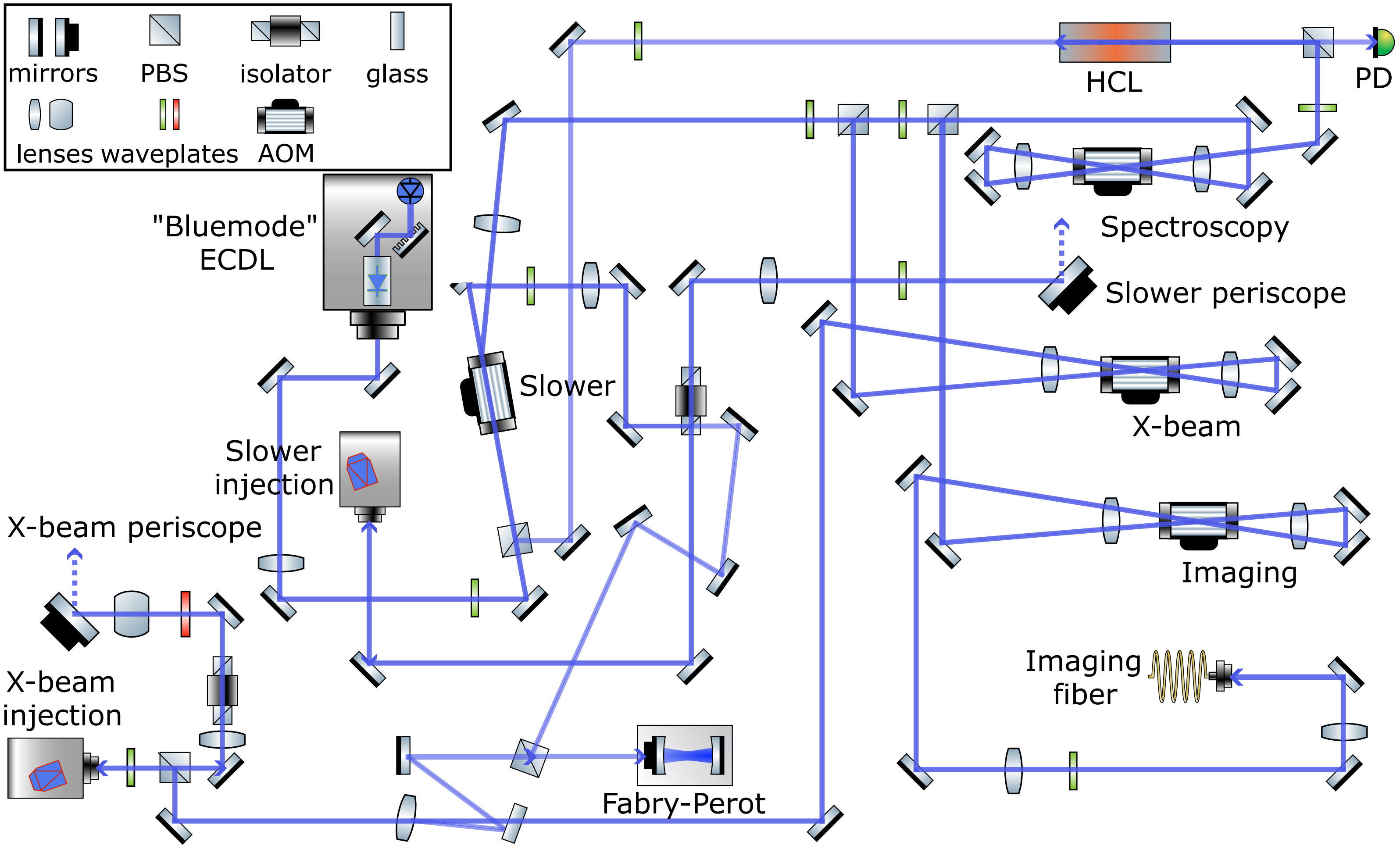

Figure 2.4: Birds-eye view drawing of the updated optics layout for the violet laser path (not to scale and reduced for simplicity). The power of the Zeeman slower and imaging beams are prioritized. The "Bluemode" ECDL source may be replaced by a TA-SHG-Pro in the future. Topleft: Legend for optics drawn using assets adapted from the 2D ComponentLibrary by Alvise Vianello.

AOM	Frequency (MHz)	Configuration
Slower	94	Single Pass, 1st Order
Spectroscopy	282	Double Pass, 1st order
Crossed-beam	180	Double Pass, 2nd order
Imaging	375	Double Pass, 1st order

Table 2.4: Violet AOM drive frequencies and configurations.

2.6.2 Green light

The resonant green light at 556 nm is produced from a Toptica TA-SHG-Pro commercial laser. The light sources the MOT beams after passing through an AOM in a double-pass configuration. We use some of this light for saturation absorption spectroscopy. Finally, we can use this light for diffraction beams detuned from resonance by AOMs.

The trapping lattice light, which is also at 556 nm is generated from a separate TA-SHG-Pro unit mounted on a brass sheet mounted about ≈ 1.5 ft above the optics table. We found it favorable to use a separate laser because we wanted a trap to detuning on the order of 10 GHz from resonance. For the trapped interferometer experiments described in Chapter 5 we also used this optical lattice light for our atom-optics pulses, such as Bragg diffraction. It is possible to use the diffraction beams from the other TA-SHG-Pro model for atom-optics and reserve the second TA-SHG unit solely for trapping in a lattice.

2.6.3 Optical dipole trap light for evaporative cooling

We also have 532 nm light for our optical dipole trap. For the folded beam trap configuration, we use a 12 W Spectra-Physics Millennia laser. After going through AOMs and optics we get at most 7.5 W from this laser. For the orthogonal beam trap

AOM	Frequency (MHz)	Configuration
Spectroscopy	450	Double Pass, 1st order
MOT	229	Double Pass, 1st order
Diffraction	~ 200	Single Pass, 1st order

Table 2.5: Green AOM drive frequencies and configurations.

configuration, we source the light from an 18 W Coherent Verdi laser. After going through AOMs and optics, we get up to 11 W after the atoms for either the horizontal or vertical beams. In the orthogonal beam configuration, the power allotted to either beam is split by a polarizing beam splitter and a half-waveplate on a rotating mount (Pacific Laser Equipment RSC-103E). The rotation angle and the RF power to both AOMs are dynamically adjusted in tandem during the evaporation sequence. One major difference between the Verdi and the Millennia is that the Verdi output is a single longitudinal mode with a 10 MHz linewidth. Consequently, the Verdi laser could not work as an FBT because of the formation of an optical lattice, which hinders evaporation. Even in the OBT, we supply AOMs for each beam so that the vertical and horizontal beams acquire a 160 MHz frequency difference.

2.7 Imaging Schemes

We use the absorption from resonant violet light for all of our imaging. We primarily utilize two different imaging planes and 3 different magnifications to look at the atoms on a daily basis. Our top-down imaging looks at the atoms in the xz-plane, and side imaging looks at the atoms in the yz-plane (see Fig. 2.2). The atoms in the magneto-optical trap and optical dipole trap are typically monitored with top-down imaging. On the other hand, manipulation of the atoms via the optical lattice is monitored via side-imaging. Top-down imaging has a high magnification (×2.67) mode and a low magnification (×0.56) mode. Side-imaging has the largest magnification (×2.98), and all three imaging modes employ two-inch imaging and objective lenses to focus the image onto CCD cameras—Allied Vision Mako model G032B or model G125B for top-down and side-imaging, respectively. The focus of the image is optimized by using translation stages on the objective lens and the cameras. We can switch between imaging modes by using magnetic base plates for swapping imaging optics. We calibrate the magnification by taking pictures with side-imaging in TOF of the atoms in free fall. Then we compare the center of mass movement to the expected displacement of the atoms in free fall with the known value of acceleration due to gravity.

In addition to those described above, we use alternate imaging planes that can image the optical dipole trap beams and the atoms at the same spot. Otherwise, aligning beams with waists smaller than the average thickness of a human hair would be incredibly difficult! For alignment purposes, we do not require knowledge of the exact magnification, but we ensure that the image of the atoms is focused onto the camera. For these imaging systems, we align the imaging beam so that it is copropagating with the laser beam that we intend to align. This method has proved useful for aligning both ODT beams to the atoms in either the OBT or FBT geometry. The crossing of the ODT beams to each other has a fairly sensitive effect on the atoms, making this alignment difficult without these additional imaging planes.

2.8 Laser Stabilization

2.8.1 Frequency lock

We stabilize the light frequency for the green and violet laser sources via saturated absorption spectroscopy. The green laser is locked to the ^{174}Yb line shown in Fig. 2.5(c) with a dedicated Yb vapor cell [44]. The violet laser can be locked to the ^{176}Yb or the ^{174}Yb line shown in Fig. 2.5(d) with a Yb hollow cathode lamp (Hamamatsu

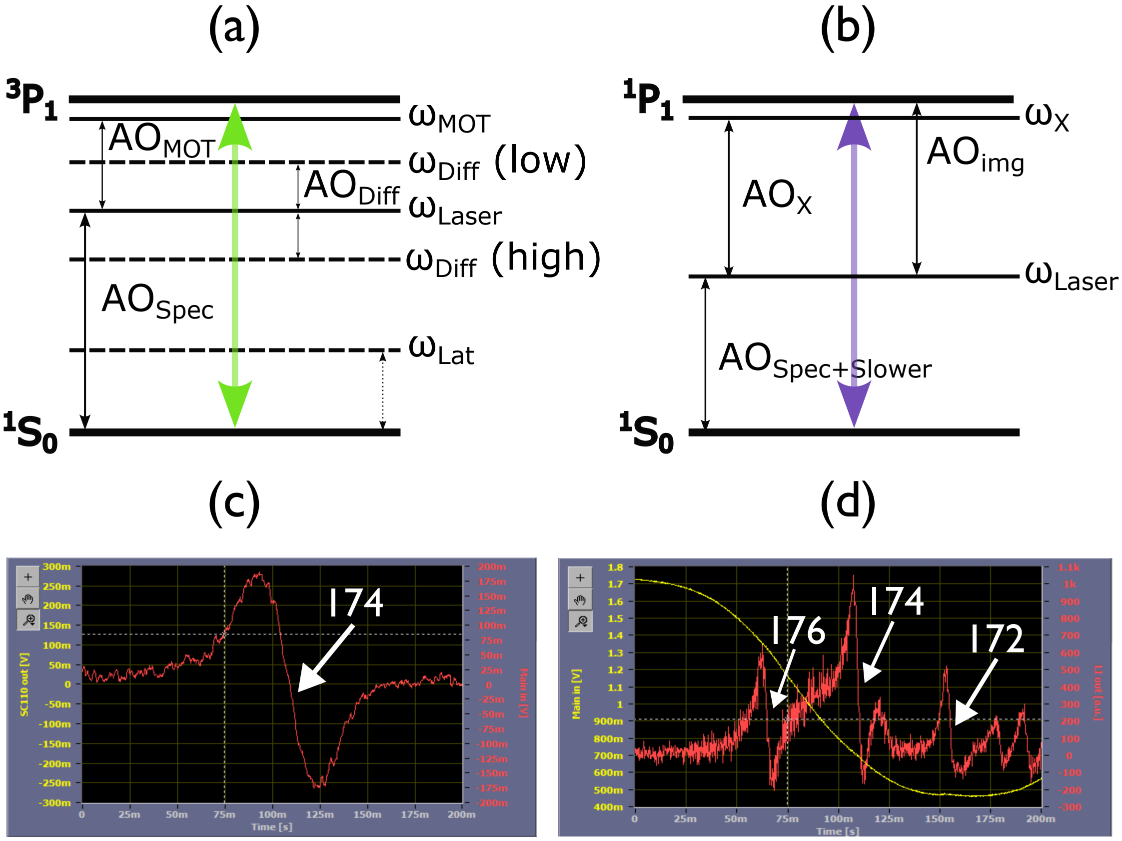

Figure 2.5: Sketch of level diagrams and measured spectral lines shown in Digilock software for violet and green transitions. (a–b) AOM frequency shifts are depicted about the ^{174}Yb green transition. The lattice trap frequency ω_{Lat} is not locked and can be used for diffraction as well. Dedicated diffraction beams may be used so that the $\mathrm{AO}_{\mathrm{Diff}}$ shifts the frequency to either ω_{Diff} high or low (b) AOM frequency shifts for violet lasers about the ^{174}Yb violet transition. (c) Error signal for the ^{174}Yb green transition. The $\mathrm{AO}_{\mathrm{Spec}}$ in (a) locks the green laser frequency red detuned $\approx$ 450 MHz from this transition. (d) Error signal in red and absorption signal in yellow showing violet spectral lines of ^{176,174,172}Yb among other isotopes. The $\mathrm{AO}_{\mathrm{Spec}}$ and $\mathrm{AO}_{\mathrm{Slower}}$ in (b) locks the violet laser frequency relative to the ^{176}Yb line. The isotope shift between ^{176}Y4 and ^{174}Y6 puts the laser frequency red-detuned $\approx$ 885 MHz from the ^{174}Yb line.

L2783-70NE-YB). With the new layout shown in Fig. 2.4, we lock to ^{176}Yb so that the bare laser can seed the injection diode for the Zeeman slower beam. There is an isotope shift of $-509.4\,\mathrm{MHz}$ between ^{176}Y4 and ^{174}Y6 [45]. This is useful to maximize the light available for the slower beam, since it does not need to get diffracted by any AOMs. For our purposes, it ensures a steady injection lock for the slower beam diode. The other AOMs are used for imaging, and the crossed-beams by shifting frequency towards the ^{174}Yb violet resonance.

The violet light is actively stabilized using an FPGA based system from Toptica called Digilock. Digilock is capable of both modulating and demodulating the saturated absorption signal (Yellow line in 2.5(d)) and for locking to the error signal with a digital PID circuit. However, we found that the signal to noise on Digilock was not sufficient for locking to the narrow green line. Instead, we opted for an analog method for generating an error signal. The error signal is then fed into the Digilock PID control directly to lock the frequency. The resulting estimated laser linewidths of our locked lasers are all sub-naturual linewidth. For the green lock as in Fig. 2.5(c), the laser linewidth is $\sim 0.2\Gamma_G$. For the violet lock as in Fig.2.5(d), the laser linewidth is $\sim 0.5\Gamma_V$ or $\sim 0.33\Gamma_V$ when we lock to the ^{176}Yb line or the ^{174}Yb line, respectively.

2.8.2 Intensity stabilization

We stabilize the power of several laser beams using a monitoring photodiode to electronically feed back onto the RF amplitude of a corresponding AOM. Most of the feedback is done with circuits consisting of only the integrator stage for the error. The AOM for the MOT, diffraction beams, and vertical and horizontal optical dipole trap beams are all intensity stabilized. The MOT feedback monitors a pick-off before the MOT beams split into three. The diffraction beams or lattice trap beams share the same fiber. They are monitored on a pick-off after the fiber ouput of each beam. The vertical ODT beam is monitored on a pick-off just before it reaches the vacuum chamber.

The horizontal beam has the most complex feedback system. Firstly, it utilizes a two-stage proportional and integrator circuit design. There are also two monitoring photodiodes—with their sensitivities about an order of magnitude different—averaged together for feedback. Each photodiode registers 11 V when they max out. The high-sensitivity photodiode is set to reach 10 V when the open-loop power of the horizontal beam is just over 2 W, and the low-sensitivity photodiode is set to approach 10 V when the laser is at max power. This averaging linearizes the closed-loop output into two regions with different linear slopes. From near max power to about 2 W is large slope region, and below 2 W is a shallow slope region. This technique allows for precise control of the power at the end of evaporation (see Section 2.4) while maintaining a high dynamic range.

2.8.3 Trapping laser

At this time, we are not frequency locking the other TA-SHG-Pro, which is tens of GHz detuned from resonance. Without specialty tools like frequency combs, locking several tens of GHz away from resonance can be quite challenging. Instead, we monitor the frequency of this light by sending a pick off to a Fabry-Perot interferometer and a wavemeter. We then correct for any slow frequency drifts manually. If left undisturbed, the frequency may drift as much as 1 GHz over the duration of one day, including the laser warm-up time (see below).

2.8.4 Temperature and humidity monitoring

One of the main reasons that our laser sources drift throughout the day is due to slow temperature and humidity changes as the system warms up. Our diagnostic capabilities recently improved thanks to the work of Richard Kim. We wanted clarity about our laser stability from temperature and humidity sensing on our optics table. Richard set-up several Rasberry Pi based humidity and temperature sensors in several strategic locations on our optics table. The wireless communication capabilities of the Rasberry Pi allow for a continuous stream of temperature and humidity data to monitor.

We learned from these diagnostics that after a daily warm-up, standard black curtains around the optics table do well for stabilizing the temperatures within $\sim 0.1^\circ$ C over a day, even if there are temperature fluctuations on the order of $\sim 1^\circ$ C outside of the curtains. We also observed that the major contribution of the temperatures variation throughout the day is a warm-up time ($\sim$ 3–4 hr) in the morning, initialized to when we turn on lasers. Surprisingly, the turn-on of the ytterbium oven does not have a noticeable effect on the warm-up time. Additionally, the relative humidity can drift on the order of $\sim 1\%$ over a day, and there is a slow seasonal drift, where the relative humidity varies by $\sim 30\%$ over a year.

Chapter 3

MULTI-PATH STÜCKELBERG INTERFEROMETRY

Our first foray into in-lattice atom interferometry began when we wanted to better understand the efficiency of Bloch oscillation pulses. We wanted to thoroughly investigate the efficiency of this atom-optics tool because Bloch oscillations (BOs) are a technique to impart large momentum transfer (LMT) between two arms of an atom interferometer. This is due to the fact that the successive application of N_{BO} Bloch oscillations provides a $2\hbar k N_{\mathrm{BO}}$ momentum shift, where k is the reciprocal lattice vector. Therefore, LMT-BOs require atoms to be loaded into a pulsed optical lattice for a sufficient duration until the desired momentum separation is achieved.

The standard description that governs the efficiency of quantum transport during Bloch oscillations is the famous Landau-Zener formula, Eq. (3.1), which describes the tunneling probability associated with transitions between two diabatic states—each of which has an associated adiabatic channel—coupled at an avoided crossing. For atomic transport, the diabatic states are represented by delocalized free-particle states, $\{|2n\hbar k + q\rangle\}$, whose momentum can be expressed modulo $2\hbar k$ quantized in units of 2 photon recoil momenta. Similarly, the adiabatic channels are the delocalized Bloch states, $\{|\phi_b\left(q\right)\rangle\}$, of the optical lattice potential whose corresponding eigenvalues are the celebrated Bloch-band solutions. For either basis, given a value of q, there is a countably infinite number of eigenstates.

In this manifestation, the Landau-Zener tunneling corresponds to diabatic transitions between free-particle momentum states by means of interband tunneling across Bloch bands. A constant force on top of the optical lattice potential causes the particle to sweep through the intraband Bloch states (smoothly changing q) and tunnel into a neighboring Bloch band at an avoided crossing with probability

$$P_\beta = \exp\left(-\frac{\pi^2}{8\beta}\frac{E_{\text{bg}}^2 T_{\text{BO}}}{hE_r}\right). \tag{3.1}$$

Here E_{bg} is the depth-dependent band gap[20], T_{BO} is the Bloch oscillation period, h is Planck's constant, and β is the higher of the two bands involved near any particular avoided crossing. The recoil energy is $E_r = h^2/8Md^2$ for a particle with inertial mass M in a lattice with spatial periodicity d, is equivalent to the zero-point energy of a particle in an infinite well of the same width as the lattice spacing.

In other words, P_β represents the infidelity of the atoms, or the probability of changing their Bloch band, during transport through an avoided crossing. Atoms that tunnel experience the force that causes Bloch oscillations, but are barely bothered by the underlying lattice potential. These atoms are left behind by the atoms that accelerate.[1]Considering that many Bloch oscillations, each imparting $2\hbar k$ worth of momentum, are needed for large momentum transfer, these infidelities should be avoided at all costs.

3.1 Limitations of Landau-Zener Description

For far-detuned optical lattices, infidelity can be reduced in two ways. The first is to increase the Bloch oscillation period, which requires a longer duration for optical lattice pulses, and the second is to increase the bandgap, which requires more laser power. If there is laser power to spare, the latter is vastly preferred. There are two primary reasons for this. The first is that the exponent goes as E_{bg}^2, which is better than the linear dependence on T_{BO}, and the second reason is that the duration of

---

[1] The infidelity of quantum transport due to finite inertia also appears in the Stewart-Tolman effect[46] where in the frame of the lattice there is an equivalent electromotive force which transports particles. This is also apparent in Landau-Zener tunneling in that, the exponent in equation (3.1) is proportional to $E_r \propto m^{-1}$, suggesting that lighter particles are more likely to tunnel. In other words, there is no universality of falling inside a lattice. We can however, introduce a natural set of units for the system where $\epsilon = E/E_r$ and $\tau_{\text{BO}} = T_{\text{BO}}E_r/h$ for a universal description of LZ tunneling.

the optical lattice pulses generally needs to be minimized for atom interferometers. Otherwise, stochastic differential phase shifts from the optical lattice may scramble the phase of the atomic wavepacket. Smaller lattice pulse durations also allow for larger interrogation times, which improve the sensitivity of interferometric measurements. The conventional wisdom is then that it is best to use ground Band ($b = 0$) Bloch oscillations for LMT because they are always more efficient than excited band ones. This is because, given an optical lattice depth, as the band number $b \to \infty$, the bandgap between the β and $\beta - 1$ bands monotonically decreases. We will address this prescription later in Chapter 4, where we argue that higher bands have a special advantage for BO pulses.

The Landau-Zener formula cannot be the complete story for understanding the dynamics of Bloch oscillations for large momentum transfer. The theoretical treatment uses approximations that necessarily break down under the conditions that we want to utilize the most. The approximations are

$$E_\beta\left(q\right) - E_{\beta-1}\left(q\right) = \hbar\dot{\delta}t, \tag{3.2}$$

$$\frac{d}{dt}\left|2\beta\hbar k + q\right\rangle = \frac{d}{dt}\left|2(\beta-1)\hbar k + q\right\rangle = 0 = \dot{E}_{\text{bg}}, \tag{3.3}$$

where the angular frequency sweep rate from a force $\vec{F}$ inducing BOs is $\dot{\delta} = 2\vec{k}\cdot\vec{F}/m$. For a sweep through the avoided crossing which is linear in time, i.e., $\ddot{\delta} = \dot{\vec{F}} = 0$, condition (3.2) means that the energy difference between the adjacent diabatic states is linear as a function of time. Condition (3.3) says that the diabatic states and the coupling between them are not a function of time. The first condition is always true for Bloch bands, but the latter is violated in the limit of fast sweeps or in the limit of large lattice depths.

For large lattice depths, bandwidths become narrow, and the avoided crossing region essentially takes about the entire Brillouin zone, which means that the diabatic state cannot start or end far away from the avoided crossing and must transform during the quantum transport. This problem may be circumvented for the simplest case of one Bloch oscillation ($N_{\mathrm{BO}} = 1$) if the eigenstate of the atoms is adiabatically changed from the free-particle and Bloch states and back again at the start and end of the BO period. For fast sweeps, the time dependence of q may give rise to a non-trivial time dependence of diabatic coupling in the avoided crossing region. These are problems for us because, for efficient large momentum transfer, we would like to accelerate our atoms as quickly as possible, which requires some balance between large optical lattice depths and fast transport.

So far, I have motivated why a careful study of Bloch oscillation efficiencies is needed in the domain of large lattice depths ($E_{bg}/E_r \gg 1$), short Bloch oscillation times ($T_{BO}Er/h \ll 1$, and many Bloch oscillations ($N_{\mathrm{BO}} \gg 1$). It was in this pursuit that we observed another intriguing interference phenomenon that appears for $N_{\mathrm{BO}} > 1$.

3.2 Landau-Zener Beam Splitters

The use of Bloch oscillations as an atom-optics tool for interferometry introduces an intra-pulse in-lattice interferometer. As an LMT atom-optics tool, Bloch oscillations are ideally implemented as a quantum transport tool that traverses between two atomic states separated by a large momentum. Therefore, within the LMT-BO optical lattice pulse, there are necessarily quantum phase effects associated with this atomic passage.

In this study [47], we investigate the phase associated with LMT-BO processes by utilizing the fact that each Bloch oscillation is accompanied by a Landau-Zener (LZ) crossing event, which acts as a beamsplitter between the diabatically coupled energy levels, or energy bands. The interference effect due to successive beamsplitter events is known as Landau-Zener-Stückelberg-Majorana interference [48, 49, 50, 51], which we will refer to as Stückelberg interference for short. After performing multi-path Stückelberg interferometry (MPSI) on a Bose-Einstein condensate (BEC) atom source, we measure the interference signal and characterize the interference effect. We find that the MPSI exhibits a signature temporal interference pattern from the path splitting and recombination due to relative Stückelberg phase accumulation along different atomic trajectories. The in-lattice atom interferometer paths are composed of Bloch state amplitudes evolving along Bloch bands during an LMT-BO pulse. We find that this interference pattern is in very good agreement with coherent, single-particle Schrödinger evolution with Bloch oscillations dynamics starting in either the ground ($b = 0$) or excited ($b = 1$) band.

The multi-path Stückelberg interferometer sequence is shown in Fig. 3.1. Time of flight (TOF) absorption images are used to probe the Bloch state amplitudes after a sequence of N_{BO} Bloch oscillations. The BOs are driven by an accelerating lattice of depth U_0. In the lattice frame, the atoms experience a periodic potential with an effective constant force. The corresponding tilt of the periodic potential in the freely falling frame is uniquely determined by T_{BO}, the Bloch oscillation period. The single-particle dynamics in this frame are described by the Hamiltonian

$$\hat{H} = \frac{\hat{p}^2}{2m} + U_0 \cos^2\left(\pi \frac{\hat{y}}{d}\right) - \frac{h}{T_{\text{BO}}} \frac{\hat{y}}{d} \,. \tag{3.4}$$

Here, the lattice spacing d is fixed by the optical lattice wavelength, and the BO period T_{BO} can be tuned via the relative frequency chirp of the counter-propagating laser beams that form the lattice. In section 3.5, additional details are provided about the optical lattice control. In short, a linear frequency sweep $\dot{\delta}_{\text{BO}}$ is applied to induce a finite sweep rate across the Brillouin zone.

In Fig. 3.1(a) we present the MPSI in a periodic zone scheme. For most of this work, we load the atomic cloud into the ground band ($b = 0$) of the lattice at quasimomentum $q = 0$. We show a typical intensity ramp trace in Fig. 3.1(c) with an exponential fit of the ramp-up (dashed line) yields a $1/e$ time of 148 μs for the lattice load. Then we initiate the linear frequency sweep $\dot{\delta}_{\text{BO}}$, which engages the Bloch oscillations. Considering only the first two bands, this interference geometry generates

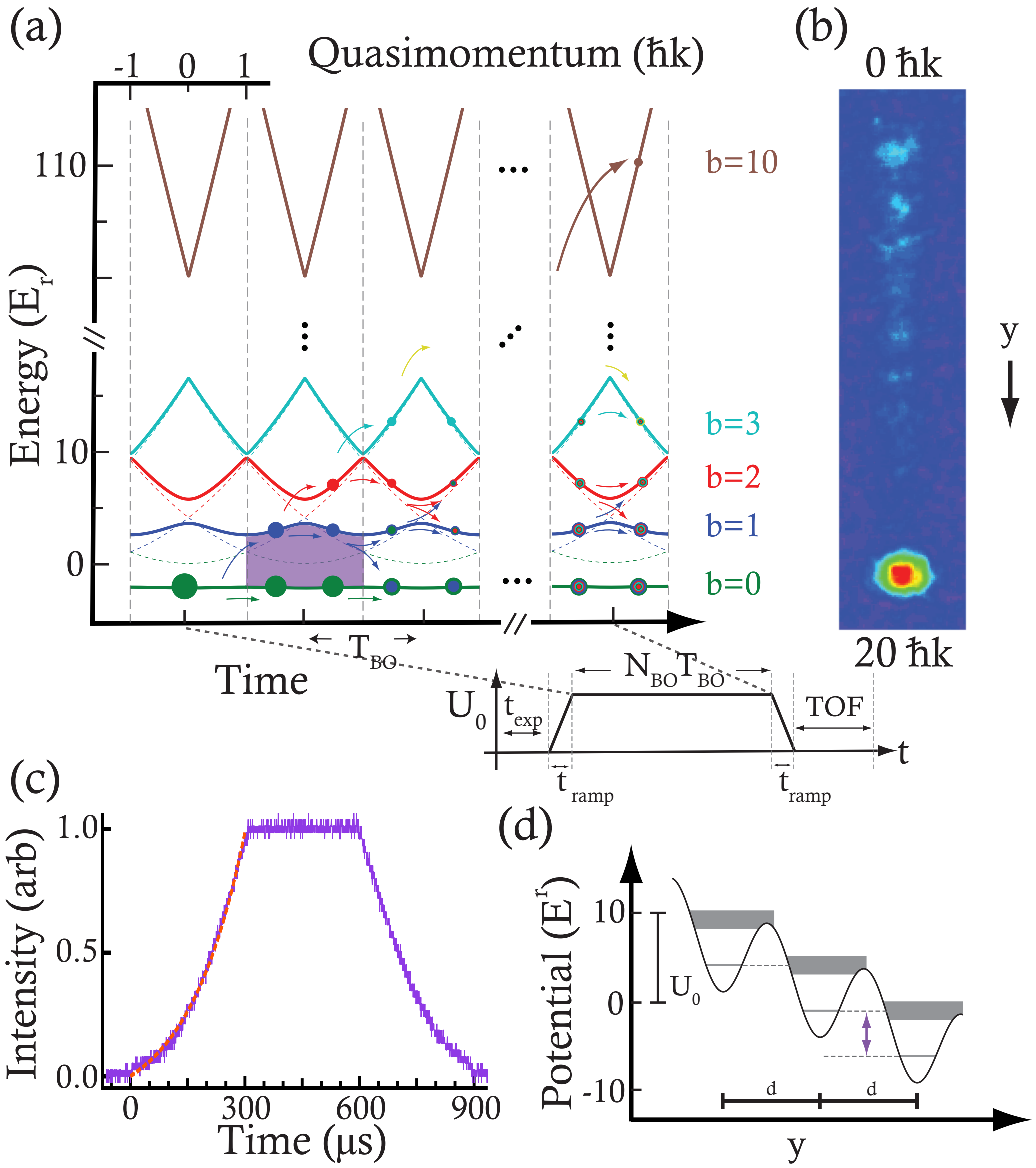

Figure 3.1: Multi-path Stückelberg interferometer sequence. (a) Atomic passage due to BOs in a periodic zone scheme with avoided band crossings acting as beamsplitters, shown for $U_0/E_r = 10$ and $N_{\mathrm{BO}} = 10$. The shaded region highlights the energy difference between $b = 0$ and $b = 1$ within one Brillouin zone. Inset: A sketch of the lattice intensity during a typical MPSI sequence. (b) Averaged absorption image ($t_{\mathrm{exp}} = 3\,\mathrm{ms}$, TOF=12 ms) showing MPSI output ports for $N_{\mathrm{BO}} = 10$, $U_0/E_r = 6$, $T_{\mathrm{BO}} = 0.33(h/E_r)$. Gravity points against the y direction. (c) A representative intensity profile with $T_{\mathrm{BO}} = 0.11(h/E_r)$, $N_{\mathrm{BO}} = 10$, $U_0/E_r = 6$. (d) Washboard potential for $U_0/E_r = 10$ and $T_{\mathrm{BO}} = 0.2(h/E_r)$ with shading for the bandwidth.

$2^{N_{\mathrm{BO}}-1}$ distinct paths. Since band numbers up to $b = N_{\mathrm{BO}}$ may be populated, and all excited bands have two avoided crossing, there are many additional paths [52, 53]. Therefore, this exponential scaling is a lower bound on the total number of interfering paths, meaning that simulating this problem on a classical computer becomes very quickly resource-intensive.

The velocity width of the atom cloud is less than 10% of the Brillouin zone before the application of the optical lattice. Each avoided crossing acts as a coherent beamsplitter where an interband transition may occur. Equivalently, the atoms experience the Hamiltonian of Eq. (3.4) during this sweep time set by $N_{\mathrm{BO}} \times T_{\mathrm{BO}}$. The TOF absorption image shown in Fig. 3.1(b) displays the different output ports of the MPSI as populations of free-particle states separated by multiples of $2\hbar k$, adiabatically mapped from the corresponding Bloch states. In Fig. 3.1(d), we see the effective washboard potential for parameters in which there is a Stückelberg resonance condition.

3.3 Stückelberg Interference Signals

3.3.1 Ground band MPSI

We first demonstrate MPSI for ground band BOs with $N_{\mathrm{BO}} = 10$, a sequence large enough to capture the $N_{\mathrm{BO}} \to \infty$ behavior relevant for large momentum transfer. As shown in Fig. 3.2(a), the interferometer output, equivalently the 10-BO efficiency, exhibits oscillatory behavior as a function of T_{BO} for various lattice depths. The N_{BO}-efficiency is defined as the fraction of the total atom number accelerated to momentum $2N_{\mathrm{BO}}\hbar k$ by the frequency chirp $\dot{\delta}_{\mathrm{BO}}$. A standard analysis associates each avoided crossing with an LZ tunneling process [48, 54] where the $b = 0$ population is depleted *incoherently*, leading to an overall infidelity of $P_{\beta}^{N_{\mathrm{BO}}}$ after N_{BO} successive Bloch oscillations. As shown by the dashed lines in Fig. 3.2(a), the LZ predictions agree with observations on the overall trend with respect to T_{BO} and U_0, but fail to capture any of the non-monotonic behavior.

The alternating local extrema in the N_{BO} efficiency curves are the signatures of multi-path Stückelberg oscillations. Constructive and destructive interference of the contributing paths direct the positions of the local minima and local maxima, respectively. To quantitatively understand our observations, we perform numerical simulations of a single particle evolving in the Hamiltonian of Eq. (3.4). (See 3.6 for more details). We additionally incorporate a small contribution from the spontaneous scattering rate R_s (see Eq. (2.10)) with the multiplicative factor $\exp[-0.5R_s(\alpha t_{\text{ramp}} + N_{\text{BO}}T_{\text{BO}})]$, where the factor of 0.5 is because the average intensity experienced by delocalized atoms in the optical lattice is half the peak intensity [55]. The numerical factor $\alpha = 0.74$ accounts for the specific shape of intensity ramps used. The good agreement of these simulations (thin solid lines in Fig. 3.2(a)) with our observations indicates a high degree of coherence in our MPSI.

The interference patterns in Fig. 3.2(a) represent MPSI measurements of Stückelberg phase accumulation during BO sequences. For Bloch oscillations starting in the ground band, ϕ_S is the relative phase caused by the difference in action between a path that traverses on $b = 1$ and another that traverses on $b = 0$. This phase difference can be evaluated from the energy difference between the paths indicated by the shaded region in Fig. 3.1(a) as

$$\phi_S^{(b)}(U_0) = \frac{E_r T_{\text{BO}}}{\hbar}\mathcal{I}^{(b)}\,, \tag{3.5}$$

$$\mathcal{I}^{(b)} = \frac{1}{2E_r}\int_{-1}^{1}[E^{(b+1)}(q,U_0) - E^{(b)}(q,U_0)]dq\,, \tag{3.6}$$

where $E^{(b)}(q, U_0)$ is the b$^{\text{th}}$ energy band for lattice depth U_0. Therefore, the integral in Eq. (3.6) represents the average bandgap over one Brillouin zone for a given lattice depth. The location of the pronounced interference minima can be estimated by setting the Stückelberg phase ϕ_S during one BO to an even multiple of π, corresponding to constructive interference into $b = 1$ or *coherent* depletion from $b = 0$. The first and second minima locations are determined by the values of T_{BO}, which solve

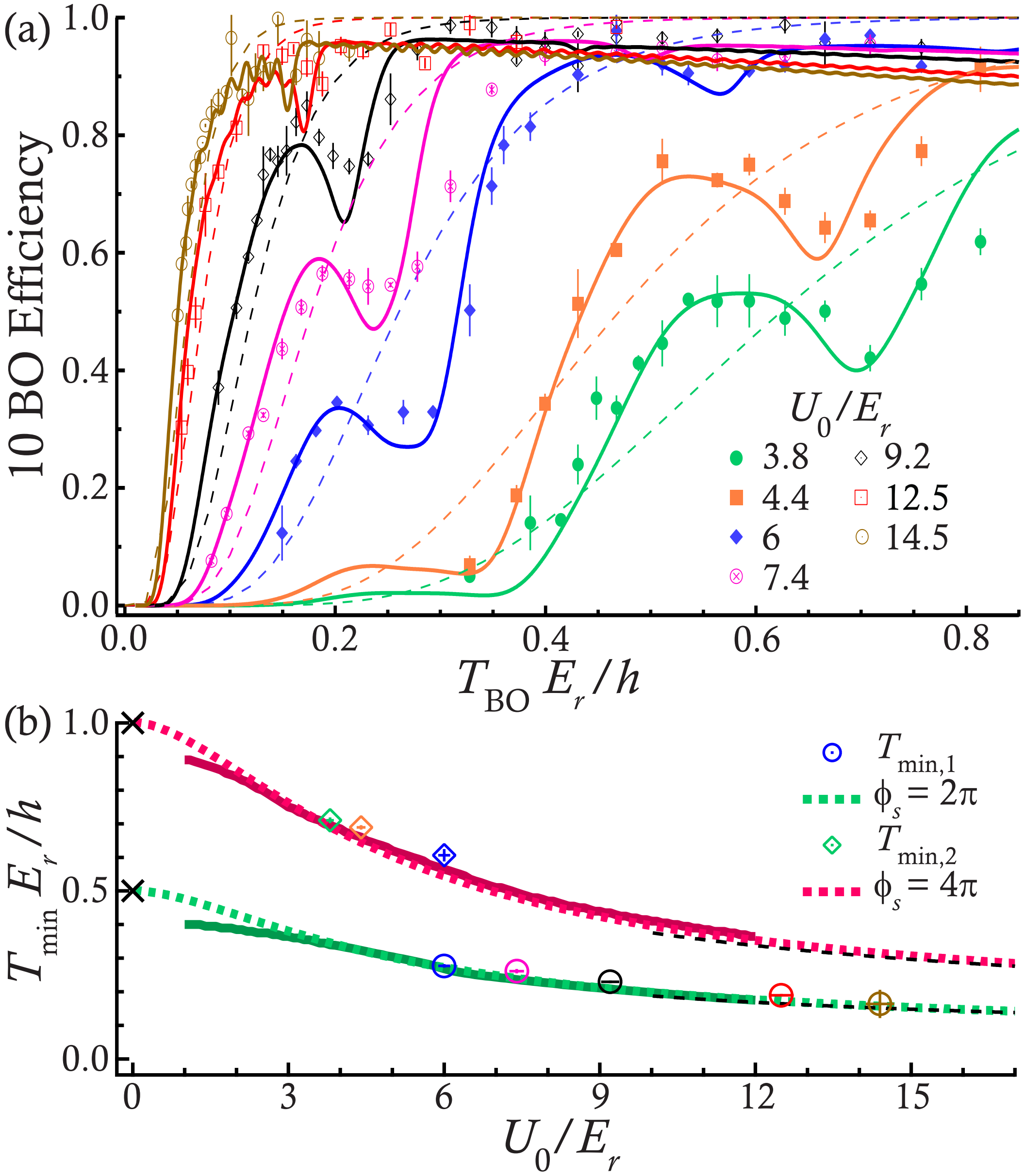

Figure 3.2: Ground band MPSI signals. (a) Observed 10 BO efficiency for various T_{BO} and U_0. Solid lines show the corresponding numerical simulations of Eq. (3.4), including spontaneous scattering. Dashed lines show predictions of the Landau-Zener model. (b) Locations of first ($T_{\mathrm{min},1}$) and second ($T_{\mathrm{min},2}$) Stückelberg oscillation minima as a function of depth. Markers are extracted from experimental data shown in (a) while solid lines are produced from numerical simulations. Colored dotted lines correspond to setting $\phi_S = 2\pi$ and 4π in Eq. (3.5) for $b = 0$. The T_{min} predictions for a free-particle ($U_0 \to 0$) are shown by the black crosses and for the harmonic approximation ($U_0 \to \infty$) by the black dashed lines.

$\phi_S = 2\pi$ and 4π resonance conditions, respectively. These solutions of Eq. (3.5) are shown as the solid lines in Fig. 3.2(b), in clear agreement with the experimentally observed minima locations $T_{\mathrm{min},1}$ and $T_{\mathrm{min},2}$. The dotted lines result from the numerical simulation of Eq. (3.4) and show excellent agreement with the Stückelberg phase calculations using Eq. (3.5), except at the lowest depths. The deviations for $U_0 \lesssim 3E_r$ arise from the contribution of the non-dynamical Stokes phase [56, 57, 58, 59], which only contributes at the avoided crossing region.

The fact that Eq. (3.5) accurately predicts the signal minima, reaffirms a resonant effect also found in other multi-path matter-wave interference phenomena such as the temporal Talbot effect [60] and the quantum kicked rotor [61]. In the regime of large lattice depths, which are more advantageous for large momentum transfer, these resonances remain pronounced. This is somewhat surprising because for larger depths, i.e., $U_0/E_r > 10$, the bandwidths of the first two bands become narrow, and the avoided crossing region is not sharply defined. A reasonable but incorrect conclusion could be that the timings for such resonances would become obscured.

Instead, for the large depth regime, intuition can be gained from the position-space picture and spatial tunneling into neighboring lattice sites. The position-space visualization for $T_{\mathrm{min},1}$ is shown in Fig. 3.1(d). The values of U_0 and T_{BO} used to generate the potential indicate a resonant tunneling loss process into nearest neighbor sites corresponding to a 2π phase difference after 1 BO in $b = 0$ and $b = 1$. Likewise, $T_{\mathrm{min},2}$ corresponds to a coherent resonant tunneling process to the next-nearest neighbor at half the lattice tilt as $T_{\mathrm{min},1}$. The delocalized Bloch states are well described by localized Wannier states in this tight-binding limit, assuming the absence of a linear potential. When the linear potential from a constant force is included, the Wannier-Stark description is more appropriate [62], and the atomic position-space wave function is again delocalized.

3.3.2 Excited band MPSI

Our group has recognized the usefulness of Bloch oscillations in excited Bloch bands as an atom-optics tool (Ref. [55]). In that spirit, we pursued an investigation of the applicability of multi-path Stückelberg interferometry towards measuring BO phases in excited bands as well. For this experiment, we modify the MPSI sequence (Fig. 3.1(a)) by loading the atomic cloud away from avoided crossings at $q = 1/2$ in $b = 1$ so that the Bloch oscillations start exclusively in the first excited band (see Chapter 2). The results for two different lattice depths are shown in Fig. 3.3. The observed Stückelberg patterns are similar to those seen in the ground band and are again in good agreement with the numerical simulations.

Since the avoided crossings between $b = 1$ and $b = 2$ feature smaller energy gaps than those between $b = 1$ and $b = 0$ for any lattice depth, more amplitude from $b = 1$ can transfer to $b = 2$ than to $b = 0$. We would thus expect that the MPSI signal is dominated by the amplitudes in $b = 1$ and $b = 2$ rather than $b = 1$ and $b = 0$. We verify this by comparing the locations of the interference minima $T_{\mathrm{min},1}$ to the condition $\phi_S = 2\pi$ with $b = 1$ in Eq. (3.5) (see Fig. 3.3 inset). A curious high-frequency oscillation is also present in the numerical simulation with a weak amplitude below our experimental detection limit. It can be attributed to the phase accumulation between paths that remain in $b = 1$ and $b = 2$ throughout the MPSI. Ground band BO simulations also display fast oscillations for the largest depth data, $U_0/E_r = 14.5$, in Fig. 3.2(a). The periodicity of these fast oscillations scales with $T_{\mathrm{min}}/N_{\mathrm{BO}}$, making the large depth interference patterns reminiscent of a multi-slit diffraction pattern.

3.4 Large Momentum Transfer Limit

This work extends beyond earlier demonstrations with ultracold atoms that explored two-path ($N_{\mathrm{BO}} = 2$) Stückelberg interference [63, 56]. We show that Stückelberg

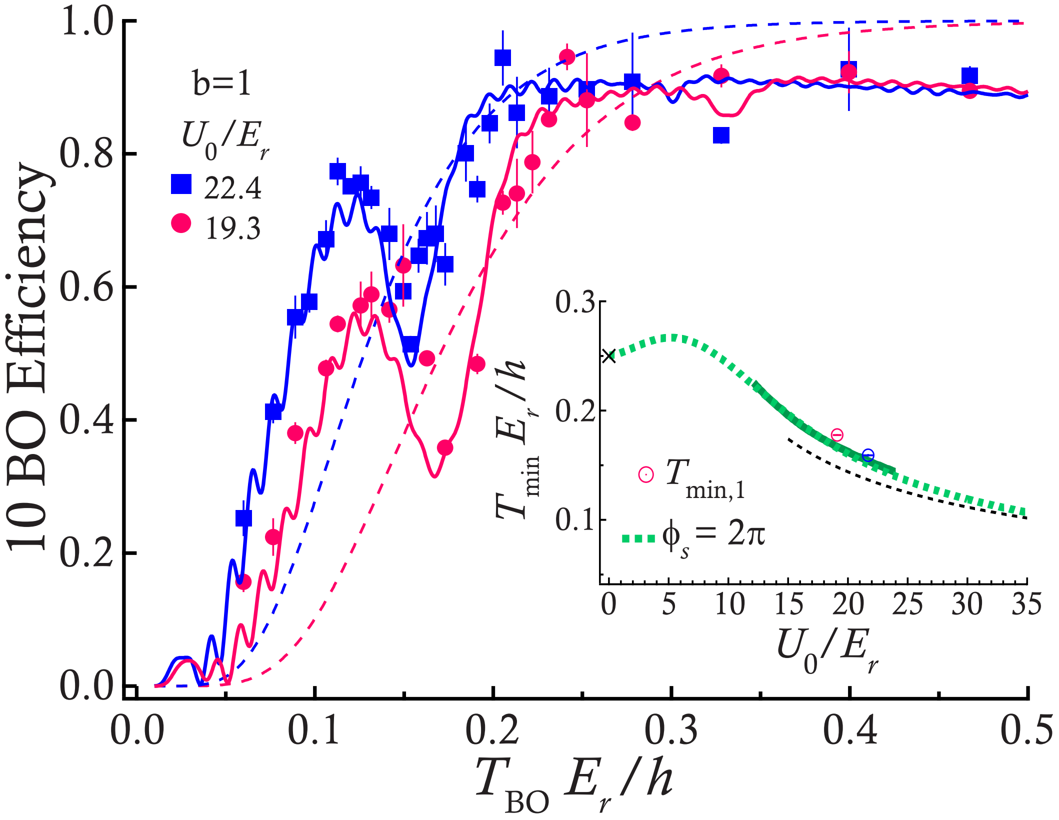

Figure 3.3: MPSI signal for excited band. Main figure shows the observed 10 BO efficiency variation with T_{BO}, for BOs starting in $b = 1$ and two different U_0. Solid lines show corresponding numerical simulations of Eq. (3.4), including spontaneous scattering. Dashed lines show predictions of the Landau-Zener model. The inset shows the location of Stückelberg oscillation minima $T_{\mathrm{min},1}$ as a function of depth. Markers and solid lines are extracted from experimental data shown in the main figure and numerical simulations. The colored dotted line corresponds to setting $\phi_S = 2\pi$ in Eq. (3.5) for $b = 1$. The $T_{\mathrm{min},1}$ prediction for a free-particle ($U_0 \to 0$) is shown by the black cross and for the harmonic approximation ($U_0 \to \infty$) by the black dashed line.

interference signals persist for at least $N_{\mathrm{BO}} = 50$, which is well within the regime of relevance for precision atom interferometry using large momentum transfer. We exploit this newly developed MPSI tool to investigate the variation of the MPSI signal in $b = 0$ for LMT-BOs as N_{BO} is increased. For an apples-to-apples comparison, we analyze the raw data and simulations in terms of "per-BO efficiency", defined as the $(1/N_{\mathrm{BO}})^{\mathrm{th}}$ power of the measured N_{BO}-efficiency.

As schematically shown in Fig. 3.1(a) and discussed in section 3.2, the MPSI involves $> 2^{N_{\mathrm{BO}}-1}$ interfering paths. Even assuming perfectly coherent evolution, we find that this leads to a saturation of the MPSI signal in the LMT limit as $N_{\mathrm{BO}} \to \infty$. In Fig. 3.4(a), we show the evolution of efficiency per BO as N_{BO} is varied for a fixed BO period. In order to increase the dynamic range for this study, the T_{BO} and U_0 are chosen near a strong interference minimum, leading to an observation of the growth of Stückelberg visibility. The signal starts to saturate at $N_{\mathrm{BO}} \approx 10$, reflecting the fact that even though the number of paths contributing to it exponentially grows per subsequent BO, the signal in $b = 0$ is composed primarily of paths that were generated only within the previous 10 BOs. The numerical simulation (points joined by lines) is in good agreement with observations. Whereas the steady-state behavior of Bloch oscillation infidelity has been described in previous work [64, 65], these observations reveal the steady-state behavior of Stückelberg fringes. The deviation from the LZ result (dashed line) grows with increasing N_{BO}. The LZ model would be a flat line, but is altered by spontaneous scattering from the finite pulse duration of the optical lattice.

The steady state behavior ($N_{\mathrm{BO}} \to \infty$) of MPSI is captured in Fig. 3.4(b), where we show a representative MPSI signal for $N_{\mathrm{BO}} = 50$ at a similar depth as 3.4(a). Clearly, the visibility remains strong and the agreement with the theoretical model is excellent, with a very small contribution from spontaneous scattering. The vertical dashed line marks the T_{BO} location of the data taken in Fig. 3.4(a). The theoretical curve shown in Fig. 3.4(c) is obtained from the numerically calculated

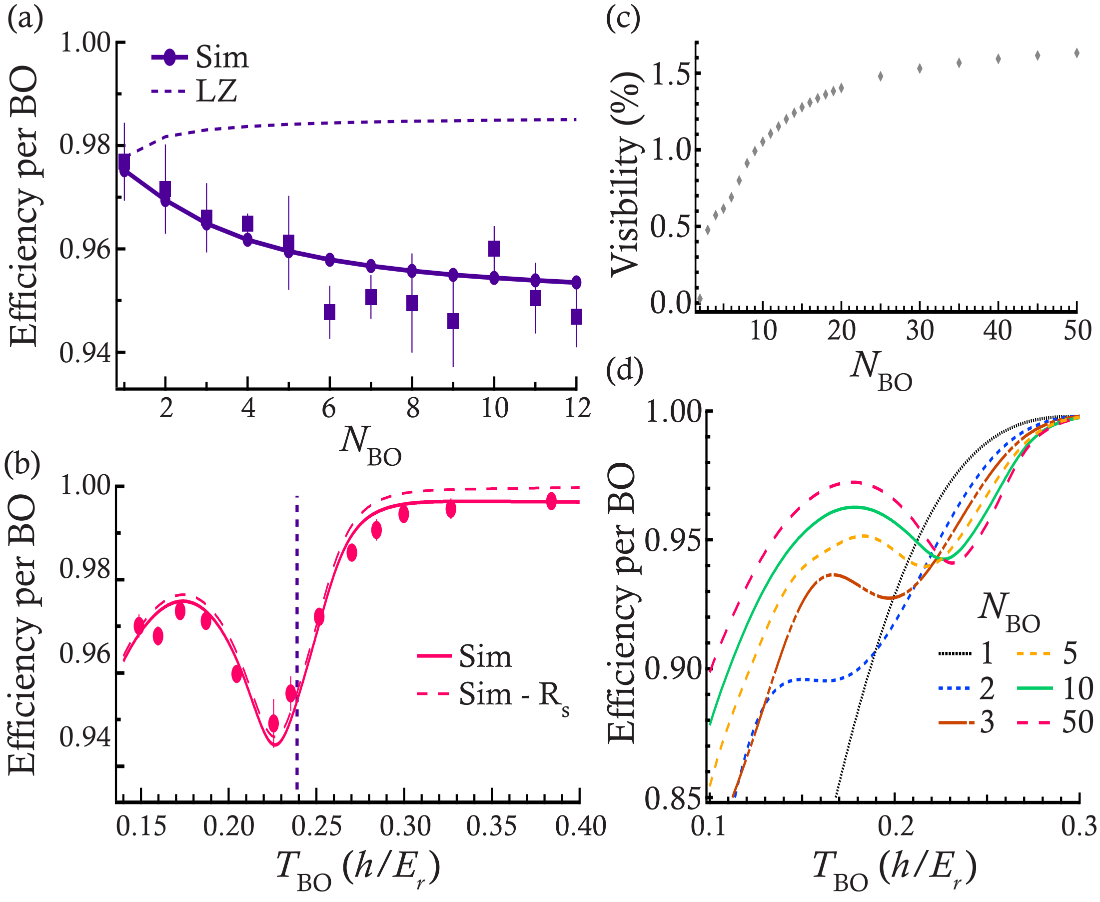

Figure 3.4: Evolution of the Stückelberg interference visibility with growing N_{BO}. The lattice depth is fixed at $U_0/E_r = 8$ unless otherwise stated (a) Per-BO efficiency vs N_{BO} at fixed $T_{\mathrm{BO}} = 0.24(h/E_r)$. Experimental data are shown as square markers and corresponding numerical simulations, including spontaneous scattering as points connected by lines. The dashed line is the Landau-Zener prediction including spontaneous scattering. (b) MPSI signal displayed as per-BO efficiency for an $N_{\mathrm{BO}} = 50$ LMT-BO sequence with $U_0/E_r = 8.3$. The solid (dashed) curve represents the corresponding numerical simulation with (without) spontaneous scattering. The vertical dashed line marks the T_{BO} value in (a), which is near the $T_{\mathrm{min},1}$ point. (c) The visibility of the MPSI signal grows quickly for the first few BOs, but the growth slows down for $N_{\mathrm{BO}} \gtrsim 10$. (d) Per-BO efficiency curves simulated for various N_{BO} up to 50.

per-BO efficiency for different values of N_{BO} while keeping U_0 fixed. The visibility is defined as (Max − Min) / (Max + Min) where Max and Min refer to the values of the local extrema up to the first interference minima. A few representative numerical simulations are shown in Fig. 3.4(d). The visibility curve shows us that $N_{\mathrm{BO}} \approx 10$ is an inflection point, after which the size of the interference effect grows slowly, because of diminishing contributions from paths that consist of several LZ tunneling events. Furthermore, Fig 3.4(d) shows us that the first interference minima gets dragged to shorter T_{BO} with decreasing N_{BO} below the inflection point. As expected, the interference effect suddenly disappears at $N_{\mathrm{BO}} = 1$. There is minimal change in the interference minima location for values of N_{BO} above the inflection point.

3.4.1 LMT-BO with one hundred Bloch oscillations

In Fig. 3.5 we show the MPSI signal as per-BO efficiency for a large depth $U_0/E_r = 25.5$ and large $N_{\mathrm{BO}} = 100$, corresponding to a $200\hbar k$ LMT-BO sequence. The numerical simulation indicates the presence of Stückelberg resonances with narrow widths. Although the widths are narrow and visibility small for larger depths, we see that the first Stückelberg minimum calculated from Eq. (3.5) accurately predicts $T_{\mathrm{min},1}$ from the simulation. The data demonstrates efficiencies of at least 0.9985 per BO are reached for lattice depth of $U_0/E_r = 25.5$ and $T_{\mathrm{BO}} = 0.08(h/E_r)$ (2.13 ms for 100 BOs). This scales to an overall efficiency of 0.47 for $N_{\mathrm{BO}} = 500$ ($1000\,\hbar k$ momentum transfer) in 10.7 ms.

3.5 Experimental Details

Details of the experimental apparatus can be found in Chapter 2. In this section, we provide more specific experimental details about the optical lattice and BEC used for this study. We describe the most relevant experimental controls and some aspects of sample preparation and detection of the Bose-Einstein Condensate.

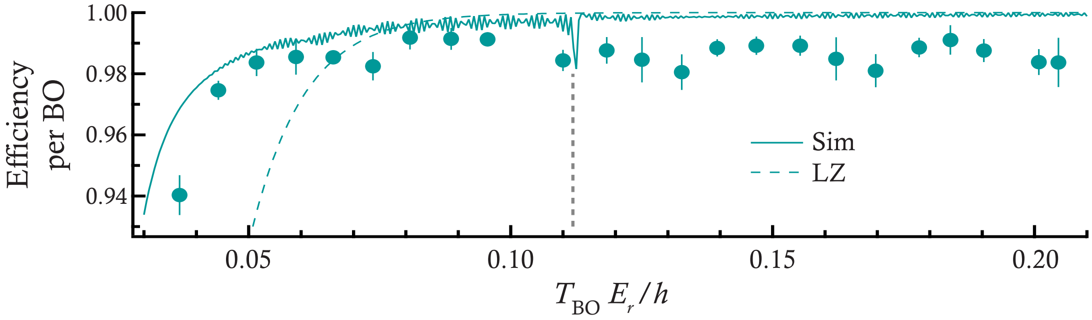

Figure 3.5: MPSI signal displayed as per-BO efficiency for an $N_{\mathrm{BO}} = 100$ LMT-BO sequence with $U_0/E_r = 25.5$. The solid curve shows the corresponding numerical simulation, while the dashed curve is the LZ prediction. The vertical dashed line marks the first Stückelberg minimum corresponding to $T_{\mathrm{min},1}$.

3.5.1 Optical lattice

The optical lattice is formed by two counter-propagating laser beams with a detuning of $\Delta/\Gamma \simeq -3500$ relative to the ${}^1S_0 \to {}^3P_1$ intercombination transition in Yb with wavelength $\lambda_L = 556\,\mathrm{nm}$ and linewidth $\Gamma = 2\pi \times 182\,\mathrm{kHz}$. The angular frequency difference δ between the two beams is controlled using a pair of acousto-optic modulators driven by a corresponding pair of direct digital synthesizers (DDSes).

The inset of Fig. 3.1(a) sketches out the experimental sequence. During the ramp time $t_{\mathrm{ramp}} = 300\,\mu\mathrm{s}$, the lattice depth smoothly rises from 0 to U_0, while a gravity-compensating frequency chirp $\dot{\delta} = \dot{\delta}_g$ is applied with one of the DDSes. The depth is then maintained at U_0 for a time $N_{\mathrm{BO}} \times T_{\mathrm{BO}}$ while the chirp is set to $\dot{\delta} = \dot{\delta}_g + \dot{\delta}_{\mathrm{BO}}$. Finally, the intensity is ramped down to 0 over $t_{\mathrm{ramp}} = 300\,\mu\mathrm{s}$ with chirp $\dot{\delta} = \dot{\delta}_g$. Varying $\dot{\delta}_{\mathrm{BO}}$ also controls the BO period since $T_{\mathrm{BO}} = 2\hbar k_L/ma$ where m is the inertial mass of Yb, a is the lattice acceleration, and $k_L = \pi/d$ is the laser wavenumber. It follows that $T_{\mathrm{BO}} = 8E_r/(\hbar\dot{\delta}_{\mathrm{BO}})$ so that control of $\dot{\delta}$ allows T_{BO} to be an independent variable for many of the experiments described above. Another independent variable, N_{BO}, is easily controlled by our sequence timing.

A detailed temporal profile of the pulse intensity is shown in Fig. 3.1(c) as a representative oscilloscope trace from a pick-off beam on a monitoring photodiode. During the portion of the experiment sequence when the depth is maintained constant, we observe a 1.9% relative intensity variation. We also see a long-term variation on the lattice depth of $\lesssim 10\%$ between multiple experimental runs within some data sets. This was measured by taking lattice depth calibrations via Bragg diffraction before the start and at the end of a data run. The calibrations allow us to take U_0 as our last independent variable within some variation.

We aligned the lattice to the atoms by optimizing the diffracted orders from $10\,\mu$s Kapitsa-Dirac pulses. The orientation of the lattice with respect to gravity was estimated as 5 mrad by utilizing the reflection from a cup of water placed on the optical table. For all the experiments reported here, the lattice depth inhomogeneity seen by the falling atoms due to this small angle is $< 10^{-5}$—negligible compared to the aforementioned intensity noise.

The gravity chirp $\dot{\delta}_g = 2\pi g/d$ makes the lattice stationary in the co-moving frame of the falling atoms. Gravity points in the $-\hat{y}$ direction in our experiment (see Fig. 3.1(b)). The gravity chirp is tuned experimentally through optimization of Kapitsa-Dirac diffraction after a long expansion time t_{exp} out of the trap. This yielded $\dot{\delta}_g = -2\pi \times 35.1$ kHz/ms, corresponding to $g = 9.76$ m/s^2 which is $< 0.5\%$ below the nominal value of $g = 9.8$ m/s^2 in Seattle. The corresponding potential systematic on T_{BO} is negligible even for the longest BO periods represented in this work.

3.5.2 Atomic interactions

The BEC of ^{174}Yb formed in the ODT contains about 7×10^4 atoms, with repulsive mean-field interactions arising from the s-wave scattering length $a_s = 5.6\,$nm. We measure the associated interaction energy to be $k_B \times 40\,$nK using absorption imaging after a long time-of-flight (TOF) when all of this energy has been converted into kinetic energy. The minimum expansion time out of the ODT before the optical

N_{BO}	100 BO	50 BO	1-20 BO
t_{exp}	9.5 ms	7 ms	3 ms
TOF	1 ms	4 ms	12 ms

Table 3.1: Expansion time t_{exp} between ODT switch off and lattice turn on and time-of-flight (TOF) between lattice turn off and absorption imaging used for different sets of experiments reported in this work.

lattice is turned on (see Table 3.1) is $t_{\mathrm{exp}} = 3\,\mathrm{ms}$, sufficiently large (see Ref. [66]), to ensure negligible interactions.

The expansion time prior to the lattice turn-on (t_{exp}), and the time-of-flight (TOF) after the lattice is adiabatically turned off, are adjusted depending on N_{BO} due to technical limitations of the imaging setup. In Table 3.1 we summarize the three different t_{exp} and TOF settings used in this work.

3.6 Numerical Simulations

Here, we detail the Bloch oscillation simulation algorithm, which was utilized to generate the theory plots in Figs. 3.2, 3.4, 3.3, 3.5,and 3.7. The Bloch oscillation simulatuation algorithm, or BORK algorithm, was primarily developed by Andrew Ivanov. The last figure also considers a complementary model based on Wannier-Stark states of a washboard potential, which was developed by Florian Fitzek.

3.6.1 Bloch oscillation simulation algorithm

The basic premise of the algorithm uses Floquet-Bloch operators to exploit the discrete translation symmetry of $\mathcal{PT}$-symmetric Bloch bands. For the BO-induced quasi-momentum sweep, we implement a Runge-Kutta numerical ODE solver. We call this algorithm Bloch Oscillation Runge-Kutta, or BORK for short. The effect of the quasimomentum sweep can be computed by integrating the time-dependent Schrödinger equation (TDSE), Eq. (3.7), with the time-dependent Hamiltonian given in Eq. (3.8):

$$i\hbar\partial_t \left|\Psi\right\rangle = \hat{H}(t)\left|\Psi\right\rangle \,, \tag{3.7}$$

$$\hat{H}(t) = E_r \begin{pmatrix} (q+2N_{\max})^2 & \nu/4 & & & \\ \nu/4 & \ddots & \ddots & & \\ & \ddots & q^2 & \ddots & \\ & & \ddots & \ddots & \nu/4 \\ & & & \nu/4 & (q-2N_{\max})^2 \end{pmatrix}, \tag{3.8}$$

where $q = q(t)$ and $U_0 = \nu E_r$ is the lattice depth. The infinite-dimensional Hilbert space is truncated to $N_{\max} > N_{\mathrm{BO}}/2$, reducing its reach to operations on a $2N_{\max}+1$ dimensional subspace.

Let $\hat{H}(t) = \hat{H}_0 + \hat{D}(t)$, where $H_0 = H(0)$. Assuming $q(0) = 0$,

$$\hat{D}(t) = \hat{H}(t) - \hat{H}_0 = E_r(q^2\hat{I} - 4q\hat{N})\,, \tag{3.9}$$

where

$$\hat{N} = \begin{pmatrix} -N_{\max} & & & & \\ & \ddots & & & \\ & & 0 & & \\ & & & \ddots & \\ & & & & N_{\max} \end{pmatrix}. \tag{3.10}$$

Let

$$\left|\Psi(t)\right\rangle = \sum_i c_i(t)\left|\psi_i\right\rangle e^{-i\omega_i t}, \tag{3.11}$$

be the state vector in the eigenbasis of H_0 with $c_i(t)$ being some time-dependent complex coefficients. Then, the TDSE

$$i\hbar\partial_t \left|\Psi\right\rangle = (\hat{H}_0 + \hat{D}(t))\left|\Psi\right\rangle \,, \tag{3.12}$$

reduces to

$$\dot{c}_k = -\frac{i}{\hbar}\sum_{i,j}[D_j\langle j|\psi_i\rangle\langle\psi_k|j\rangle^{-i(\omega_i-\omega_k)t}]c_i\,. \tag{3.13}$$

where $|j\rangle$ and D_j are the eigenvectors and eigenvalues of $\hat{D}$ with the latter running along the diagonal top to bottom.

Equation (3.13) can be simplified as

$$\dot{c}_k = -\frac{i}{\hbar}\sum_{i}[\langle\psi_k|\hat{D}|\psi_i\rangle^{-i(\omega_i-\omega_k)t}]c_i\,, \tag{3.14}$$

which leads to the following matrix first-order differential equation for $C = (c_1, \cdots, c_{\mathrm{dim}})^T$, where $U = (\psi_1, \cdots, \psi_{\mathrm{dim}})$:

$$\begin{aligned}\dot{C} &= -\frac{i}{\hbar}e^{iU^\dagger\hat{H}_0Ut}U^\dagger\hat{D}Ue^{-iU^\dagger\hat{H}_0Ut}C\\ &= -i\Omega_r e^{iU^\dagger\hat{H}_0Ut}U^\dagger\hat{(}q^2\hat{I} - 4q\hat{N})Ue^{-iU^\dagger\hat{H}_0Ut}C\\ &= -i\Omega_r(q^2\hat{I} - 4qe^{iU^\dagger\hat{H}_0Ut}U^\dagger\hat{N}Ue^{-iU^\dagger\hat{H}_0Ut})C\,.\end{aligned} \tag{3.15}$$

We represent one BO as a linear sweep of q from $q = 0$ to $q = 2$ in the periodic Brillouin zone picture, shown in Figure. 3.6, such that

$$q(t) = a_{\mathrm{lat}}t = 2t/T_{\mathrm{BO}}\,. \tag{3.16}$$

Integrating Eq. (3.15) for $t \in [0, T_{\mathrm{BO}}]$ gives c_i in the energy basis of H_0. To obtain actual band amplitudes we need to translate them into the energy basis of $H(q = 2)$, which in practice is very easy: the eigenstates of $H(q = 2)$ are obtained from the eigenstates of H_0 with a simple gauge transformation by a downward shift of 1 position for all $|\psi_i\rangle$ (see Figure 3.6).

Equation (3.15) in unitless form with $\tau = tE_r/h$ is

$$\dot{C} = -i2\pi q(\tau)\left(q(\tau)\hat{I} - 4e^{i2\pi U^\dagger\tilde{H}_0U\tau}U^\dagger\hat{N}Ue^{-i2\pi U^\dagger\tilde{H}_0U\tau}\right)C\,, \tag{3.17}$$

where $q(\tau) = 2\tau/\tilde{T}_{\mathrm{BO}}$ and $\tilde{H}_0 = \hat{H}_0/E_r$. It can be readily integrated with an adequate ODE solver such as RK4. Note that the first term in parentheses in Eq. (3.17) can be

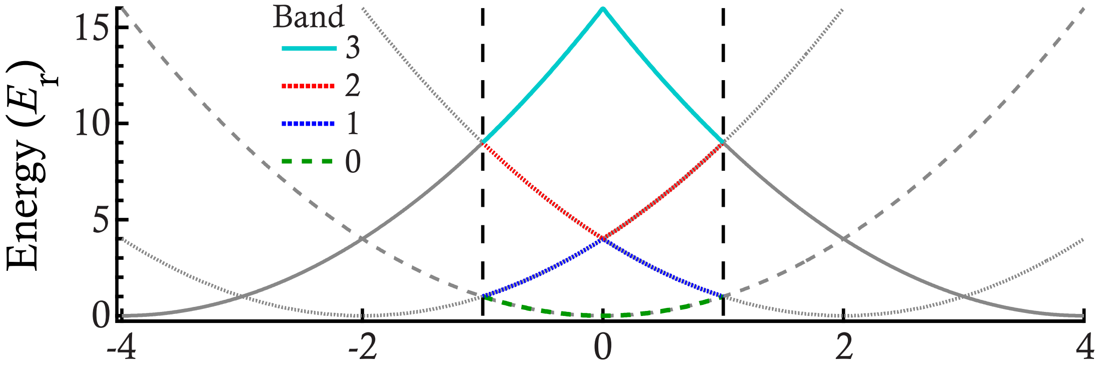

Figure 3.6: Repeated Brillouin zone picture with parabolas corresponding to the dispersion relation of uncoupled ($\nu \rightarrow 0$) states. The dashed lines are the periodic boundary condition of the Brillouin zone edge, which demonstrate the relationship between diagonal matrix elements of $\hat{H}(q = 2)$ and $\hat{H}(q = 0)$: $H(q = 2)_{i,i} = H(q = 0)_{i-1,i-1}$. This means that if $|\psi_i\rangle$ is an eigenstate of $H(q = 0)$ corresponding to i^{th} band, then $|\downarrow \psi_i\rangle$, where $\downarrow$ denotes a cyclic downward shift of all state vector components by one position is an eigenstate of $H(q = 2)$ corresponding to the same band.

dropped since it only produces a global phase. Below, we outline the algorithm for simulating N_{BO} Bloch oscillations (c_i^0 are initial band populations at $t = 0$ and RK4 denotes numerical integration):

```
$C \leftarrow (c_1^0, \cdots, c_{\mathrm{dim}}^0)$
for $n \leftarrow 1, N_{\mathrm{BO}}$ do
    $C(\tilde{T}_{\mathrm{BO}}) \leftarrow \mathrm{RK4}(\dot{C}(\tau),\, C(0),\, [0..\tilde{T}_{\mathrm{BO}}])$
    $\Psi \leftarrow \sum c_i \left|\psi_i\right\rangle e^{-i2\pi\tilde{\omega}_i\tilde{T}_{\mathrm{BO}}}$
    for all $\psi_i$ do
        $c_i \leftarrow \langle \downarrow \psi_i | \Psi \rangle$
    end for
end for
```

To facilitate an arbitrary initial quasimomentum, Eq. (3.17) is modified to

$$\dot{C} = -i2\pi(q(\tau) - q_0)\left((q(\tau) + q_0)\hat{I} - 4e^{i2\pi U^{\dagger}\tilde{H}_0 U\tau} U^{\dagger}\hat{N}U e^{-i2\pi U^{\dagger}\tilde{H}_0 U\tau}\right)C\,, \tag{3.18}$$

where $q(\tau) = q_0 + 2\tau/\tilde{T}_{\mathrm{BO}}$, and the computational basis $\left|\psi_i\right\rangle$ is composed of the eigenfunctions of $H(q = q_0)$.

Calculation of the Floquet-Bloch operator

We define the Floquet-Bloch operator [67] in the basis of the eigenstates of $\hat{H}(0)$ as follows:

$$\hat{U}_B = \mathcal{T}\left\{\exp\left[-\frac{i}{\hbar}\int_0^{T_{\mathrm{BO}}} \hat{H}(t)dt\right]\right\}\,, \tag{3.19}$$

where $\mathcal{T}$ indicates time ordering of the exponential operation.

Direct evaluation of the Floquet-Bloch operator is quite non-trivial since, as a consequence of the time-ordering constraint, it requires computing Dyson series. However, utilizing the algorithm described herein, we can very efficiently and with high accuracy compute $\hat{U}_B$ indirectly. To that end, let's denote one iteration of the algorithm with operator $\hat{U}_1$. Recognizing that $\hat{U}_1$ is defined over a vector space of instantaneous Bloch bands which we denote as $|n\rangle$ with $n \in \mathbb{N}$, where the natural numbers $\mathbb{N}$ are inclusive of 0. In the preceding discussion, c_n represented the complex coefficients of the populations in each band. Then we can write

$$\hat{U}_B = \sum_{mn} \alpha_{mn} |m\rangle\langle n|, , \tag{3.20}$$

where α_{mn} are the matrix elements to be determined. Clearly,

$$\hat{U}_B \,|n\rangle = \hat{U}_1 \,|n\rangle \implies \sum_m \alpha_{mn} \,|m\rangle = \hat{U}_1 \,|n\rangle \ . \tag{3.21}$$

Therefore,

$$\alpha_{mn} = \langle m| \,\hat{U}_1 \,|n\rangle \ , \tag{3.22}$$

which means that full evaluation of $\hat{U}_B$ reduces to N_{max} applications of U_1 operationally defined in the form of the computational algorithm discussed earlier, with N_{max} being the maximal number of Bloch bands to be accounted for. Once U_B is computed for specific values of lattice depth νE_r and Bloch period T_{BO}, it can be used for calculating band amplitudes over an arbitrary number of periods N_{BO} starting from an arbitrary initial state $|\Psi_B(t=0)\rangle$, as follows:

$$|\Psi_B(t = N_{\text{BO}}T_{\text{BO}})\rangle = \hat{U}_B^{N_{\text{BO}}} \,|\Psi_B(t=0)\rangle \ , \tag{3.23}$$

where the final amplitudes in $|\Psi_B(t = N_{\text{BO}}T_{\text{BO}})\rangle = \sum_{m=0}^{2N_{\text{max}}} c_m \,|m\rangle$ are extracted to reveal the N_{BO}-efficiency. The per-BO efficiency is evaluated as $\left(c_b^* c_b / \sum_m^{2N_{\text{max}}+1} c_m^* c_m\right)^{1/N_{\text{BO}}}$ for the b$^{\text{th}}$ band. Of course, the results of this process will be identical to explicit integration over N_{BO} by means of the full computational algorithm; However, using the Floquet-Bloch operator is considerably (by orders of magnitude) more efficient and also more accurate than performing explicit numerical integration over many BO.

3.6.2 Comparison with Wannier-Stark approach

Here we compare the output of the numerical simulation described in section 3.6.1 with the Wannier-Stark approach used in Ref. [62]. Both sets of ground band numerical simulations are shown in Fig. 3.7 for parameters similar to those in Fig 3.2(a) in section 3.3.1. We find excellent agreement between the two approaches across a wide range of the U_0 and T_{BO} parameter space. The deviations between the two appear mostly at low T_{BO}, which may arise from adiabaticity considerations, as $T_{\text{BO}} \to 0$. An alternate explanation is that for the shortest T_{BO}, the Wannier-Stark calculations better capture the lattice dynamics than the BO picture, because approximation (3.3) is not reliable.

In our model, the Bloch oscillations are instantly switched on to mimic the fact that the linear frequency sweep switches quickly in a step-like fashion from $\dot{\delta}_g$ to $\dot{\delta}_{\text{BO}}$ and back to $\dot{\delta}_g$ over the MPSI sequence. Section 3.5 provides further details on the experimental sequence. On the other hand, the efficiency curves produced by Fitzek et al. assume an adiabatic change in the ramp rate, while the optical lattice depth ramps up between 0 and U_0. Fig. 4 of Ref. [62] suggests that non-adiabatic ramps would produce additional losses in our experiment, which are not accounted for by the simple Wannier-Stark model.

3.7 Bloch Oscillation Enhanced Interferometry

High-efficiency large momentum transfer tools using Bloch oscillations *within* an atom interferometer constitute what we will call "BO-enhanced" atom interferometry. BO-enhanced interferometers have the potential to create large interferometer space-time areas for the next generation of fundamental physics tests and applications in inertial sensing and gradiometry [68].

3.7.1 Bragg vs. BO LMT efficiency

Bloch oscillations provide an appealing alternative approach for LMT interferometers compared to other techniques such as pulsed Bragg diffraction [69, 70]. The main advantage lies in the highly efficient accelerations possible with BO dynamics when restricted to an isolated energy band. However, this feature is also accompanied

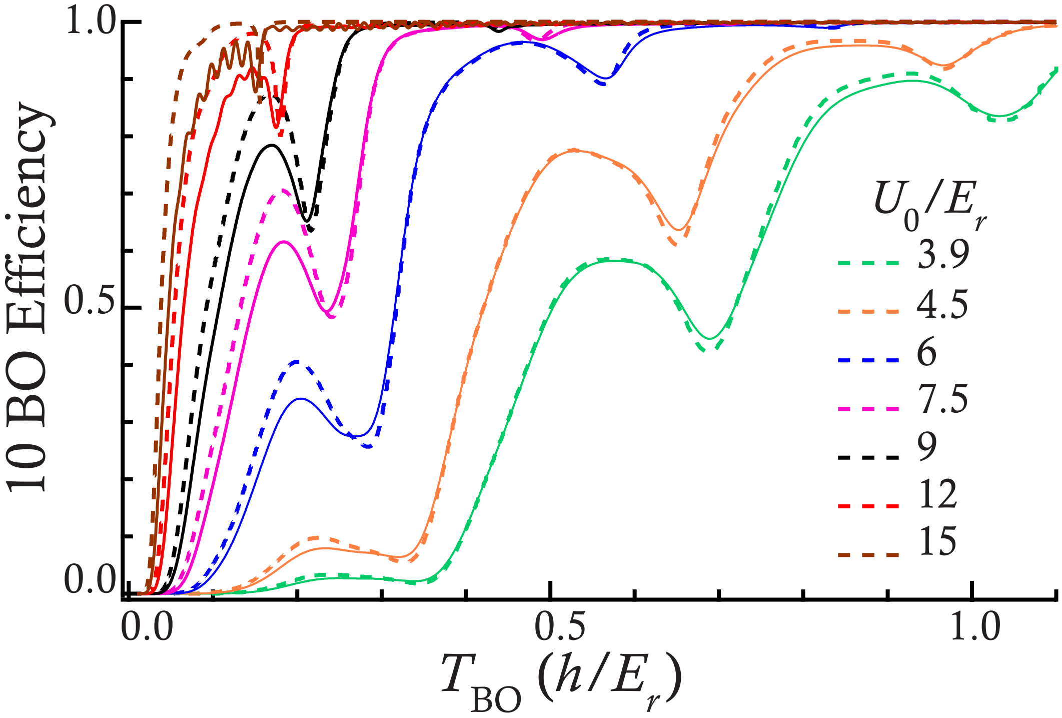

Figure 3.7: Comparison of the numerical simulations used in this work (solid lines) to the Wannier-Stark approach (dashed lines)—see Fitzek et al. 2024—for parameters similar to those in Fig 3.2(a). Both approaches have similar results for locations of local minima $T_{\min}$, but efficiencies deviate slightly for the shortest Bloch oscillations as $T_{\mathrm{BO}} \to 0$.

by large relative phase accumulation between multiple bands during the LMT-BO process, inducing Stückelberg phases. Precise control of these phases increases experimental demands to maintain phase stability in a BO-enhanced interferometer. While $1000\hbar k$ level momentum transfer has been demonstrated with BOs [8, 71], BO-enhanced interferometry[2], which has been limited to relatively modest momentum separation ($< 100\hbar k$) [75, 76, 72, 73, 74]. Using our MPSI tool, we find high coherence even for long BO sequences, suggesting that LMT-BO enhanced interferometry is possible beyond the best experimental demonstrations thus far.

Fast and highly efficient Bloch oscillations are achieved at high lattice depths. The $U_0/E_r = 14.4$ data shown in Fig. 3.2(a) indicates a momentum transfer efficiency of 0.995 per $\hbar k$ for $T_{\mathrm{BO}} \simeq 46\,\mu$s. We see in Fig. 3.5 that we achieve an even higher LMT-BO efficiency of 0.999 per $\hbar k$ for $U_0/E_r = 25.5$ at half the BO period. Extrapolating to $1000\hbar k$ LMT, the fidelity is 0.47 delivered in just 11.5 ms—far better than results previously reported in Ref. [77] with an efficiency of 0.985 per $\hbar k$ achieved in the same atomic species and similar lattice depth with Bragg diffraction. The rate of momentum transfer for the optimized Bragg pulses was $6\hbar k$ with $54\,\mu$s FWHM Gaussian pulses, which is comparable to the momentum transfer rate in the BO case. However, if we extrapolate the Bragg diffraction efficiency to a $1000\hbar k$ LMT, we get 2.73×10^{-7} fidelity, which is untenable. The BO fidelity is more than six orders of magnitude better!

3.7.2 Phase instability with BO enhancement

We now examine the criteria needed for high-precision tests with BO-enhanced interferometers. We consider both the maximal separation in band number ($\Delta b = N_{\mathrm{BO}}$) *and* the relative phase evolution ϕ_{lat} of two paths during an LMT-BO sequence ap-

---

[2] Ground-band BOs have been used to demonstrate a phase-stable $80\hbar k$ interferometer in a guided (non free-space) geometry [72]. Recent work in free-space interferometers has shown even larger momentum splitting with ground-band BOs [73, 74], however, phase stability was demonstrated only up to $20\hbar k$

plied on one of the paths. As a benchmark for the bleeding edge of high-precision interferometry, we take $1000\hbar k$ momentum transfer as a suitable goalpost for the next generation of BO-enhanced interferometers. We also require phase instabilities of $\delta\phi \ll \pi$ for our interferometers, otherwise fringe visibilities would be washed out. Considering the standard deviation of randomly sampled phase contributions between 0 and π, we take $\delta\phi_{\text{lat}} \leq 50\,\text{mrad}$ phase instability, which is more than one order of magnitude smaller, as a constraint for sufficient visibility.

Spurious phases may be a result of variations in lattice depth. At high depth $U_0 \gg E_r$ and for the LMT-limit ($N_{\text{BO}} \gg 10$), we estimate the phase difference with the expression in (3.24) below for wavepackets that span a large number of bands:

$$\hbar\phi_{\text{lat}} \simeq \frac{1}{2} U_0 \times T_{\text{BO}} N_{\text{BO}}\,, \tag{3.24}$$

$$\delta\phi_{\text{lat}} \simeq 2\pi \times \frac{\epsilon}{2}\frac{U_0}{E_r}\frac{T_{\text{BO}} E_r}{h} N_{\text{BO}}\,. \tag{3.25}$$

The factor of half is because in a deep lattice, a $b = 0$ wave packet has an average internal energy of $\approx U_0/2$ compared to delocalized Bloch states. Here, delocalized means the band energy $E^{b=B}(q) \geq U_0$, because a wavepacket in a band $b > B$ would be like that of a free particle. This is easily achieved in the LMT limit because the dispersion is $E^{b \gg B}(q) \approx [2b + (q/\hbar k)]^2\, E_r$, where the wavepacket is effectively in free fall.

As a result, the corresponding phase instability is proportional to the lattice depth variance. Given a relative lattice depth variance of ϵ we expect a phase instability of $\delta\phi_{\text{lat}} \simeq \epsilon\phi_{\text{lat}}$. Using more convenient units we express the phase instability in expression (3.25). For the goalpost of $1000\hbar k$ LMT with $\delta\phi_{\text{lat}} \leq 50\,\text{mrad}$ entertained above and using the parameters for the best LMT rates mentioned above, we require $\epsilon \lesssim 2 \times 10^{-5}$. It would be quite a challenging endeavor to improve our lattice beam intensity variation to this level, especially given that the variation is three orders of magnitude worse at present. One avenue for improved phase stability is to use excited band ($b > 0$) Bloch oscillations at "magic" depths. In previous work from our group

(Ref. [55]), we tuned our lattice intensity to these magic depths and demonstrated a suppression of phase instability induced by lattice depth variation.

3.8 Summary

In this work, we developed a multi-path Stückelberg interferometer with ultracold atoms and used it to study the phase accumulation during a long sequence of BOs. Furthermore, we applied multi-path Stückelberg interferometry in the regimes of large lattice depth ($U_0 \gg E_r$), short Bloch oscillations times ($T_{\mathrm{BO}} \ll h/E_r$), and steady-state behavior ($N_{\mathrm{BO}} \gg 1$). These are the regimes most relevant for an efficient large momentum transfer protocol.

We demonstrated that Bloch oscillation processes can be applied in a highly coherent manner. However, the use of large N_{BO} as LMT beamsplitters is limited by experimental challenges in stabilizing lattice depth beam intensities. Although this study offers a readily available explanation for the interferometric fringe locations, the fringe sharpness requires more clarification. We observe a general trend of increasing sharpness with larger lattice depth and larger momentum transfer.

We believe that the MPSI tool can help optimize atom-optics parameters for BO-enhanced interferometers and can also be used to explore geometric phases in topologically nontrivial band structures [78]. A comparative analysis of BO efficiency optimization with the Wannier-Stark and BO models could help direct future LMT-BO protocols. Lastly, we identify phase instability resulting from lattice depth fluctuations as an important technical challenge for future experiments. These challenges could be addressed by Bloch oscillations using Bloch bands at magic depths [55]. Alternative strategies include symmetric atom interferometer schemes such as those shown in Refs. [73, 74], or alternative LMT approaches such as Floquet atom-optics [79]. I hope that these results may help guide next-generation fundamental physics tests, gravimetry, or inertial sensing with atom interferometry.

Chapter 4

MAGIC BLOCH BAND STABILITY

In this chapter, we will explore the concept of "magic depths" or "magic Bloch-bands" in a one-dimensional optical lattice. We will make an effort to understand magic depths using both a Bloch-band view and a position-space view. We will then apply this understanding towards the visibility of atom interferometry fringes. The canonical commutation relation $[\hat{x}, \hat{p}] = i\hbar$ tells us that both position and momentum bases are informative. (Perhaps it tells us that both are somewhat uninformative). By considering both pictures, I attempt to offer a more complete description of magic depths.

4.1 Magic Depth vs. Magic Wavelength

We define magic depth with analogy to magic wavelengths, which are relevant for atomic clock applications. Timekeeping with atomic clocks involves precision spectroscopic measurements of a narrow-line atomic transition that feed back on the frequency of a resonant laser field. Optical atomic clocks are highly sensitive to perturbations such as Stark shifts from trapping laser fields, which means that the variation of Stark shifts can lead to measurement instability. In some cases, a carefully chosen light color, called a magic wavelength, is tuned so that the Stark shift of both energy levels is the same up to first-order frequency drifts in the presence of this trapping laser field. Calculating Stark shifts can be very cumbersome since multiple nearby energy levels affect the polarizability of each clock state [80]. Magic wavelengths are particularly relevant for optical lattice clocks, where ensembles of atoms are trapped inside multiple lattice sites[1].

Atoms in optical lattices have eigenenergies called Bloch bands. If the band energies fluctuate, this also means that the phase of an atom inside a Bloch band fluctuates. We define the magic *depth* of an optical lattice in the same spirit as the magic wavelength. In other words:

> The magic depth $U_M^{(b)}$, of the b^{th} Bloch band is the crystal lattice depth in which the average band energy $\left\langle E^{(b)} \right\rangle$ becomes first-order insensitive to changes in the lattice depth.

This definition hints at a notable difference between magic wavelength and magic depth, in that the magic depth is unique for each band. The only knowledge we need to calculate the magic depths is the band structure. In our case, the sinusoidal lattice structure generates Bloch bands. Once we choose the lattice depth U, all band energies can be generated numerically. For each band b, the average energy is

$$\left\langle E^{(b)} \right\rangle = \frac{1}{2\hbar k} \oint_{\text{BZ}} E^{(b)}(U, q) dq \,, \tag{4.1}$$

where we apply a closed integral of the quasimomentum q, across one Brillouin zone[2] (BZ). A second difference between magic depth and magic wavelength is that the former is easier to calculate. As we will see below, the calculations of the average energy in Eq. (4.1) for various depths U are all that is needed to determine the magic depth for each band. Since each Bloch band has exactly one magic depth, there are an infinite number of magic depths to choose from.

---

[1] For optical lattice clocks, there is another form of "magic intensity" or "magic depth". For clock states involving electric quadrupole or magnetic dipole transitions [81], or density dependent shifts [82]. The light shift is sensitive to lattice intensity variation which can be reduced with a convenient choice of lattice depth.

[2] This integral can be taken for any closed contour inside of a Brillouin zone. In our case, we are interested in Bloch oscillations so that atoms undergo a linear sweep through a full BZ. We can also consider nonlinear sweeps caused by a time-dependent force, such that the integral generalizes to $\oint E^{(b)}(U, q) F(t) dt/(2\hbar k)$ where $F(t) = dq/dt$ is not necessarily constant.

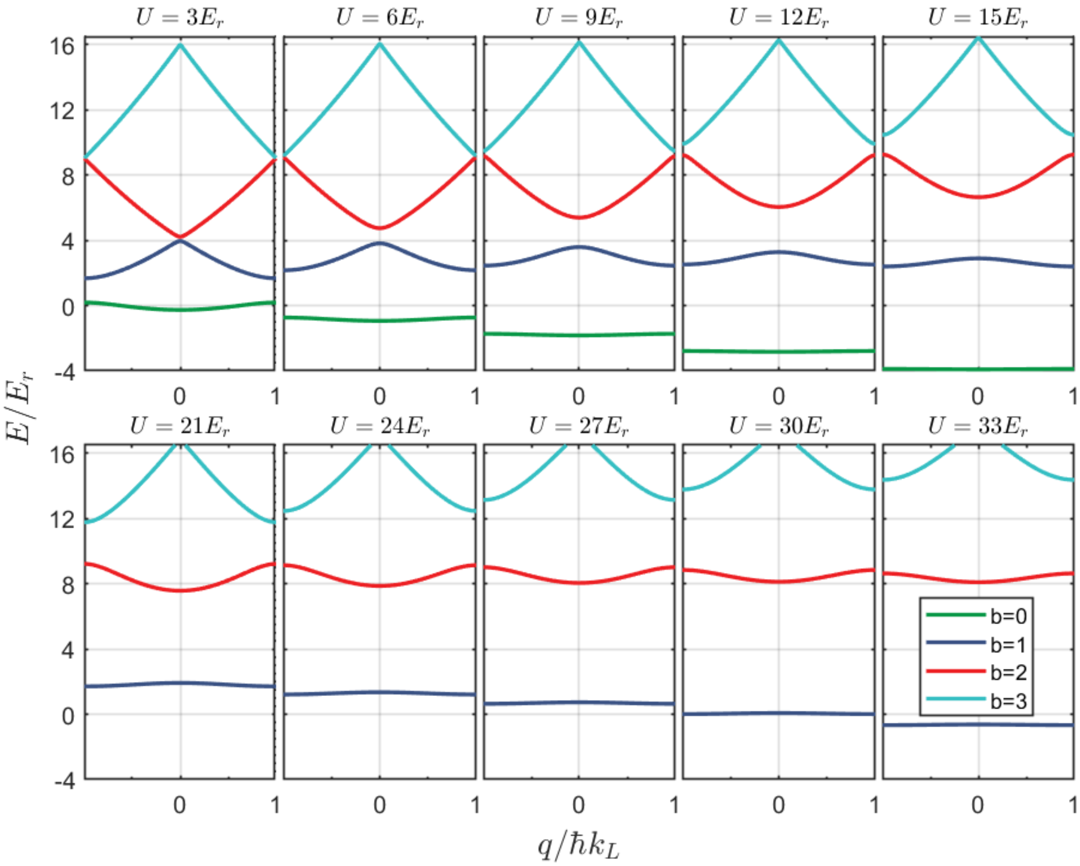

Figure 4.1: The ground (b=0) and three excited (b=1,2,3) Bloch bands shown for a range of lattice depths. Top row: Bloch bands around the first magic depth $U_M^{(1)} = 9.2E_r$. Bottom row: Bloch bands around the 2nd magic depth $U_M^{(1)} = 27.3E_r$.

4.2 Magic Bloch Bands

4.2.1 The turning point

Let's consider first a few Bloch bands at various depths as shown in Fig. 4.1. The top row shows the first few Bloch bands between $U = 3E_r$ and $U = 15E_r$. We can see that the overall the ground band ($b = 0$) drops down as the lattice depth grows. The first excited band ($b = 1$) has some slightly different behavior. We can see that the overall band energy shifts up between $U = 3E_r$ and $U = 9E_r$, then shifts down after increasing the depth further.

We can explain this through level repulsion in degenerate perturbation theory. At the edge of the BZ there is an avoided crossing between the ground and first excited band, which means that the bands pull apart with increasing lattice depth. The degeneracy lifted here is between free particle dispersions with momentum that are $2\hbar k$ different from each other. There is also an avoided crossing between the first and second excited band in the middle of the BZ, corresponding to a degeneracy of free particles with momentum that are $4\hbar k$ apart. We can see that the $b = 1$ and $b = 2$ bands pull apart in the middle of the BZ, which pushes the first extended band to lower energies. The first excited band performs a balancing act because it is pushed by the bands adjacent to it.

The second row of Fig. 4.1 describes a similar balancing act for the second excited band. It is pushed up by the $b = 1$ band in the middle of the BZ and pushed down by the $b = 3$ band at the edge of the BZ. These are the avoided crossings connecting free particle states with momentum that are $4\hbar k$ and $6\hbar k$ apart, respectively. Again, the overall trend is that the second excited band is getting pushed up by the band below it for lower depths and pushed down by the band above it for higher depths. For both $b = 1$ and $b = 2$, this results in a turning point for the average energy of the band. The turning point is near $U = 9E_r$ for $b = 1$ and near $U = 27E_r$ for $b = 2$. After the turning point, if the depth is further increased, the band is pinched so that it has a narrower bandwidth.

4.2.2 Magic depths

The exact value of the turning point of the average band energy quantifies the magic depth. A more mathematically concise definition of the magic depth is the depth $U_M^{(b)}$ that satisfies the following condition:

$$0 = \frac{d}{dU} \left\langle E^{(b)} \right\rangle \bigg|_{U=U_M^{(b)}} . \tag{4.2}$$

Since the first derivative vanishes at the magic depth, this means that the average energy of the band is first-order insensitive to changes in the lattice depth.

From the band pictures described in the last section, we can immediately point out a few things about the magic depth. Firstly, the ground band ($b = 0$) has no magic depth. This is because the ground band is only ever pushed down by the bands above; therefore, its average energy only decreases with increasing depth. Secondly, all excited bands ($b \geq 1$) have a unique magic depth which increases monotonically with band number. Thirdly, the Bloch band at the magic depth describes a dispersion which is neither a free particle nor a tight-binding lattice. The bands have too much curvature to be free particles, but are not flat enough to be in a tight-binding lattice.

In Fig. 4.2(a) we show the values of the average band energies for the first four bands calculated using Eq. (4.1) up to $U = 100E_r$ lattice depth. The turning points for the first three excited bands are also visible. The magic depths are calculated by numerically retrieving the maximum value of each of the bands. We show the magic depths in Fig. 4.2(c) up to $b = 25$. We also show the second-order correction to the average band energy in Fig. 4.2(e) because this would be the next-order correction due to lattice depth variations away from the magic depth. The correction drops about one order of magnitude from the first to the fifth excited band, and shows little change after the tenth excited band.

We also show how the bandgaps change as a function of depth in Fig. 4.2(b) for $\beta \leq 4$ where β is the higher of the two bands involved at an avoided crossing. Specifically, in Fig. 4.2(d) we show the bandgaps at the magic points for β up to 26. The symbol $||_M$ denotes evaluation at the magic depth. Intriguingly, when we constrain the band gaps to the magic Bloch bands, the band gaps become linear as a function of the band number $\beta - 1$, with a positive slope. This is not the case generically if we fix the depth and vary the band number which is seen in Fig. 4.2(b). However, at the limit of the harmonic approximation ($U \to \infty$), the linear dependence on β for the bandgaps is recovered (see Chapter 1), albeit with a negative slope.

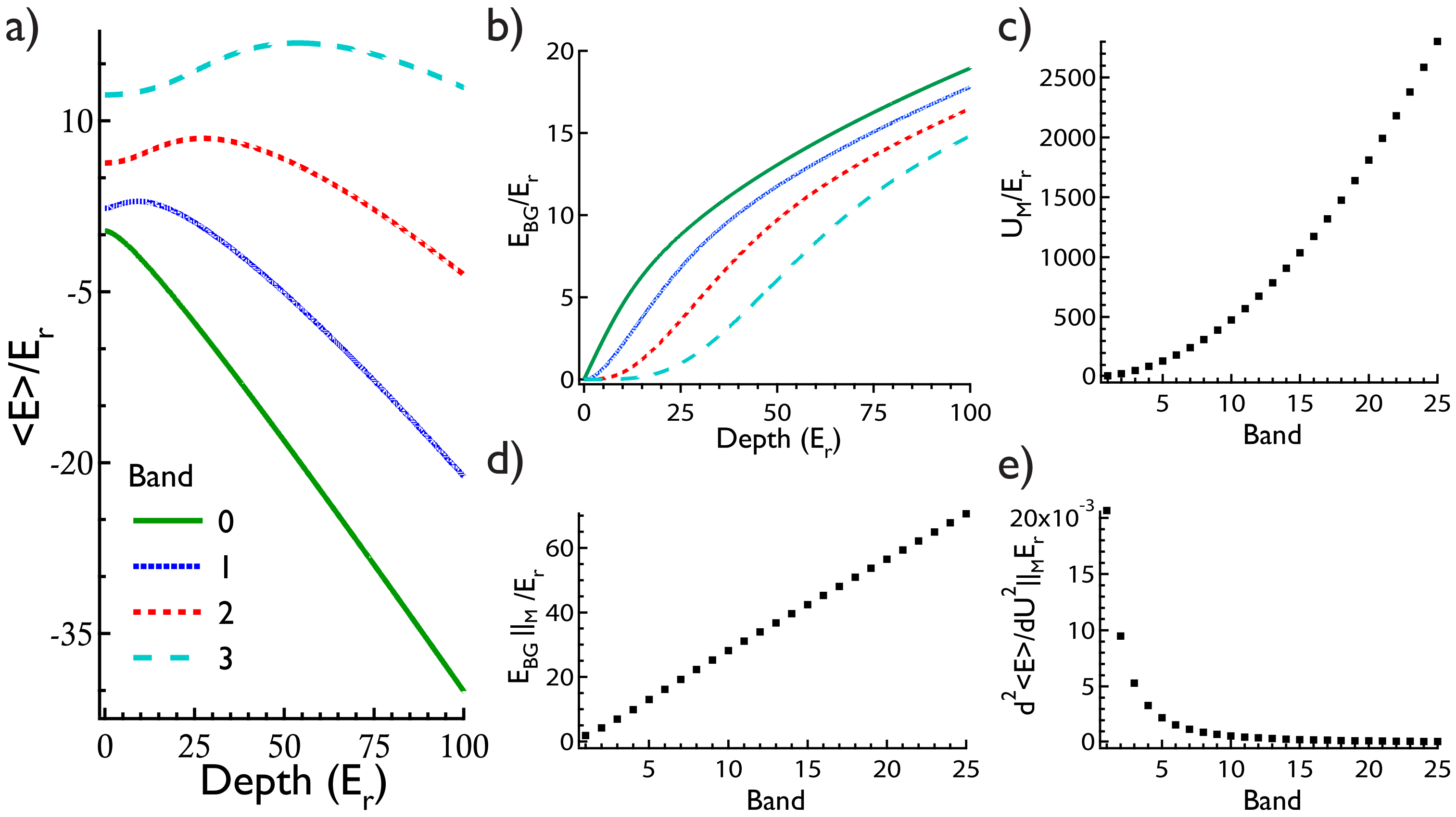

Figure 4.2: a) The average band energy from Eq. (4.1) up to $b = 3$ as a function of lattice depth with each excited band containing a turning point. (b) The bandgap between bands b and $b + 1$ for bands up to $b = 3$ as function of lattice depth. (c) The value of the magic depth for each band for the first twenty-five excited bands. (d) The bandgap as in (b) evaluated at the magic depth up to $b = 25$. (e) The second-order correction coefficient for the average energy as in (a) evaluated at the magic depths up to $b = 25$.

4.2.3 Intensity variation

Operating with magic Bloch bands offers protection against variation in the lattice depth. This may naturally arise due to intensity noise on the optical lattice lasers. Variations may also arise from atomic motion in the transverse direction of the optical lattice. We have discussed in Chapter 2 how atom-optics pulses for an atom interferometer are produced with an optical lattice. Lattice depth fluctuations in an optical lattice make Bloch oscillations unwieldy because they introduce phase noise on atom-optics pulses, diminishing the visibility of atom interferometer fringes.

A study of an atom interferometer operating with and without magic Bloch bands was pioneered in McAlpine et al. (Ref. [55]) with Bloch oscillations on one arm of a Mach-Zehnder interferometer. The visibility of the interferometric fringe was improved eightfold (see Fig. 4.3(b,c)) after applying a Bloch oscillation pulse in the first excited band near the magic depth $U_M^{(1)}$, when compared to application of Bloch oscillations in the ground band near the same depth.

In Figure 4.3(a) we show calculations of the average band energy up to $U = 12E_r$ so that we can visualize the effect of intensity shifts on the first two bands. Specifically, we consider a relative intensity variation of $\varepsilon = 0.1$ on the magic depth of the first excited band. The variation is depicted as the vertical gray shaded region. The corresponding variation in the average energy shift is shown as horizontal shaded regions. We can see that the variation of the average energy region on the ground band (red shaded region) is much wider than for the excited band (blue shaded region) for the 10% variation in lattice depth.

To quantify how much better the first excited band is, let's consider the phase instability $\delta\phi_{\text{lat}}$ resulting from lattice depth fluctuations of size εU_M after the lattice is on for a time T. We have dropped the superscript for the band number because choosing a magic depth also specifies the band. We can consider the contribution of a $\varepsilon \approx 1\%$ from our typical intensity noise on our lattice beams. The phase instability

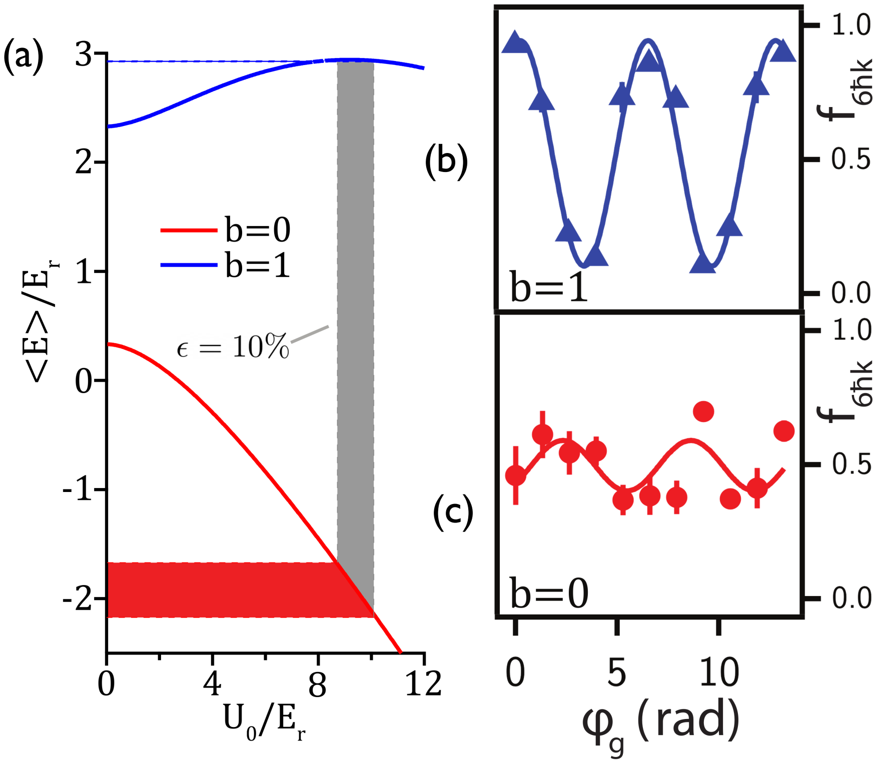

Figure 4.3: Visibility enhancement with magic Blochband (a) Average energy shown for ground and first excited band function of lattice depth. Vertical shaded region represents a 10% variation in lattice depth. The blue (red) shaded region is the average energy variation for $b = 1\,(0)$. (b,c) The visibility of Mach-Zehnder interferometer fringes utilizing $b = 1$ Bloch oscillation acceleration pulses near the $U_M^{(1)}$ magic depth—see McAlpine et al. 2020. (c) Same as (b) but utilizing ground band acceleration pulses.

is proportional to the variation of the average energy shown respectively in Eq. (4.3) and Eq. (4.4) for the excited band at a magic depth and the ground band for the same depth:

$$\delta\phi_{\text{lat}}^{(b>0)} = \left[\frac{1}{2}\left|\frac{d^2\langle E\rangle}{dU^2}\right|_{U_M} U_M^2\frac{T}{\hbar}\right]\varepsilon^2\,, \tag{4.3}$$

$$\delta\phi_{\text{lat}}^{(b=0)} = \left[\left|\frac{d\langle E\rangle}{dU}\right|_{U_M} U_M\frac{T}{\hbar}\right]\varepsilon\,, \tag{4.4}$$

$$\delta\phi_{\text{lat}}^{(b>0)}/\delta\phi_{\text{lat}}^{(b=0)} = \kappa(U_M)\varepsilon\,. \tag{4.5}$$

The improvement of instability in Eq. (4.5) by operating at a magic depth is proportional to the relative variation on the depth and on a prefactor which depends on the magic depth used. Because the slope of the average energy in the ground band varies slowly as a function of the lattice depth, the prefactor $\kappa(U_M)$, is mostly shaped by the product of (c) and (e) in Fig. 4.2. The result is that the prefactor does not vary much as a function of magic depth, and $0.28 \lesssim \kappa \lesssim 0.33$ for the first 25 excited bands. This means that if we expect $\varepsilon = 1\%$ lattice depth variation in the ground band, then we get nearly three orders of magnitude improvement of the phase instability by operating with excited bands. Reducing the instability by reducing ε even further provides and even greater enhancement in visibility from magic Bloch band operation.

4.3 Position-space View

4.3.1 Mathieu functions

A perfect optical lattice consisting of counterpropagating plane waves creates a pure cosine potential. For Gaussian beams, we have a cosine potential whose amplitude is modified by a gaussian envelope in the transverse direction. We will consider just the one-dimensional Schrodinger Eq. (4.6) with a cosine lattice of depth V_0 and lattice spacing d along the x-direction:

$$-\frac{\hbar^2}{2M}\frac{d^2}{dx^2}\psi(x)+\frac{V_0}{2}\cos\left(\frac{2\pi}{d}x\right)\psi(x)=E\psi(x)\,, \tag{4.6}$$

$$-\frac{1}{k^2}\frac{d^2}{dx^2}\psi+\frac{1}{2}\frac{V_0}{E_r}\cos\left(\frac{2\pi}{d}x\right)\psi=\frac{E}{E_r}\psi\,, \tag{4.7}$$

$$\frac{d^2}{d\alpha^2}\psi(\alpha)+\left[\epsilon-\frac{s}{2}\cos(2\alpha)\right]\psi(\alpha)=0\,. \tag{4.8}$$

After rescaling the eigenenergy and lattice depth by the recoil energy $E_r = \hbar^2 k^2/(2M)$ and making the substition $\alpha = kx$ we arrive at Eq. (4.8) which is the Mathieu equation[3].

The Mathieu equation has been extensively studied for a wide range of physical phenomena involving various numerical methods [85, 86], including quantum particles in an optical lattice [87, 88]. The solutions of the Mathieu equation have the form

$$\psi(\alpha)=e^{i\nu\alpha}u(\alpha)\,, \tag{4.9}$$

where $\nu(\epsilon, s)$ is called the characteristic exponent and $u(\alpha) = u(\alpha + \pi)$. Equation (4.9) describes Bloch waves if ν is real-valued. Of particular interest are the special Mathieu functions in which ν is an integer. For even integers, the special Mathieu functions have π period, and for odd integers, the special Mathieu functions have π anti-period.

4.3.2 Mathieu charactersitics

The pairs of values of the eigenenergies and lattice depths, $\epsilon(s)$ for which $\nu(\epsilon, s) = n$ where n is an integer, are called the characteristic values of the special Mathieu functions. These solutions are called the cosine-elliptic ($\mathrm{ce_n}(\alpha)$) and sine-elliptic ($\mathrm{se_n}(\alpha)$) functions. As illustrated in Fig. 4.4(b), we plot the Mathieu Characteristic for $s = 25$,

---

[3] The standard notation [83, 84] from Abramowitz and Stegun for the characterstic values, a and q in the Mathieu equation can be related to the rescaled band energies and lattice depth by $a = \epsilon$ and $q = s/4$.

which is equivalent to the Bloch bands of the extended Brillouin zone scheme. The special Mathieu functions for $\nu \in \mathbb{Z}$ exist at the middles and edges of the Brillouin zone where $\mathrm{ce_n}$ is the Bloch wave for the band $b = n$ at the lowest energy of the band and $\mathrm{se_n}$ is the Bloch wave for the band $b = n - 1$ for the highest energy of the band.

The characteristic values $\epsilon(s)$ for the cosine-elliptic and sine-elliptic Mathieu functions are shown in Fig. 4.4(a) in solid and dashed lines, respectively. The height of the filled shaded region between the characteristic curves shows the bandwidth of the energy bands as a function of lattice depth. From this figure, we can see that the bandwidths are largest when $s = 0$, describing free-space dispersion. On the opposite extreme, all of the bands eventually become flat as the depth increases to the harmonic oscillator limit ($s \to \infty$).

Using an extension of the characteristic curves, where we take ν to be a real number, we can also extract the magic depths! In Fig. 4.4(a), we see that the shaded regions have a turnaround point for all bands except for the ground band ($b = 0$). The turnaround point increases with increasing $\nu \in \mathbb{Z}$. We numerically integrate the characteristic curves for each value of the lattice depth. The maximum values of the integrated characteristic curves are marked by black dots and are exactly the magic depths [4]. The magic depths appear to be in a region between Bloch waves that are free and Bloch waves that are tightly bound.

To understand this further, in Fig. 4.4(c) we superimpose the characteristic values on a magic depth lattice for the first excited band. We can see that the characteristic values of $b = 1$ are just barely bound in the potential. Figure 4.4 (d) is similar but for the $b = 2$ magic depth. Once again, we see that the characteristic values for the second

---

[4] The characteristic curves in the lattice energy-depth parameter space share a resemblance with the stability diagrams of parametrically driven resonators in the drive frequency-amplitude parameter space. There, the onset of a resonance is driven by an instability from the resonator at rest [89]. The unstable regions are similar to the unshaded region captured by Fig. 4.4(a). Bloch waves are analogous to the shaded regions, i.e., stable solutions, where the oscillatory motion is bounded with non-zero amplitude. Magic depths are analogous to driving oscillations in a zero-dispersion regime [90], which makes the frequency stability robust to drive noise.

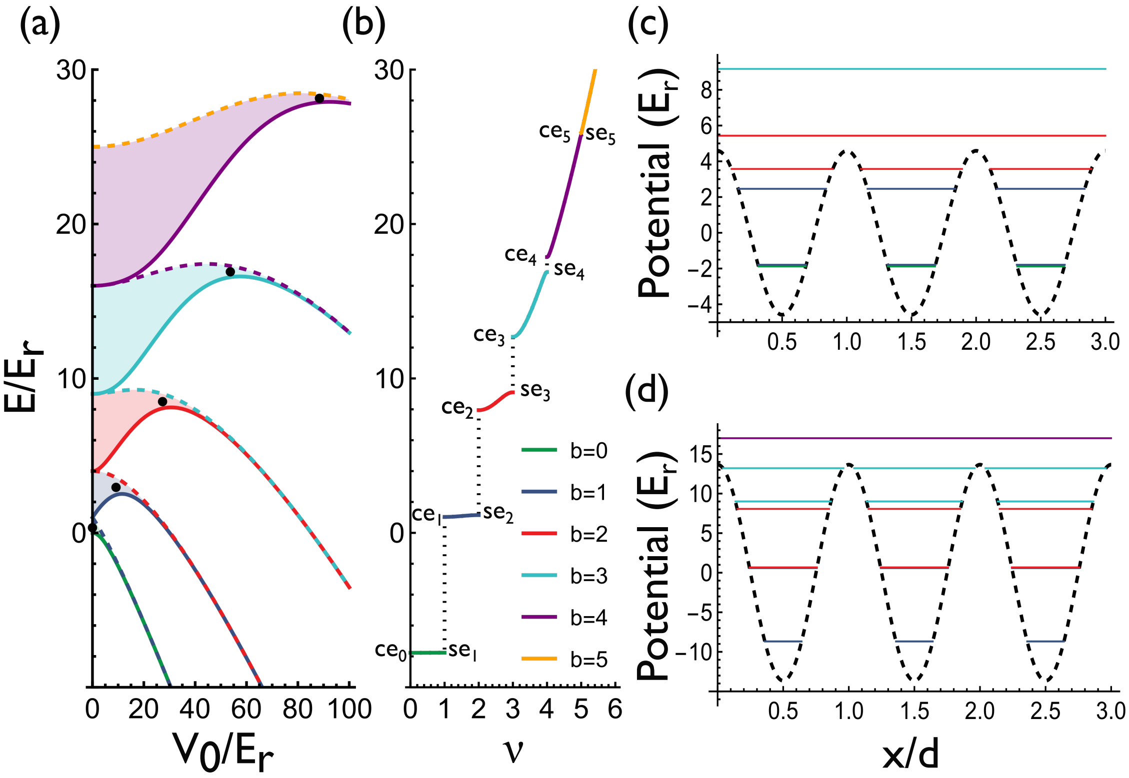

Figure 4.4: Mathieu charactersitics. (a) The characteristic curves $\epsilon_n(s)$ of the special Mathieu functions. Solid (dashed) curves are for the $\mathrm{ce_n}$ ($\mathrm{se_n}$) functions. The black dots represent the turnaround points from integrating $\epsilon_n(s)$ with characteristic exponent from $\nu = n$ to $\nu = n + 1$ in each of the shaded regions. (b) The characteristic value ϵ for $s = 25$ and $0 \leq \nu \leq 6$ reveal the first 6 bands in the extended Brillouin zone scheme. Dotted lines represent band gaps. (c) The optical lattice potential energy as a function of the lattice spacing, where $x/d = \alpha/\pi$. The horizontal lines are the first few Mathieu characteristic values for $s = U_M^{(1)}/E_r$ up to $\mathrm{se_3}$ are drawn. (d) Same as (c) for $s = U_M^{(2)}/E_r$ up to characteristic values for $\mathrm{se_4}$.

excited band are just barely bound by the lattice. We also see that the highest bound band (HBB) is too high in energy to be approximated by a tight-binding potential since the HBB is not very flat. The Bloch bands shown in Fig. 4.4(b) is for a depth just below the second magic depth. It is clearly shown that while the ground band has become flat, the first excited band has a small amount of dispersion and is almost flat. The 2nd excited band has some dispersion, but less than that of a free-particle. The higher bands are nearly like free-particles.

4.4 Magic Depth Scaling

We turn back to Fig. 4.2(c,d) to better understand the scaling of magic depth values as a function of band number. Let's consider first deep lattices in the tight-binding limit, where the bandgaps are also linear with the band number. This behavior resembles the bound states of the infinite well. In that limit, the energy states are nondispersive ($dE/dq \approx 0$) and the eigenenergies grow quadratically $E_l = l^2 E_r$ where l is the principal quantum number. This means that the difference between them grows linearly with the principal quantum number, $E_{l+1} - E_l = (2l+1)E_r$.

On the other hand, when particles occupy the highest bound band, they are weakly bound, and energy states are still dispersive. For a particle in band b to be in the HBB, the depth would have to be $U_M \gtrsim (b+1)^2 E_r$. The depth would have to change by $\Delta U||_M \gtrsim (2b+3)E_r$ to accommodate the $b+1$ band. For dispersive energy states, such as for the HBB, we can approximate the band gap as $E_{\text{BG}} \sim \Delta U/2$ for the highest bound band. This comes from a nearly degenerate two-level system perturbed by a ΔU potential depth. That means that the bandgap $E_{\text{BG}}||_M/E_r \gtrsim (2b+3)/2$ which gives a linear bound to the band number. Interestingly, this scaling gives a finite depth for which the ground band ($b=0$) is the HBB. We can write this as $\Delta U_M^{(b=0)} \sim E_{\text{BG}} \gtrsim 1.5E_r$ where we are abusing notation from the association between the depth for the HBB and the magic depth. However, the characteristic curve for the ground band shown in Fig. 4.4(a) indicates that this depth would not be robust against lattice depth variations, even though it is barely bound. This is because the ΔU for ground band is with reference to a plane wave energy at the limit of zero momentum, i.e., a zero-energy state with no dispersion. A true magic Bloch band requires some amount of dispersion from an energy states below and above it.

Chapter 5

EXCITED BAND TRAPPED ATOM INTERFEROMETRY

5.1 Constraining Atom Interferometry

High aspirations for accurate measurements of fundamental constants and highly precise sensing have driven the need for long-baseline atom interferometers, which are unconstrained in size, weight, and power (SWaP). For inertial sensing using a Mach-Zehnder (MZ) configuration, as in Fig. 5.1(a), the propagation phase scales as $\phi_{\text{prop}} \propto aT^2$, where atoms experience an acceleration a for a time $2T$, where T is the free propagation time between atom-optics pulses.[1] Furthermore, the phase sensitivity scales as

$$\frac{\delta\phi\sqrt{\tau_{\text{cycle}}}}{\phi_{\text{prop}}(T)}\,, \tag{5.1}$$

where $\delta\phi$ and $\phi_{\text{prop}}(T)$ are, respectively, the phase precision and propagation phase in one shot, and $\tau_{\text{cycle}} > 2T$ is the cycle time for a shot. Large propagation phase in small cycle times means that the measurement can be repeated more frequently, which allows for better sensitivity. The quadratic dependence on the propagation phase to T enables precision sensing with large bandwidths (small τ_{cycle}), making the MZ design very appealing since the measurement bandwidth is inversely proportional to the interferometer cycle time.

However, the physical dimensions of the interferometer also scale quadratically with the interferometer time and linearly with acceleration[2], making the Mach-Zehnder

---

[1] One additional mirror pulse may be implemented in a symmetric ($\pi/2$–π–π–$\pi/2$) pulse scheme for an interferometer. This mitigates the Doppler sensitivity of the atom-optics pulses [91, 92]. These can be due to fluctuations in the atomic velocity for different interferometer sequences or the finite momentum variance of matterwaves in each interferometer sequence.

[2] This simple scaling assumes that we do not use large momentum transfer techniques to improve

design unappealing on SWaP consideration grounds. (Consider the size, weight, and electrical power required to stabilize and maintain large stainless steel ultra-high vacuum systems. Not to mention the large amounts of laser power needed for a given laser intensity in beams with large Rayleigh ranges). For gravimetric local sensing, i.e., $a = g$, a back-of-the-envelope calculation yields that achieving a one-second free propagation time requires $\sim 2.5\,\mathrm{m}$ system sizes. (For interferometers placed in settings that may experience larger accelerations, this scaling is even worse for a fixed interferometer time). The straightforward approach to increasing the interferometer area results in system sizes that are unfeasible for laboratory-scale experiments.

Cutting-edge experimental designs for gravimetric precision measurements with atom interferometers involve large towers [93, 94] and/or networks of atom interferometers [95, 96, 97] for long-baseline measurements. Experiments on this scale must reckon with the technical challenges, overhead costs, and organizational complexities present in large user facilities and scientific collaborations. Further enhancing the performance of these user facilities would involve correlated measurements by kilometer-sized detectors for terrestrial-scale sensing [98]. These approaches for scaling up the interferometer size and number of detectors are clearly not compatible with the low SWaP requirements for local sensing in a fieldable apparatus [99].

5.2 Atom Interferometry with Trapping Fields

An alternative approach to scaling up precision sensing using atom interferometers employs some method of trapping matterwaves in space. These approaches start with the assumption that the system size must be limited. The space-time area enclosed by the interferometer is increased by suspending atoms in a trapping potential. With these approaches, measurement precision is traded off for measurement bandwidth, i.e., increased precision comes with longer experimental time scales. Trapped inter-

---

the scaling of the propagation phase with interferometer time.

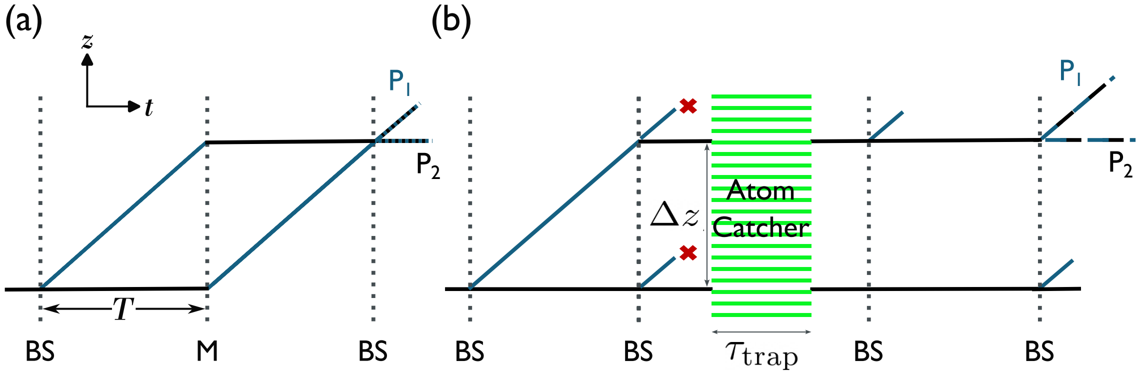

Figure 5.1: Space-time diagrams for field sensing with two interferometer output ports, P_1 and P_2, sketched in the co-moving frame of the atoms which aren't diffracted by beamsplitters. (a) Free space atom interferometer scheme that consists of only beamsplitters (BS) and a mirror (M) in a MZ configuration. The amplitudes of all four paths contribute to the interference of the fractional populations in the two output ports. (b) A trapped atom interferometer consisting of beamsplitters in a Ramsey-Bordé-like configuration augmented by an atom catcher which traps the matter wave with a superposition of wavepackets separated by a distance Δz for a duration τ_{trap}. There are eight possible paths—seven are explicitly shown—and the amplitudes of four paths contribute to interference effects of the two output ports.

ferometry is not a magic bullet; in a sense, this approach shifts the burden of an unconstrained experiment size to an unconstrained experiment duration. This is suitable for applications where high-precision measurements do not need to be repeated quickly. In addition, trapping fields introduce systematics and sources of noise that must be contended with and carefully investigated. Unlike free fall atom interferometers, where atom-optics are pulsed and have small contributions to the total phase, the propagation phase for trapped interferometers is significantly affected by the dynamics of matterwaves in continuously held traps.

Atoms susceptible to magnetic fields may be guided by stationary trapping fields for inertial sensing [100]. Developments with atom chip designs have led to configurable small-scale atom interferometers with unique trapping geometries [101, 102]. Furthermore, atom chips are capable of producing Bose-Einstein Condensates (BECs) in fast timescales [103]. The narrow momentum width of BECs allows for more efficient atom-optics pulses and better resolution of atomic populations between different interferometer output ports.

Trapping atoms in ground states, which are magnetically *insensitive*, requires an entirely different approach. Ytterbium is one such atom and can be cooled to quantum degeneracy in few-second timescales or quicker [42]. Atoms may be trapped within an optical dipole trap, split apart into spatially separated traps, and then recombined so that interferometer phase depends on the difference between the depths of the two traps. This early observation in Shin et al. [104] demonstrates the basic idea of a light-trapped interferometer, but the phase is dominated by differences in the light intensity, which would spoil sensitivity to gravitational effects. Instead, we build on an approach to trapped atom interferometry that utilizes optical lattices [22, 105, 106]. The interferometer geometry is similar to a Ramsey-Bordé interferometer, except that the interferometer paths are interrupted by a trapping potential which catches the matterwaves (see Fig. 5.1(b)). In this case, the "atom catcher" is a vertical standing wave formed by a 1D optical lattice. This type of interferometer scheme links the phase sensitivity of the beamsplitter pulses with the endurance of Bloch oscillations [107], leading to an increased sensitivity to gravity. This approach is suitable for all atoms, regardless of whether or not they are magnetic. This makes lattice-trapped atom interferometry ideal for ultracold ytterbium atoms, because the bosonic isotopes are very magnetically insensitive, while the fermionic isotopes have a finite *nuclear* magnetic dipole moment (see Chapter 2 for elaboration).

5.3 Magic Lattice-trapped Atom Interferometer

Lattice-trapped atom interferometers (LTAIs) utilizing the scheme shown in Fig. 5.1(b) have demonstrated unprecedented minute-scale coherence times [24]. Extrapolating the simple Mach-Zehnder scheme to one minute of coherence requires an interferometer tower that would extend into the stratosphere. Although the quadratic scaling of the propagation phase for an MZ interferometer implies that a much shorter interferometer time is required for the same phase accumulation, extending atom interferometry to longer coherence timescales could realize experimental probes of low-energy quantum gravity effects [108, 109]. The LTAI scheme is also robust to typical noise sources in ambient conditions, such as vibrations or magnetic fields [110, 111]. In the latter case, co-magnetometers are used to account for magnetic field gradients. Effects due to environmental magnetic fields may also be neglected by using atoms in magnetically insensitive states.

A major hurdle of trapped-atom interferometry, using either magnetic or laser fields, is the ability of trapping fields to disturb the sensitivity to the quantity of interest. Fluctuations in the trapping fields themselves could introduce instabilities on the trap propagation phase of atomic wavepackets [112]. In fact, state-of-the-art coherence times for LTAI are limited by the transverse motion of thermal atoms, causing stochastic sampling of the lattice depth for different atomic wavepackets [24]. Another possible cause for decoherence is the variation in the lattice depth. Therefore, an exploration of the lattice-induced phase noise and systematics is also required.

There are several ways to introduce lattice depth variation, which can cause dephasing during Bloch oscillations, e.g., fluctuations in the beam mode, beam power, beam pointing, or beam frequency.

5.3.1 Bloch-band control for lattice-trapped interferometry

Only differential variations between trapped wavepackets due to inhomogeneity of the beam in the lattice axis would cause dephasing. This necessitates the application of Bloch-band engineering by controlling the degrees of freedom of the lattice to further enhance the stability of such interferometers. Previously, our group applied Bloch band engineering to operate atom-optics pulses at magic depths in a free fall MZ interferometer [55]. (See Chapter 4 for more details about magic depths). There, we saw an enhancement in the visibility of interferometric fringes by operating Bloch oscillation pulses for large momentum transfer at the magic depth of an excited Bloch band. The key innovation for magic lattice-trapped atom interferometry (MLTAI) is to operate the trapping lattice in excited bands. For this work, we have limited our investigation to LTAI with $b = 0$ and $b = 1$ only.

We present the experimental scheme for MLTAI in Fig. 5.2, which illustrates the interferometer space-time diagram. First, we produce a BEC made of $\sim 5 \times 10^4$ atoms and a kinetic temperature of $< 30\,\mathrm{nK}$ in the $\hat{z}$-axis, which we let expand for a time t_{exp}, before any atom-optics pulses, so that interactions are negligible. We then apply a 2^{nd}-order Bragg π-pulse about $150\,\mu\mathrm{s}$ wide, the same width as the subsequent Bragg pulses, to clean up the momentum distribution of the BEC. The clean-up pulse ensures that the atoms have the same momentum width on each shot of an interferometer sequence. The subsequent beamsplitter pulse profiles ($\pi/2$-pulses) for the MLTAI are identical in duration but lower in pulse height. The identical width maintains the velocity selectivity of the Bragg pulse.

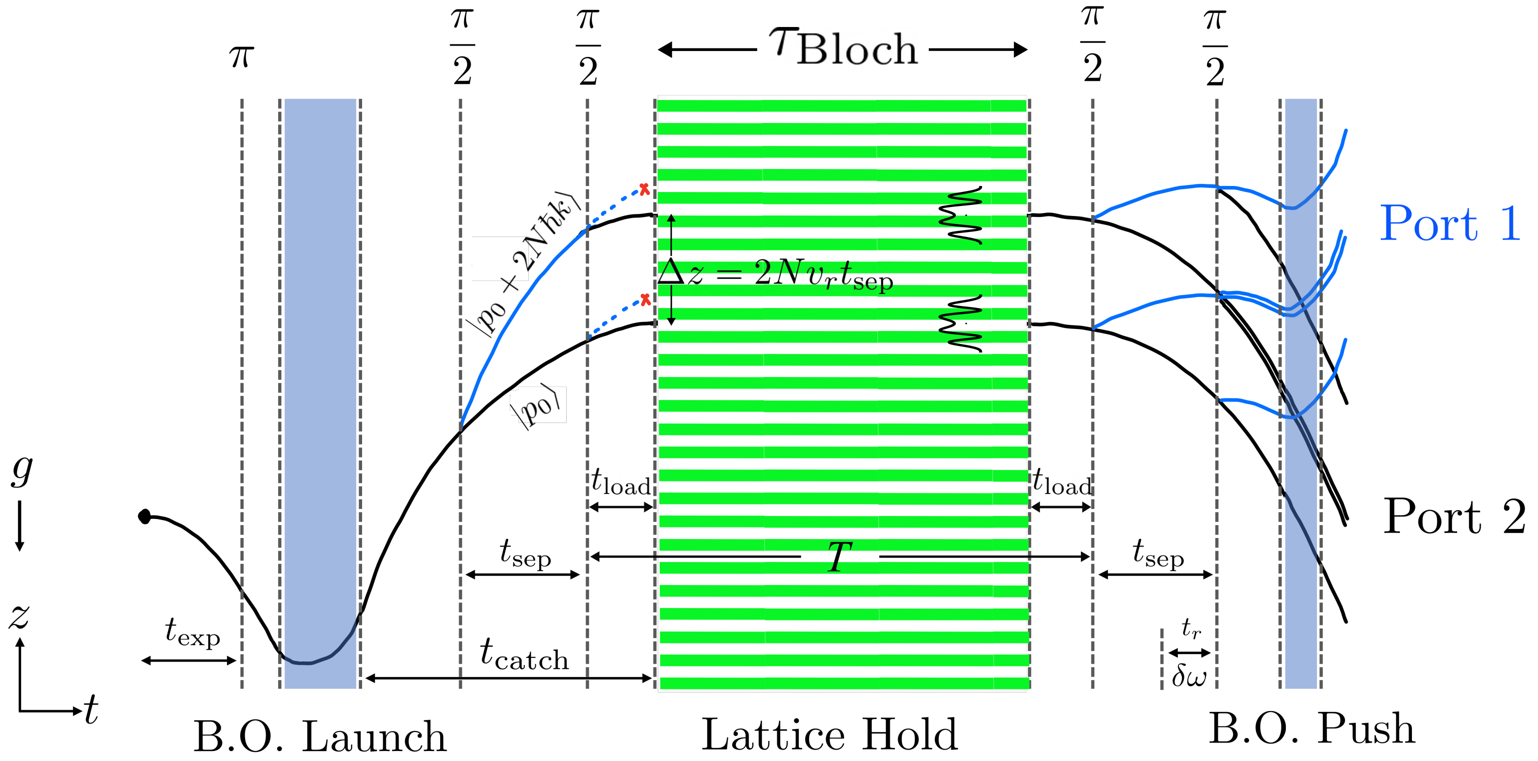

Figure 5.2: Spacetime diagram for magic lattice-trapped interferometry (not to scale). The solid black (blue) line sketches the classical trajectory of the $|p_0\rangle$ ($|p_0 + 2N\hbar k\rangle$) path. The π-pulse and $\pi/2$-pulses are $N = 2$-order Bragg diffraction pulses. The π-pulse is used to clean up the velocity distribution and is typically $\sim 50\%$ efficient. The BO launch is used to launch the atoms upward using ground band BOs in an accelerated lattice. The lattice hold is used to trap the wavepackets—shown as magic Bloch band state ($b = 1$, $q = 0.5\hbar k$) probability density—near the apex for a duration of τ_{Bloch} separated by Δz. The four $\pi/2$-pulses make a Ramsey-Bordé sequence extended by $T = \tau_{\text{Bloch}} + 2t_{\text{load}}$. The BO push spatially separates the interferometer ports by using ground band BOs to accelerate the atoms in Port 1 only—see Piccon et al. 2022.

Just before the interferometer starts, we launch the atoms against gravity using a ground band Bloch oscillation (BO) pulse with an upward-accelerating lattice, which is crucial for this interferometer scheme. We find a $t_{\text{ramp}} = 400\,\mu\text{s}$ intensity ramp time sufficient for adiabatically loading and unloading into and out of the optical lattice for all BO pulses used. As the BEC approaches the apex of its classical trajectory, we apply our opening interferometer pulse with a second-order Bragg $\pi/2$ pulse. After a time t_{sep}, a subsequent $\pi/2$ pulse is applied. After a time t_{load} following the second $\pi/2$-pulse, the atoms are caught in the trap. The order of the Bragg pulse N, and the duration t_{sep} determine the spatial separation $\Delta z = 2Nv_r t_{\text{sep}}$, of the atomic wavepackets. Here, $v_r = 4.1\,\text{mm/s}$ is the recoil velocity. After a time t_{catch} from the BO launch, the standing wave is turned on. The timing relative to the apex determines the band and quasimomentum into which the BEC is loaded (see Eq. (2.14) in Chapter 2 for more detail). We choose to trap the pair of states with lower momentum p_0 (black lines in Fig. 5.2), because catching that pair makes the free propagation time in the interferometer shorter[3]. The matterwaves are held in the lattice for a duration τ_{Bloch} where the atoms experience gravity-induced BOs. The typical lattice depth for the trap is near the magic depth of the first excited band.

After the atoms are released from the trap they see two more symmetrically timed $\pi/2$-pulses. Between these two pulses, the angular frequency of one of the lattice beams can be given a fixed offset of $\delta\omega$ for a laser phase ramp time of t_r before snapping back to the correct frequency for the last $\pi/2$-pulse where the interferometer closes. Then a Bloch separator pulse [113], which we label the BO push beam, is used to spatially separate the output ports of the interferometer. We accelerate the atoms in Port 1 ($|p_0 + 2N\hbar k\rangle$) with ground band BOs. The Port 2 ($|p_0\rangle$) atoms Landau-Zener tunnel and are effectively in free fall during the BO push. Finally, the populations of

---

[3] It is generally beneficial to reduce the time between beamsplitter pulses because otherwise the phase variation of beamsplitters grows, due to vibrations on optical lattice mirrors. The wavepackets with larger momentum $p_0 + 2N\hbar k$, are loaded into a higher band that is not bound, which means that they are effectively in free fall and Landau-Zener tunnel to higher bands

the two output ports are counted via absorption imaging after time of flight.

In practice, the atom-optics pulse timings are all calculated relative to the apex time, which depends only on the BO launch. Choosing the band and initial quasimomentum of the atoms in the trap involves shifting the entire interferometer relative to the apex time. We vary t_{sep} by changing the time for the first (last) beam splitter pulse before (after) the apex. This constrains $t_{\text{sep}} < t_{\text{catch}}$, which limits the matter-wave separation as well. In principle, t_{catch} can be extended by applying a larger BO launch force.

5.3.2 Trapping in excited or ground bands

The narrow momentum width of our BEC source allows for adiabatically loading the atoms into any band. For this demo work, we choose to load in either the first excited or ground band. We detune the optical lattice light so that it is $\Delta/\Gamma = -8.8 \times 10^4$, which is approximately 16 GHz red detuned from the narrow linewidth ${}^1S_0 \rightarrow {}^3P_1$ intercombination transition. We measure the one-body loss rate for the atoms trapped in either the ground or the excited band at the $b = 1$ magic depth. For the ground band, we observe a $1/e$ decay time of 384(17) ms, which is entirely consistent with the spontaneous scattering rate. For the loss of atoms in the excited band, we find that the decay time is smaller at 77(14) ms, which is nearly a factor of five faster. As described in Chapter 4, the magic Bloch band for a given band is the highest bound band of the cosine potential. Technical imperfections in the lattice beams may cause increased spilling in magic-trapped bands and this band may be more susceptible to loss from heating in the lattice. Further investigation on this is required.

We also observe Bloch oscillations in the momentum of the atom clouds in the ground or excited bands. The experimental sequence for this measurement is very similar to the one illustrated in Fig. 5.2 except without the $\pi/2$ pulses or the BO push beam. As in Fig. 5.3(a), the BEC is loaded into either the ground ($b = 0$) or excited band ($b = 1$) with $q_0 \approx 0.5\hbar k$ initial quasimomentum, respectively. We then

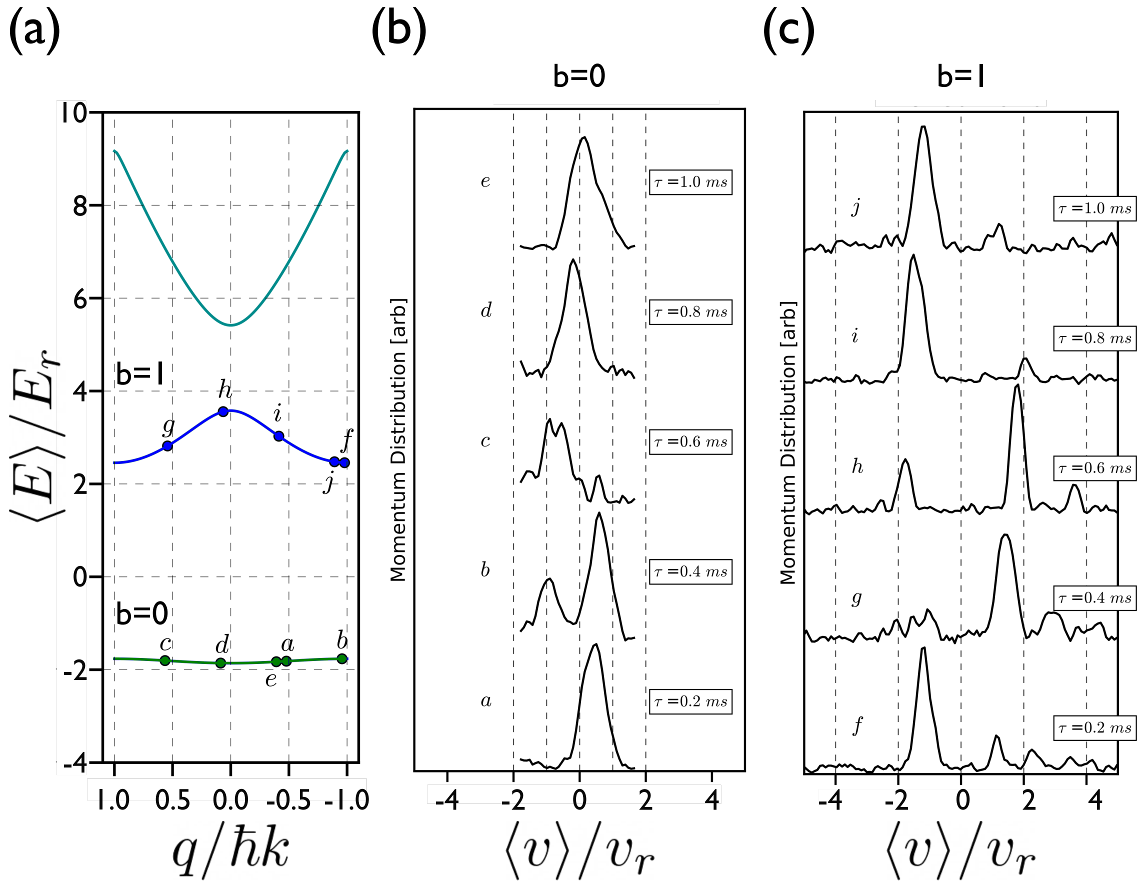

Figure 5.3: Gravity-induced Bloch oscillations in a trapped vertical lattice of depth $U \approx 10E_r$ where $T_{\mathrm{BO}} \approx 840\,\mu$s is the BO period. Negative momentum or velocity is in the direction of gravity. (a) Bloch bands showing the green (blue) $b = 0$ ($b = 1$) bands with labels approximating the linear sweep in quasimomentum. (b) TOF traces after adiabatically unloading from the lattice when the atoms are at the quasimomenta labeled in (a) for $b = 0$. We observe a Bragg event where the atoms have a $-2v_r$ jump (c) Same as (b) but for $b = 1$. Here we see two Bragg events, a feature of excited band BOs, where the atoms have a $+2v_r$ jump followed by a $-4v_r$ jump.

vary τ_{Bloch} between 0.2 ms and 1.0 ms, which encompasses nearly one Bloch oscillation period.

We use time of flight imaging to map the band states back to the free-particle states after adiabatically unloading from the trapping lattice. Integrated traces shown in Fig. 5.2(b,c) are of the BEC after time of flight for ground band and excited band trapping, respectively. Encapsulated in these traces is a distinguishing feature of ground band Bloch oscillations, which is that the atoms only see one avoided-crossing over the course of one Bloch oscillation. Atoms in all other bands would see two avoided crossings in a Bloch oscillation process. The avoided crossings in the middle correspond to the even Bragg diffraction orders, and the edge avoided crossings corresponds to odd order Bragg diffraction [114, 115, 20]. This means atoms in the ground band see a first-order Bragg diffraction event which connects v_r and $-v_r$ free-particle states. Here, $v_r = \hbar k/M$ is the recoil velocity and M is the mass of ytterbium (see Chapter 2). On the other hand, atoms in the first-excited band see a first-order Bragg event at the edge of the Brillouin zone followed by a second-order Bragg event at the middle of the Brillouin zone. These are jumps connecting $-\hbar k$ to $\hbar k$ followed by a jump connecting $2\hbar k$ to $-2\hbar k$ free particle states.

5.3.3 Interferometer visibility with ground vs excited band trapping

We compare interference fringes utilizing magic and non-magic Bloch band trapping in the vertical standing wave. In other words, we employ the interferometer described in the earlier section at a fixed lattice depth $U \approx U_M^{(\text{b}=1)}$ with the BEC loaded selectively into the ground band of this optical lattice or the first excited band. For the ground band we load the atoms at $q_0 = 0.5\hbar k$, and for excited band we load the atoms into $q_0 = -0.5\hbar k$ to ensure maximum separation from any Bragg scattering events at the avoided crossings during the initial load into the optical lattice. If we did not load the atoms exclusively into one band, we would expect multi-path Landau-Zener-Stückelberg-Majorana interference effects [47] which would contribute to the propagation phase.

For fixed separation Δz and lattice hold duration τ_{Bloch}, we extract interferometric fringes by varying the lattice grating phase ϕ_L of the last Bragg beam splitter pulse. A few example fringes are shown in Fig. 5.4 using the phase ramp time, $t_r = \phi_L/\delta\omega$, as our independent variable, where $\delta\omega = \{\pm 5\,\mathrm{kHz}\}$ or 0 if we choose not to ramp. We show fringes for the first-excited and the ground band near the magic depth for $b = 1$ in the left and right columns, respectively. The data for each fringe is taken by randomly varying t_r and $\delta\omega$, our independent variables. The different rows of Fig. 5.4 correspond to different settings for the wavepacket separation and the lattice trap duration.

The periodic variation of the asymmetry $\mathcal{A}$ can be decomposed into three contributions arising from the propagation phase, the laser phase, an imperfect splitting phase, and an offset phase with reference to a perfectly stable lattice position [116, 99]. From each fringe, we fit a sinusoidal function to the asymmetry

$$\mathcal{A} = \langle \mathcal{A} \rangle + C \cos\left(\Phi + \delta\phi\right), \tag{5.2}$$

defined as ($\mathcal{A} \equiv \rho_1 - \rho_2$), where ρ_j is the fractional population of the j^{th} output port. The additional term in the phase $\delta\phi$ represents a phase precision which may result from instabilities in Φ defined in Eq. 5.3 in the next section. The resulting phase instability would cause a reduction in the fitted amplitude of the interferometer fringe.

Only four of the eight possible paths interfere in the two output ports. This means that the maximal contrast we expect is $C = 0.5$ because only half the atoms contribute to the population coherently. For our fits, as seen in Fig. 5.4, the phase is parameterized as $\Phi = \phi_L + \phi_0$ and we keep the mean asymmetry $\langle A \rangle$, amplitude $C^{(b)}$ and offset phase ϕ_0 as free parameters. Other typical limiters of interferometer contrast include static beam imperfections [22] or background noise on our detectors.

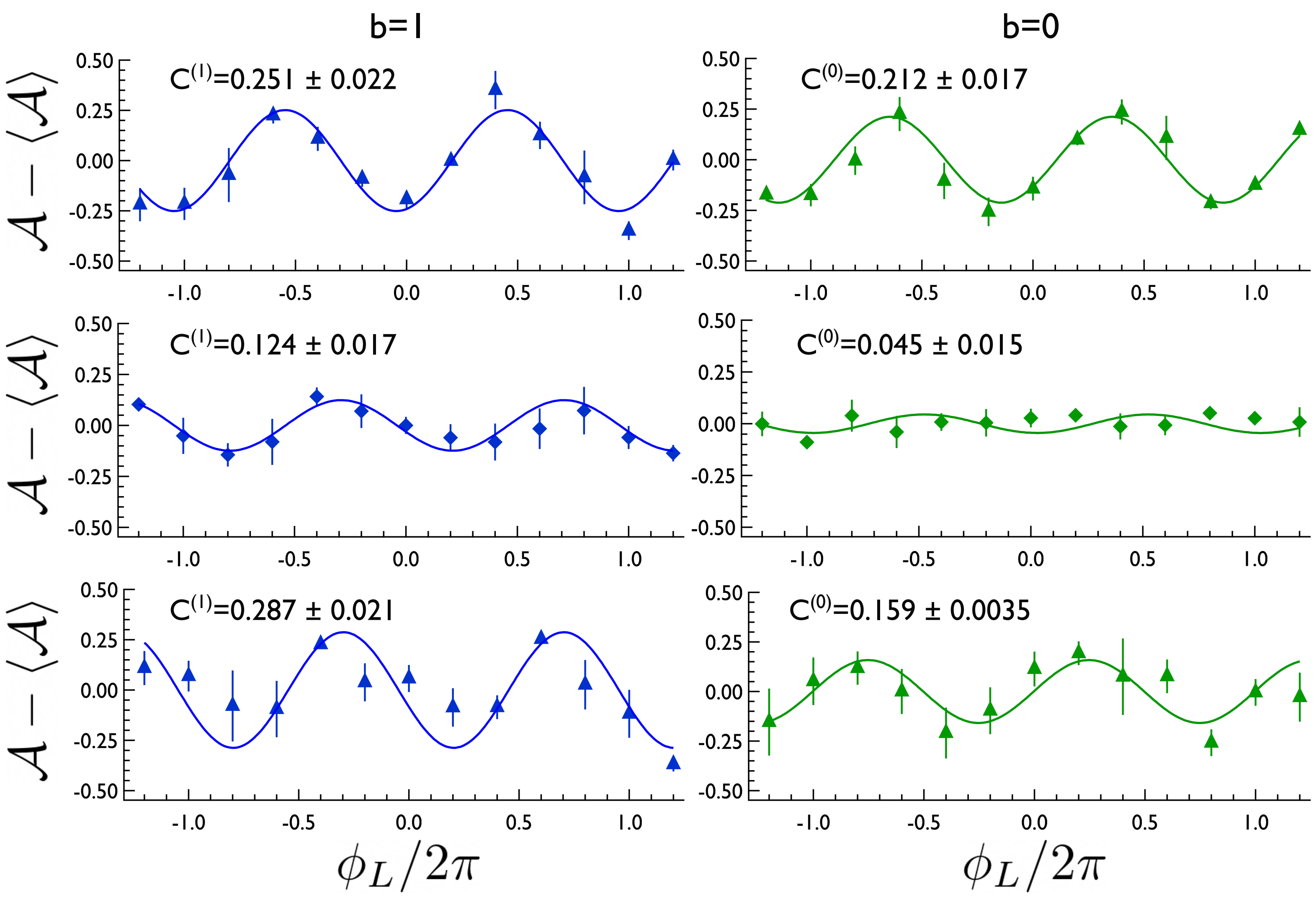

Figure 5.4: Preliminary: Trapped atom interference fringes obtained by varying the laser grating phase for atoms in excited (ground) band on the left (right) column. Top: Fringes for wavepackets loaded into a $U = 9.2E_r$ deep lattice where $(\Delta z/d, \tau_{\text{Bloch}}/T_{\text{BO}}) \approx (10, 5)$ Middle: Same as top but for a $U = 9.4E_r$ deep lattice where $(\Delta z/d, \tau_{\text{Bloch}}/T_{\text{BO}}) \approx (10, 186)$ Bottom: Same as middle, but $(\Delta z/d, \tau_{\text{Bloch}}/T_{\text{BO}}) \approx (80, 5)$.

5.3.4 Signal dephasing and instability

Neither the atoms nor the optical lattice are perfectly uniform in space or constant in time. Furthermore, for a thermal distribution of atoms in an optical lattice, atoms experience a distribution of trapped propagation phases due to the variation in the lattice depth experienced by the different atoms. The result is *dephasing* across the atomic ensemble. In Chapter 4 we considered the resulting *phase instability* due to variation in the lattice depth in either the ground or excited band. We saw that special Bloch bands, called magic Bloch bands, are insensitive to such variations up to first order. Phase instabilities reduce the *visibility* of an interferometric signal without reducing the contrast. Phase instabilities are only the result of variation in the lattice depth. If the ensemble of atoms sees the lattice identically, thereby each atom contributes the same phase, what that phase is may vary shot-to-shot because of lattice depth variation. On the other hand, dephasing occurs when an inhomogeneous/fluctuating ensemble of atoms meet an inhomogeneous/fluctuating lattice. Thereby, for each shot, the ensemble averaging over the distribution of phases results in a flattening of the contrast of the interferometer signal. In short, environmental variation on an atomic wavepacket results in phase instability, while environmental variation *combined with* atomic ensemble variation results in dephasing.

We also emphasize that the phase for this interferometer geometry (Fig. 5.2) is only susceptible to variation in the *differential* lattice depth between the separated wavepackets. This means that the lattice must have inhomogeneities and fluctuations in the vertical direction, e.g., through lattice tilt noise for a thermal ensemble of atoms [24], leading to decoherence of the interference signal. While we understand that magic depths protects against phase instabilities, we expect that they would also help with dephasing from lattice dynamics. This is simply because the phase variance between atoms in the thermal ensemble is also minimized at the magic depth. We may interpret the fitted amplitudes $C^{(b)}$, as the overall visibility of the fringe, where

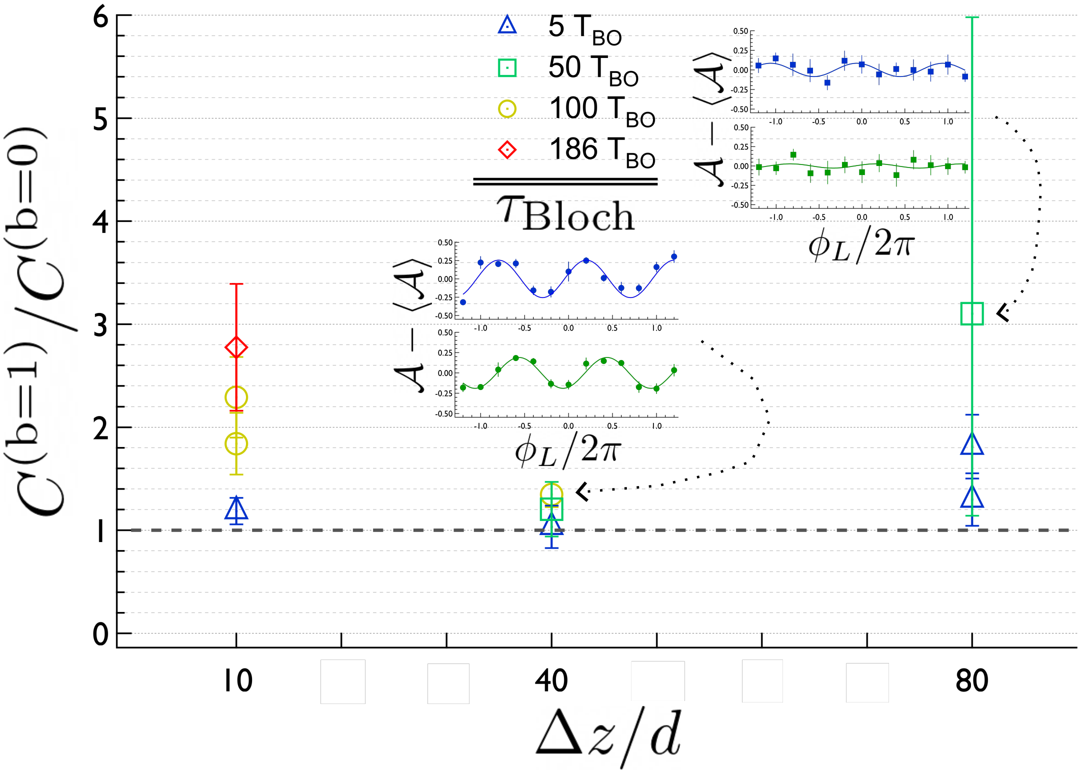

Figure 5.5: Preliminary: Relative performance of ground vs excited band trapping for a vertical lattice near the magic depth for the first excited band. The ratio $C^{(1)}/C^{(0)}$ of visibilities extracted from fringes as in Fig. 5.4 comparing ground and excited band LTAI. The horizontal dashed line represents when the fringes have the same visibility. Middle inset: Ground (excited) band fringe for $\Delta z/d = 40$ and $\tau_{\text{Bloch}}/T_{\text{BO}} = 100$ on the bottom (top). Right inset: Same as the middle inset but for $\Delta z/d = 80$ and $\tau_{\text{Bloch}}/T_{\text{BO}} = 50$. The large relative error from this point comes from the fact that the sinusoidal fit is poor for the ground band fringe due to the data being consistent with 0 visibility.

the fit captures the reduction from the maximum visibility ($C^{(b)} = 0.5$). Both phase instabilities and dephasing should cause the fitted amplitudes of interferometer fringes to drop from the maximum value which would impact the resulting phase precision $\delta\phi \sim 1/C^{(b)}$. Using various fringes as in Fig. 5.4, we compare the visibility of ground and excited band fringes near the $b = 1$ magic depth. Figure 5.5 shows the ratio of the fitted amplitudes for various combinations of wavepacket separations and lattice trap durations. The ratio $C^{(\mathrm{b=1})}/C^{(\mathrm{b=0})}$ quantifies the relative performance of magic vs nonmagic Bloch bands. The error bars are propagated from the statistical error on the fitted amplitudes. We observe that the MLTAI fringes are never worse than the ground band LTAI fringes. We find generally that there is a trend of improved performance for MLTAI compared to ground band interferometers with increasing lattice trap duration for all wavepacket separations explored. However, the enhancement in visibility may be due to operation in an excited band rather than operation in a magic Bloch band.

5.4 Gravimetry with a Lattice-trapped Interferometer

The total interferometer phase Φ, of a perfectly stable ($\delta\phi = 0$) lattice-trapped interferometer depends only on the propagation phase, the laser phase, the splitting phase, and an offset phase. This is explicitly as

$$\Phi = \phi_{\mathrm{laser}} + \phi_{\mathrm{prop}} + \phi_{\mathrm{split}} + \phi_0 \,, \tag{5.3}$$

$$\phi_{\mathrm{laser}} = \phi_L + \phi_{\mathrm{chirp}} \,, \tag{5.4}$$

$$\phi_{\mathrm{prop}} = \phi_{\mathrm{free}} + \phi_{\mathrm{trap}} + \phi_{\mathrm{diff}} \,, \tag{5.5}$$

where the laser phase and propagation phase has been further broken down. The propagation phase has contributions from the free fall and trapped evolution of the matterwaves, as well as a diffraction phase [20] from Bragg pulses. The laser phase has a contribution from the lattice grating phase ϕ_L and a phase ϕ_{chirp} arising from a frequency chirp to maintain the Doppler shift of the beam splitters in the co-moving frame of the atoms. For the rest of the discussion, we will assume that there is perfect overlap of the wavepackets ($\phi_{\text{split}} = 0$).

In the typical Mach-Zehnder configuration, gravimetric measurements are done by tuning the laser frequency chirp α, so that the laser phase perfectly cancels out the *free* propagation phase up to a fixed phase offset. The MZ interferometer phase is

$$\begin{aligned} \Phi_{\text{MZ}} - \phi_0 &= \phi_{\text{laser}} + \phi_{\text{free}} && (5.6) \\ &= (k_{\text{eff}} g - N\alpha) T^2 \,, && (5.7) \end{aligned}$$

where T is the free propagation time between the beam splitter and mirror as in Fig. 5.1(a) and N is the Bragg order of the pulses ($N = 1$ for two-photon Raman pulses). Varying α for fixed T gives an interferometer fringe whose offset is ϕ_0 when α exactly compensates for g. In that case, the time-varying portion of Eq. (5.7) is zero, so that multiple interference fringes can be measured for different T. The value of α for which $\Phi_{\text{MZ}} = \phi_0$ gives the null phase. This means that if k_{eff} is known by precisely measuring the laser wavenumber and having knowledge of the Bragg order, then a precise value of g is revealed.

5.4.1 Ramsey-Bordé-Bloch modes

The technique for varying the frequency chirp α, was demonstrated by Charrier et al. and Zhang et al. for lattice-trapped interferometry as well [22, 105]. For the LTAI configuration, the propagation phase (5.5) has a contribution from the evolution of the matter wave in the trap

$$\begin{aligned} \phi_{\text{trap}} &= 2\pi \times (\nu_{\text{B}} \tau_{\text{Bloch}}) \, (\Delta z / d) && (5.8) \\ &= k_{\text{eff}} g t_{\text{sep}} \tau_{\text{Bloch}} \,. && (5.9) \end{aligned}$$

In fact, we would like to operate the LTAI so that the dominant contribution to the propagation phase is from the trap phase (5.9) to extend the total interferometer time. The technique used in Charriere et al. and Zhang et al. implements a non-zero laser phase for the beamsplitter pulses during the trapped evolution. To compensate for the Doppler shift from the fact that the atoms were not in free fall, an additional frequency jump is applied. The resulting phase is

$$\begin{aligned}\Phi_{\mathrm{RBB}} - \phi_0 &= \phi_{\mathrm{laser}} + \phi_{\mathrm{free}} + \phi_{\mathrm{trap}} && (5.10)\\ &= \underbrace{(k_{\mathrm{eff}} g - N\alpha)\left(t_{\mathrm{sep}}^2 + t_{\mathrm{sep}} T\right)}_{\text{freely falling frame}} - \underbrace{(k_{\mathrm{eff}} g \tau_{\mathrm{Bloch}} + \delta\omega) t_{\mathrm{sep}}}_{\text{BO compensation}}\,, && (5.11)\end{aligned}$$

where $T \approx \tau_{\mathrm{Bloch}}$ as in Fig. 5.2. The constant frequency chirp treats the interferometer as if the atoms are in free fall to give the first term. The Bloch oscillation term results from the fact that the atoms are trapped for $\tau_{\mathrm{Bloch}} \approx N_B \nu_B^{-1}$ duration. It includes the frequency jump $\delta\omega \approx -k_{\mathrm{eff}} g \tau_{\mathrm{Bloch}}$, so that a lattice grating phase $\phi_L = \delta\omega t_{\mathrm{sep}}$ causes this term to vanish. Fringes are measured by varying the frequency chirp, while holding T and t_{sep} fixed. After repeating the measurement for different values of T, we get a linear dependence on the fringe frequency. Then α is perfectly tuned to gravity when the slope of the frequency as a function of T is zero. If the Bloch oscillation term is not perfectly canceled, then there is another contribution to this slope, which means that the accuracy of the interferometer may be limited by how well the Bloch oscillation frequency is known. We call this the Ramsey-Bordé mode of the lattice-trapped interferometer, which is sensitive to acceleration due to gravity.

We use another approach, which was demonstrated by Xu et al. [106]. To account for the potentially long propagation time in the trap ($\tau_{\mathrm{Bloch}} \gg t_{\mathrm{catch}}$), we jump the chirp between $\alpha \sim 2kg$ for the free fall portion of the interferometer and $\alpha = 0$ for the trapped portion of the interferometer, where the lattice is stationary. Here, $2kg \approx 35.28\,\mathrm{kHz/ms}$ for ytterbium in our lattice. This means there is no laser phase during the trapped portion of the interferometer. Then the total phase is similar to that of a Ramsey-Bordé interferometer phase:

$$\begin{aligned}\Phi_{\mathrm{RBB}} - \phi_0 &= \phi_{\mathrm{laser}} + \phi_{\mathrm{free}} + \phi_{\mathrm{trap}} && (5.12)\\ &= \underbrace{\left(k_{\mathrm{eff}}g - N\alpha\right)\left(t_{\mathrm{sep}}^2 + 2t_{\mathrm{sep}}t_{\mathrm{load}}\right)}_{\text{free fall}} - \underbrace{k_{\mathrm{eff}}gt_{\mathrm{sep}}\tau_{\mathrm{Bloch}}}_{\text{Bloch oscillations}}\,, && (5.13)\end{aligned}$$

where $T = \tau_{\mathrm{Bloch}} + 2t_{\mathrm{load}} \approx \tau_{\mathrm{Bloch}}$ extends the interferometer time because of the trap.The first term is similar to the traditional Ramsey-Bordé interferometer phase with a time $2t_{\mathrm{load}}$ between the second and third beam splitters. The second term is the trap propagation phase (5.9), due to Bloch oscillations. The trap duration $\tau_{\mathrm{Bloch}} = N_B\nu_B^{-1} + \delta\tau$, consists of N_B Bloch oscillation periods and an additional time $\delta\tau \equiv \tau_{\mathrm{Bloch}} \bmod \nu_B^{-1}$. Crucially, the total phase (5.13) has contributions from the free fall evolution and the trapped evolution as expected.

From the phase (5.13), we can measure a fringe by varying τ_{Bloch} and holding α and t_{sep} fixed. The first free fall term would just be an offset. Ideally, α can be set so that the first term vanishes. From this variation we get a fringe whose frequency scales with the Bloch oscillation frequency. Therefore, precise measurement of this frequency can be done by choosing several values of N_B and measuring a fringe by varying $\delta\tau$ around each value of N_B. Since there is also a linear dependence of the slope on t_{sep}, we can vary the spacing and see a linear dependence on the frequency. The accuracy of t_{sep} can be a limiting factor for the accuracy of the frequency, although this ambiguity can be resolved by operating a typical MZ interferometer without the trap ($\tau_{\mathrm{Bloch}} = t_{\mathrm{load}} = 0$) by varying α and measuring the quadratic dependence of the fringe frequency on t_{sep}. We call this method of fringe measurement the Bloch mode of the interferometer because we can precisely deduce the Bloch oscillation frequency.

The two measurement modes of this interferometer make it a Ramsey-Bordé-Bloch (RBB) interferometer. In the Ramsey-Bordé mode, the phase (5.11) is varied as a function of frequency chirp, and the Bloch oscillation term is canceled. In this mode, the RBB interferometer phase is sensitive to the *local acceleration due to gravity*, but the accuracy is limited by the determination of the Bloch oscillation frequency. On the other hand, in the Bloch mode, the phase (5.13) is sensitive to *local forces*, i.e., Bloch oscillations, but the accuracy may be limited by the determination of t_{sep}. Both modes of the interferometer may be used in tandem to measure the acceleration due to gravity and the inertial mass ($M \propto \nu_B$) separately.

5.5 Summary

We report on lattice-trapped atom interferometry with BECs in magic Bloch bands. We find an overall enhancement in the performance of the magic lattice-trapped atom interferometer when compared to the ground band trapped atom interferometer. We use the ratio of the magic and non-magic trapped interferometer visibilities at $U_M^{(b=1)}$ lattice depth as a proxy for the improvement in the interferometer performance. This ratio is a crude measure of the performance enhancement because the visibility of ground band fringes is poor for large τ_{Bloch} and Δz, which makes sinusoidal fits unreliable. Because of this, the error bars in Fig. 5.5 start to diverge for the largest values of τ_{Bloch} and Δz used in this work. We see that the spontaneous scattering rate of the trapping laser limits τ_{Bloch} and we believe Δz is limited by vibrational phase instabilities between beamsplitter pulses [117].

Further analysis is needed to better quantify the enhancement in visibility from employing lattice-trapped interferometry with magic Bloch bands. Some technical improvements on our experimental apparatus could increase the dynamic range for MLTAI. Firstly, we expect that the maximum contrast of the interferometer may improve with mode cleaning optics for the interferometer beams. The interferometer coherence time is limited by the spontaneous scattering rate of the diffraction beam laser. We expect improved coherence times by utilizing a separate, farther detuned laser source for the trapping lattice. We also expect that improved vibration isolation or phase-locked lattice beams [118] could lower the phase instability of the beamsplitter pulses for larger matter wave separation.

Chapter 6

OUTLOOK

Let's return to the question we asked in the very beginning—what can we do with quantum interference? We found that atomic matterwaves can be controlled via optical lattices, which serve as the matterwave atom-optics. We concern ourselves now with possible future directions for precision atom interferometry using Bloch oscillations (BOs) for inertial sensing. The phase sensitivity of both lattice-pulsed and lattice-trapped interferometers may benefit from utilizing Bloch oscillations, which have had limited use thus far. Bloch band engineering techniques, which place ultracold atoms in magic Bloch bands, may be a method to wield Bloch oscillations in *phase-stable* interferometers for lattice-pulsed and lattice-trapped interferometry.

For interferometers where the atomic wavepackets evolve largely through free-space, BOs are used as a large momentum transfer tool, increasing the sensitivity to accelerations by increasing the interferometer space-time area. On the other hand, for lattice-trapped interferometers, where the atomic wavepackets evolve largely in the trap, forces are measured precisely by measuring the Bloch oscillation rate. Although ground band BOs in optical lattices have higher fidelity than excited band BOs for a given lattice depth, magic depth BOs in excited bands are protected from lattice depth variation. We are particularly interested in applying atom interferometers towards precision sensing of gravity for advances in quantum sensing and fundamental physics.

6.1 Kilorecoil Interferometry

For lattice-pulsed interferometry, interferometers have yet to exceed the large momentum transfer threshold of one thousand photon recoils within a phase-stable interfer-

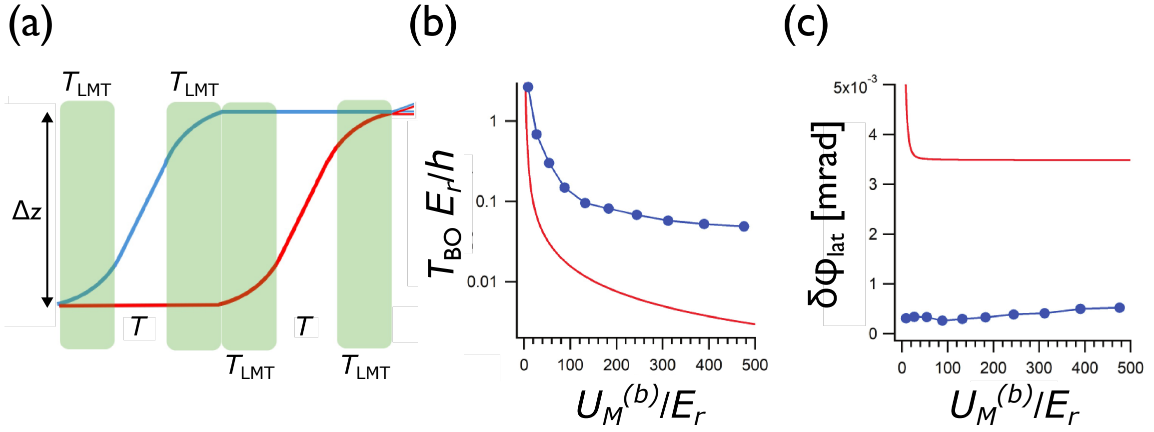

Figure 6.1: Large momentum transfer phase stability with Bloch oscillations. (a) Mach-Zehnder interferometer. In the first half, the top arm is accelerated and then decelerated by two LMT pulses (green shaded region). In the second half, the bottom arm receives the LMT pulses. (b) Bloch oscillation period required for 99.9% efficient pulses for ground band (line) and magic excited Bloch bands (points connected by a line). (c) The lattice-induced phase instability for ground band (line) and magic excited Bloch bands (points connected by a line) for the LMT pulses with $T_{\rm BO}$ in (b) and $\varepsilon = 0.5\%$ lattice depth variation.

ometer. Part of the reason is that the fidelity of momentum transfer suffers exponentially with the number of photon recoils. For example, a fidelity of 99.5% per $\hbar k$ results in $< 1\%$ overall transfer efficiency for $1000\hbar k$. Due to their adiabatic passage, Bloch oscillations offer very high-fidelity momentum transfer compared to other prevalent atom-optics techniques, e.g., Bragg pulses or Raman pulses. Although several BOs have been implemented in conjugate [73, 8] or twin lattice [74] interferometer designs, large momentum transfer within a phase-stable interferometer has been elusive on the hundreds of recoils scale. Without phase stability, it is possible to have good interferometer contrast, but not good visibility. For metrologically useful sensing, we require high-fidelity *and* phase-stable large momentum transfer techniques.

A Mach-Zehnder interferometer augmented with LMT acceleration pulses as shown in Fig. 6.1(a) would benefit from the phase stability of magic Bloch bands. The propagation phase is

$$\phi_{\mathrm{prop}} = gkN_{\mathrm{BO}}\left[T^2 + T_{\mathrm{LMT}}\left(2T_{\mathrm{LMT}} + T\right)\right] \,, \tag{6.1}$$

$$\Delta z = \frac{\hbar k}{M} N_{\mathrm{BO}}\left(2T_{\mathrm{LMT}} + T\right) \,, \tag{6.2}$$

where T_{LMT} is the duration of the N_{BO} Bloch oscillation acceleration pulse and T is the interrogation time of the interferometer. We saw that there is an infinite family of magic Bloch bands in Chapter 4 and that the magic depths $U_M^{(b)}$ grow with band number b. For the most part, Bloch oscillation fidelity grows monotonically with the Bloch oscillation period T_{BO}, except for the local extrema from Stückelberg phases discussed in Chapter 3. Taking all that together, we can calculate the Bloch oscillation period needed to achieve at least 99.9% per $2\hbar k$ for various magic Bloch bands, which yields an overall $\approx 60\%$ fidelity for $N_{\mathrm{BO}} = 500$ periods. Figure 6.1(b) shows the results for the first ten excited bands. The lattice-induced phase instability $\delta\phi_{\mathrm{lat}}$, for ground band LMT pulses at a range of lattice depths and magic depth BOs is shown in Fig. 6.1(c) for the respective BO period T_{BO} to achieve 99.9% fidelity.

Considering that the LMT pulses take a duration of $T_{\mathrm{LMT}} = N_{\mathrm{BO}}T_{\mathrm{BO}}$, we would like to limit atom loss due to spontaneous scattering. The spontaneous scattering rate in the lattice—see Eq. (2.10)—then determines the relative detuning Δ/Γ needed for the LMT pulses. We choose the $U_M^{(b=5)} = 132E_r$ magic depth, with $T_{\text{BO}} = 0.095E_r/h \approx 26\,\mu\text{s}$, to minimize the detuning needed to achieve at least 99.9% per BO survival probability from spontaneous scattering during LMT pulses. The detuning required is at least $|\Delta| \approx 8 \times 10^4\Gamma \approx 2\pi \times 14.4\,\text{GHz}$. The resulting overall survival is at least 99.8% per BO period, which leads to an overall survival of 13.5% after the interferometer. The propagation phase (6.1) provides a pathway toward a resolution of $\delta g/g \sim 10^{-8}$ per shot for T_{LMT} described above with $T = 10\,\text{ms}$ and $\Delta z = 7.3\,\text{cm}$ for an interferometer with $< 100\,\text{mrad}$ phase instability.

The phase response due to lattice vibrations or other environmental considerations *during* the LMT Bloch oscillation pulse requires some further exploration with the $T_{\text{LMT}} \sim 10\,\text{ms}$ pulse durations discussed above. For example, variance in the lattice tilt angle could induce transverse motion of atomic ensembles during LMT pulse, leading to lattice depth variation across the atomic ensemble [119]. The subsequent dephasing may also be suppressed by magic Bloch bands.

6.1.1 Magic Wannier-Stark states

In our calculations of magic depths, we have only been considering small accelerations. However, in Chapter 3, we saw that for an optical lattice with large accelerations, the Wannier-Stark picture provides a reliable description of the tunneling dynamics during Bloch oscillation, resulting in losses. The acceleration becomes large as the corresponding Bloch oscillation frequency approaches the lattice depth $h\nu_B \sim U_0$. In the supplementary material of Fitzek et al. (Ref [62]), the authors employ the Wannier-Stark description to calculate the average depth for various accelerations. They found that the magic depth of the first-excited Wannier Stark ladder state increases with larger acceleration (see Fig. 6.2). In Chapter 4, we understood that the magic depth corresponds to the highest bound band of an optical lattice potential.

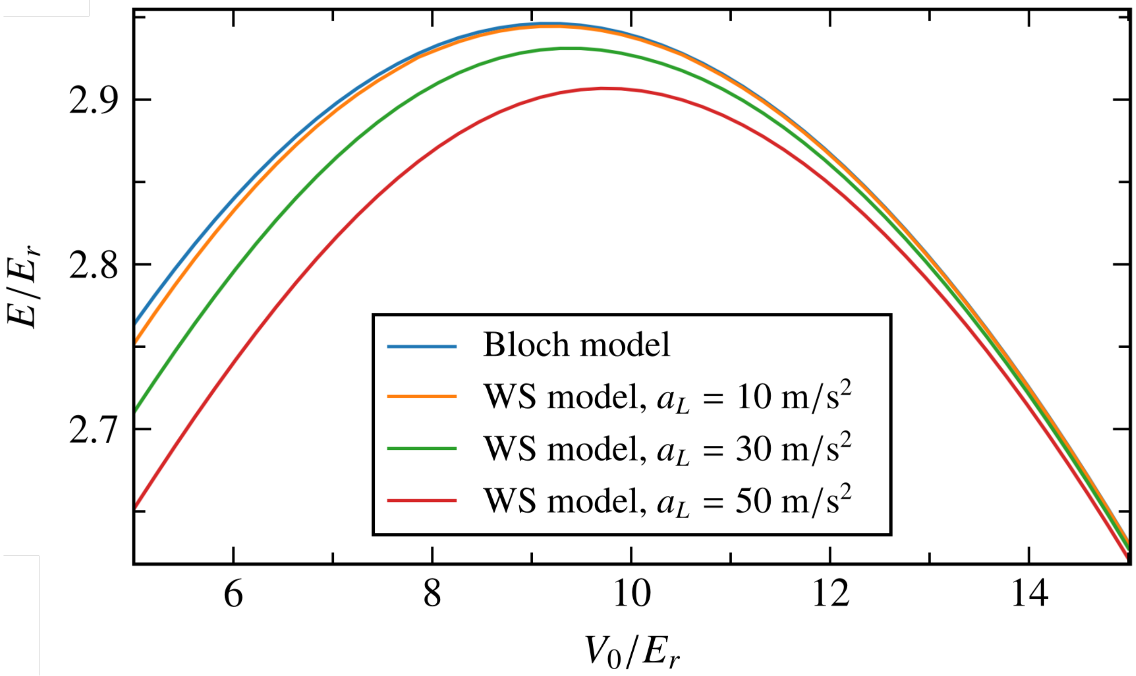

Figure 6.2: From Supplementary material of Fitzek et al. 2024. The Wannier-Stark energy E for a range of lattice depths V_0 and for various accelerations a_L of the first excited ladder state which corresponds to the first excited band in the Bloch model in the limit of zero acceleration.

Trap duration	Magic depth	Δ/Γ	Power per beam	Survival per BO
0.1 s	$U_M^{(1)} = 9.2E_r$	9×10^3	$4.7\,\mathrm{mW}$	> 0.99
1 s	$U_M^{(1)} = 9.2E_r$	1.8×10^5	$95\,\mathrm{mW}$	> 0.999
10 s	$U_M^{(2)} = 27.3E_r$	5.3×10^6	$8.28\,\mathrm{W}$	> 0.9999

Table 6.1: Magic lattice-trapped atom interferometer settings required for various trap durations for ytterbium. The optical lattice is assumed to be made of two counterpropagating collimated Gaussian beams with $550\,\mu$m waist and $d \sim 278\,$nm lattice spacing.

For larger accelerations, i.e., larger tilts, this band may no longer be bound. The lattice depth would therefore need to increase in order to restore this characteristic feature of magic Bloch bands. Notably, the magic depth does not change much from the acceleration due to gravity on Earth ($h\nu_B \approx 0.32E_r$ for ytterbium in a $d = 278\,$nm optical lattice). Especially for faster accelerations, the Wannier-Stark picture allows for a more accurate determination of magic depths.

6.2 Lattice-Trapped Atom Interferometry

In Chapter 5, we investigated the effect of magic depth on a lattice-trapped interferometer. We found preliminary evidence that magic Bloch bands protect against dephasing effects in the lattice trap. This results in larger overall visibility than for atoms trapped in the ground band at the same lattice depth, suggesting that magic Bloch band operation could provide better measurement precision for gravity. The precision scales linearly with trap duration, so for high-precision measurements, long-lived Bloch oscillations are required. The fidelity for $b = 1$ and $b = 2$ Bloch oscillations is > 0.9995 per BO and > 0.99995 per BO at their respective magic depths. Numerical simulations shown in Fig. 6.3 suggest that the fidelity per BO does not get better

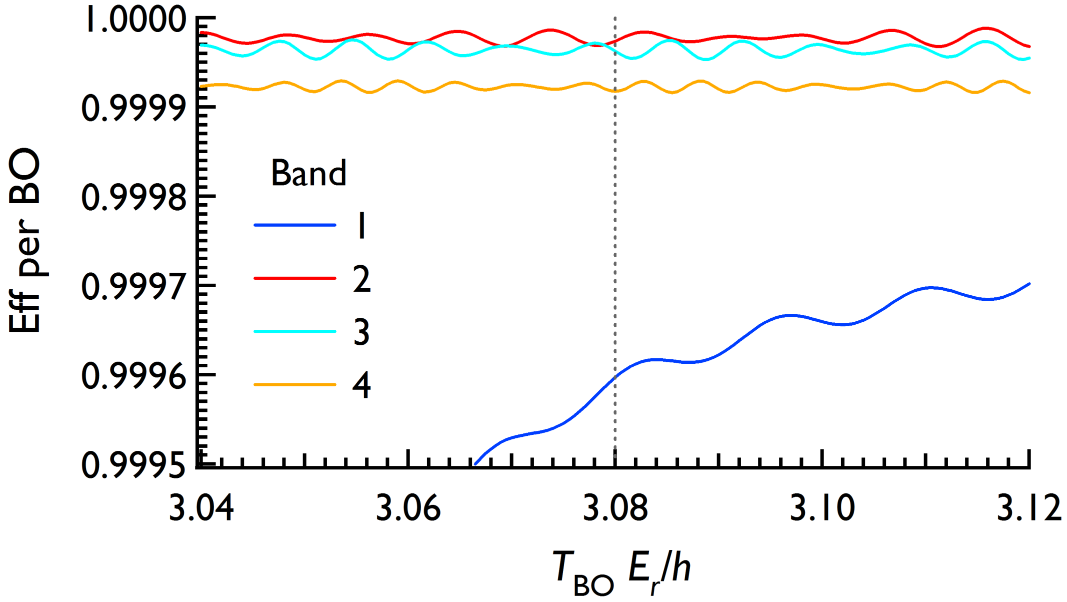

Figure 6.3: Per BO efficieny curves (solid lines) for magic depths $U_M^{(b)}$ of the first four excited bands calculated for T_{BO} near $g = 9.8\,\mathrm{m/s^2}$ (vertical dashed line). Small oscillations are artifacts from a finite number of BO periods. The overall trend for $b = 1$ is from the proximity to a nearby high-order Stückelberg resonance around $T_{\mathrm{BO}} \approx 3h/E_r$ for this depth.

for Bloch oscillations in higher magic Bloch bands, with $b = 2$ having the best fidelity. We consider a range of trap durations in the first column of Table 6.1. The detunings Δ listed in the table provide the minimum scattering rate needed for the overall survival rate in the last column, which results in $> 30\%$ overall survival at the end of the interferometer. For the $\Gamma_G = 2\pi \times 182\,\mathrm{ms}^{-1}$ intercombination line in ytterbium, the largest detuning in the table corresponds to a 2 nm smaller wavelength.

The best fidelities for magic depth Bloch bands suggest that trap durations much larger than 10 s ($N_{\mathrm{BO}} = 11962$ for ytterbium in a $d = 278\,\mathrm{nm}$ lattice) are out of reach. For example, a 100 s trap duration at the best fidelities could only yield an overall survival of just a few percent. The standard quantum-limited resolution on a gravity measurement would be

$$\frac{\delta g}{g} = \frac{\delta \nu_B}{\nu_B} = \frac{\sqrt{1/N_{\mathrm{atoms}}}/C^{(b)}}{2\pi \times (\nu_B \tau_{\mathrm{Bloch}})(\Delta z/d)}\,, \tag{6.3}$$

where the numerator consists of the number of measured atoms N_{atoms} and the visibility $C^{(b)}$ in the interference signal. The denominator is the phase evolution between the separated wavepackets during the trap (see Eq. (5.9)). We consider the resolution per shot from Eq. (6.3) given a $\tau_{\mathrm{Bloch}} = 10\,\mathrm{s}$ trap duration. Our current BEC production typically yields $\gtrsim 10,000$ atoms that participate in the interferometer with a best visibility of $C^{(b)} \approx 0.4$. We consider a $1/e$ drop in visibility and the atom number with wavepackets separated by $\Delta z = 50d$ after a 10 s trap duration. The resulting resolution in gravity is $\delta g/g \sim 10^{-8}$ per shot or about one order of magnitude smaller than the current state of the art with lattice-trapped interferometry [9] with comparable wavepacket separations and trap durations. It should be noted that operation of the optical lattice in the last row of Table 6.1 would require much higher optical lattice intensities than our laser sources are capable of providing. At present, the Gaussian beam waist of our lattice beams is $550\,\mu\mathrm{m}$, which means that each beam would need $< 8.3\,\mathrm{W}$ of power for 2 nm detuning and a 10 s trap duration. A smaller waist would lower the demand in power, e.g., 4.2 W is sufficient if each beam has a

400 μm waist.

Notably, recent demonstrations of *continuously* trapped interferometry in magic Bloch bands [120] offer another approach to MLTAI with ultracold atoms. As discussed in Chapter 3, Stückeleberg phases arise from the energy difference between Bloch bands and the Bloch oscillation period $T_{\mathrm{BO}} \equiv \nu_B^{-1}$. Similarly, atoms in Floquet-Bloch bands are sensitive to Stückelberg phases. The existence of magic Floquet-Bloch bands offers a compelling direction for interferometry within a lattice. The trapped propagation phase scales with T_{BO} in such interferometers, making them especially suitable for precision sensing of small forces.

Finally, we can envision inserting acceleration and deceleration pulses in between the beamsplitter pulses of the lattice-trapped interferometer. Such a hybrid design would improve the independent control over the spatial and temporal interferometer scales. Inserting LMT techniques may yield larger wavepacket separations than would be otherwise possible. For example, Eq. (6.2) suggests centimeter-scale wavepacket separations are achievable using the same LMT parameters described in the previous section for $b = 5$ magic Bloch bands. Alternatively, centimeter-scale separations are achievable with 99.9% per BO survival in $b = 2$ magic Bloch bands for $T_{\mathrm{BO}} = 0.683h/E_r$ and $N_{\mathrm{BO}} = 100$ pulses, giving a comparable T_{LMT} for the $b = 5$ case. Although still compact, such interferometers could yield $\delta g/g \sim 10^{-11}$ with a 10 s trap durations in a standard quantum limited interferometer.

6.3 Applications for Precision Inertial Sensors

We have so far considered two approaches to precision sensing of inertial effects using compact phase-stable atom interferometers. The first is based on a well-trodden approach of using pulsed atom-optics tools for large momentum transfer via fast Bloch oscillations. The second is a more novel approach utilizing atom-optics to trap matterwaves and benefit from long-lived Bloch oscillations. The two approaches have a trade-off between sensor size and sensor bandwidth. In the previous sections, we considered magic Bloch band parameters that could yield precision measurements of local gravity at the 10^{-8} level per shot on the respective space-time scales of $\sim 10\,\mathrm{cm}$–$10\,\mathrm{ms}$ and $\sim 10\,\mu\mathrm{m}$–$10\,\mathrm{s}$ for lattice-pulsed and lattice-trapped interferometers. Both methods offer a promising method towards phase-stable interferometry. Furthermore, large momentum transfer techniques can be applied to long-baseline interferometers for further enhancement. Let us now consider a couple of examples where we can leverage these atom-optics techniques towards advancements in inertial sensing.

The equivalence principle is one of the conceptual foundations underlying general relativity. It states that *local* effects due to gravity can always be attributed to an accelerating frame rather than a gravitational force. In other words, gravity is fundamentally geometric and a consequence of this principle is the universality of free fall in classical physics [121]. Tests of this universality are called weak equivalence principle tests and are typically quantified by the Eötvös parameter

$$\eta = \frac{|a_1 - a_2|}{|a_1 + a_2|}, \tag{6.4}$$

where $a_i \approx g$ for the i^{th} test mass. The Eötövs parameter $\eta \equiv 0$ if and only if the universality of free fall holds exactly. Therefore, any deviations from $\eta = 0$ show a violation of a fundamental tenet of geometric gravity theories and may help with the reconciliation of gravity and quantum mechanics [122]. The best measurements using atom interferometers show that the equivalence principle holds within $\eta \lesssim 10^{-12}$ rubidium light-pulsed interferometers [7]. However, state-of-the-art measurements with macroscopic test bodies [123, 124] outshine the most sensitive atom interferometry measurements by a few orders of magnitude. Efficient and stable kilorecoil momentum transfer techniques may offer a much-needed boost to atom interferometer precision measurements. In addition, effects from the coupling of the gravitational force to quantum mechanical degrees of freedom are of particular interest. The various stable isotopes of ytterbium have either a $I = 0, 1/2, \text{or}\, 5/2$ nuclear spin component and $L = S = 0$ in the ground state. Tests of the equivalence principle with particles of different spin bound the Eötvös parameter $\eta \lesssim 10^{-7}$ in strontium isotopes by measuring the frequency of Bloch oscillations [16] and atom interferometers with rubidium prepared in different hyperfine levels [125]. These measurements also bound the coupling strength of intrinsic spin to gravity [126, 127].

Beyond tests of gravity, atom interferometers can be operated as inertial sensors for measuring accelerations and forces in general. Compact atomic sensors onboard transport vessels open the door to inertial navigation on Earth and "GPS-denied" navigation [99]. In the latter case, transport with land, water, air, or outer space vehicles would require dead-reckoning capabilities. This is achievable through a combination of accelerometers and gyroscopes, so that the velocity of the vehicle can be measured repeatedly. For geodesy, atom interferometers paired with a precise, high-resolution gravitational atlas [128] could be used to determine position without a GPS. For long voyages, such as deep space travel, highly accurate and stable positioning and timing systems must be applied in tandem, because even small inaccuracies could lead to a large accumulation in trajectory error. Atom interferometers in space have already been used for pathfinding experiments onboard the International Space Station [129]. Realizing the full power of inertial sensing on Earth or in space requires high precision, accuracy, and stability [130]. With meticulous control of pristine atomic systems in exquisitely engineered optical lattice fields, atom interferometry provides an exciting platform towards local inertial sensing for fundamental physics and navigation.

BIBLIOGRAPHY

[1] L. Marton, J. A. Simpson, and J. A. Suddeth, "Electron beam interferometer," *Phys. Rev.*, vol. 90, pp. 490–491, May 1953.

[2] H. Rauch, W. Treimer, and U. Bonse, "Test of a single crystal neutron interferometer," *Physics Letters A*, vol. 47, pp. 369–371, Apr. 1974.

[3] LIGO Scientific Collaboration and Virgo Collaboration, "Gw150914: The advanced ligo detectors in the era of first discoveries," *Phys. Rev. Lett.*, vol. 116, p. 131103, Mar. 2016.

[4] R. Geiger, A. Landragin, S. Merlet, and F. Pereira Dos Santos, "High-accuracy inertial measurements with cold-atom sensors," *AVS Quantum Science*, vol. 2, p. 024702, Jun. 2020.

[5] X. Guo, Z. Yu, F. Wei, S. Jin, X. Chen, X. Li, X. Zhang, and X. Zhou, "Quantum precision measurement of two-dimensional forces with 10-28-newton stability," *Science Bulletin*, vol. 67, pp. 2291–2297, Nov. 2022.

[6] Z.-K. Hu, B.-L. Sun, X.-C. Duan, M.-K. Zhou, L.-L. Chen, S. Zhan, Q.-Z. Zhang, and J. Luo, "Demonstration of an ultrahigh-sensitivity atom-interferometry absolute gravimeter," *Phys. Rev. A*, vol. 88, p. 043610, Oct. 2013.

[7] P. Asenbaum, C. Overstreet, M. Kim, J. Curti, and M. A. Kasevich, "Atom-interferometric test of the equivalence principle at the 10^{-12} level," *Phys. Rev. Lett.*, vol. 125, p. 191101, Nov. 2020.

[8] L. Morel, Y. Zhao, P. Clade, and S. Guellati-Khelifa, "Determination of the fine-structure constant with an accuracy of 81 parts per trillion," *Nature*, vol. 588, p. 61, Dec. 2020.

[9] C. D. Panda, M. J. Tao, M. Ceja, J. Khoury, G. M. Tino, and H. Müller, "Measuring gravitational attraction with a lattice atom interferometer," *Nature*, vol. 631, pp. 515–520, Jul. 2024.

[10] O. Carnal and J. Mlynek, "Young's double-slit experiment with atoms: A simple atom interferometer," *Phys. Rev. Lett.*, vol. 66, pp. 2689–2692, May 1991.

[11] D. W. Keith, C. R. Ekstrom, Q. A. Turchette, and D. E. Pritchard, "An interferometer for atoms," *Phys. Rev. Lett.*, vol. 66, pp. 2693–2696, May 1991.

[12] M. Kasevich and S. Chu, "Atomic interferometry using stimulated raman transitions," *Phys. Rev. Lett.*, vol. 67, pp. 181–184, Jul. 1991.

[13] M. Ben Dahan, E. Peik, J. Reichel, Y. Castin, and C. Salomon, "Bloch Oscillations of Atoms in an Optical Potential," *Phys. Rev. Lett.*, vol. 76, p. 4508, Jun. 1996.

[14] S. Wilkinson, C. Bharucha, K. Madison, Q. Niu, and M. G. Raizen, "Observation of Atomic Wannier-Stark Ladders in an Accelerating Optical Potential," *Phys. Rev. Lett.*, vol. 76, p. 4512, Jun. 1996.

[15] N. Poli, F. Wang, M. Tarallo, A. Alberti, M. Prevedelli, and G. Tino, "Precision Measurement of Gravity with Cold Atoms in an Optical Lattice and Comparison with a Classical Gravimeter," *Phys. Rev. Lett.*, vol. 106, p. 038501, Jan. 2011.

[16] M. Tarallo, T. Mazzoni, N. Poli, X. Zhang, D. Sutyrin, and G. Tino, "Test of Einstein Equivalence Principle for 0-Spin and Half-Integer-Spin Atoms: Search for Spin-Gravity Coupling Effects," *Phys. Rev. Lett.*, vol. 113, p. 023005, 2014.

[17] R. H. Parker, C. Yu, B. Estey, W. Zhong, and H. Muller, "Measurement of the fine-structure constant as a test of the Standard Model," *Science*, vol. 360, p. 191, Apr. 2018.

[18] F. Bloch, "Uber die Quantenmechanik der Elektronen in Kristallgitter," *Z Phys*, vol. 52, p. 555, 1928.

[19] D. Giltner, R. McGowan, and S. Lee, "Theoretical and experimental study of the Bragg scattering of atoms from a standing light wave," *Phys. Rev. A.*, vol. 52, p. 3966, Nov. 1995.

[20] D. Gochnauer, K. McAlpine, B. Plotkin-Swing, A. Jamison, and S. Gupta, "Bloch-band picture for light-pulse atom diffraction and interferometry," *Phys. Rev. A.*, vol. 100, p. 043611, Oct. 2019.

[21] C. K. Kirkendall and A. Dandridge, "Overview of high performance fibre-optic sensing," *Journal of Physics D: Applied Physics*, vol. 37, p. R197, Sept. 2004.

[22] R. Charrière, M. Cadoret, N. Zahzam, Y. Bidel, and A. Bresson, "Local gravity measurement with the combination of atom interferometry and Bloch oscillations," *Physical Review A*, vol. 85, p. 013639, Jan. 2012.

[23] N. M. R. Hoque and L. Duan, "A Mach-Zehnder Fabry-Perot hybrid fiber-optic interferometer operating at the thermal noise limit," *Scientific Reports*, vol. 12, Jul. 2022.

[24] C. D. Panda, M. Tao, J. Egelhoff, M. Ceja, V. Xu, and H. Müller, "Coherence limits in lattice atom interferometry at the one-minute scale," *Nature Physics*, vol. 20, pp. 1234–1239, Aug. 2024.

[25] B. Plotkin-Swing, *Large Momentum Separation Matter Wave Interferometry.* PhD thesis, University of Washington, 2018.

[26] K. E. McAlpine, *Advancing Atom Interferometry with a Bloch-bands Approach.* PhD thesis, University of Washington, 2019.

[27] D. Gochnauer, *Vertical Contrast Interferometry and Bloch-Band Approach to Atom Optics.* PhD thesis, University of Washington, 2020.

[28] M. Kaiser, J. Grimmel, L. Torralbo-Campo, M. Mack, F. Karlewski, F. Jessen, N. Schopohl, and J. Fortágh, "Observation of the motional stark shift in low magnetic fields," *Phys. Rev. A*, vol. 96, p. 043401, Oct. 2017.

[29] N. Hinkley, J. A. Sherman, N. B. Phillips, M. Schioppo, N. D. Lemke, K. Beloy, M. Pizzocaro, C. W. Oates, and A. D. Ludlow, "An atomic clock with 10^{-18} instability," *Science*, vol. 341, pp. 1215–1218, Aug. 2013.

[30] H. N. Hausser, J. Keller, T. Nordmann, N. M. Bhatt, J. Kiethe, H. Liu, I. M. Richter, M. von Boehn, J. Rahm, S. Weyers, E. Benkler, B. Lipphardt, S. Dörscher, K. Stahl, J. Klose, C. Lisdat, M. Filzinger, N. Huntemann, E. Peik, and T. E. Mehlstäubler, "^{115}in^{+}–^{172}yb^{+} coulomb crystal clock with 2.5×10^{-18} systematic uncertainty," *Phys. Rev. Lett.*, vol. 134, p. 023201, Jan. 2025.

[31] K. Ono, Y. Saito, T. Ishiyama, T. Higomoto, T. Takano, Y. Takasu, Y. Yamamoto, M. Tanaka, and Y. Takahashi, "Observation of nonlinearity of generalized king plot in the search for new boson," *Phys. Rev. X*, vol. 12, p. 021033, May 2022.

[32] M. Door, C.-H. Yeh, M. Heinz, F. Kirk, C. Lyu, T. Miyagi, J. C. Berengut, J. Bieroń, K. Blaum, L. S. Dreissen, S. Eliseev, P. Filianin, M. Filzinger,

E. Fuchs, H. A. Fürst, G. Gaigalas, Z. Harman, J. Herkenhoff, N. Huntemann, C. H. Keitel, K. Kromer, D. Lange, A. Rischka, C. Schweiger, A. Schwenk, N. Shimizu, and T. E. Mehlstäubler, "Probing new bosons and nuclear structure with ytterbium isotope shifts," *Phys. Rev. Lett.*, vol. 134, p. 063002, Feb. 2025.

[33] A. J. Shin, C. Zhao, Y. Shen, C. E. Dickerson, B. Li, H. Roshandel, D. Bím, T. L. Atallah, P. H. Oyala, Y. He, L. K. Alson, T. A. Kerr, A. N. Alexandrova, P. L. Diaconescu, W. C. Campbell, and J. R. Caram, "Toward liquid cell quantum sensing: Ytterbium complexes with ultranarrow absorption," *Science*, vol. 385, pp. 651–656, Aug. 2024.

[34] S. Ma, A. P. Burgers, G. Liu, J. Wilson, B. Zhang, and J. D. Thompson, "Universal gate operations on nuclear spin qubits in an optical tweezer array of ^{171}Yb atoms," *Phys. Rev. X*, vol. 12, p. 021028, May 2022.

[35] Y. Nakamura, T. Kusano, R. Yokoyama, K. Saito, K. Higashi, N. Ozawa, T. Takano, Y. Takasu, and Y. Takahashi, "Hybrid atom tweezer array of nuclear spin and optical clock qubits," *Phys. Rev. X*, vol. 14, p. 041062, Dec. 2024.

[36] M. Iqbal, N. Tantivasadakarn, R. Verresen, S. L. Campbell, J. M. Dreiling, C. Figgatt, J. P. Gaebler, J. Johansen, M. Mills, S. A. Moses, J. M. Pino, A. Ransford, M. Rowe, P. Siegfried, R. P. Stutz, M. Foss-Feig, A. Vishwanath, and H. Dreyer, "Non-Abelian topological order and anyons on a trapped-ion processor," *Nature*, vol. 626, pp. 505–511, Feb. 2024.

[37] B. Plotkin-Swing, A. Wirth, D. Gochnauer, T. Rahman, K. McAlpine, and S. Gupta, "Crossed-beam slowing to enhance narrow-line ytterbium magneto-optic traps," *Rev. Sci. Instr.*, vol. 91, p. 093201, Sept. 2020.

[38] B. Seo, P. Chen, Z. Chen, W. Yuan, M. Huang, S. Du, and G.-B. Jo, "Efficient production of a narrow-line erbium magneto-optical trap with two-stage slowing," *Phys. Rev. A*, vol. 102, p. 013319, Jul. 2020.

[39] W. Lunden, L. Du, M. Cantara, P. Barral, A. Jamison, and W. Ketterle, "Enhancing the capture velocity of a Dy magneto-optical trap with two-stage slowing," *Phys. Rev. A*, vol. 101, p. 063403, Jun. 2020.

[40] K. Shibata, H. Ikeda, R. Suzuki, and T. Hirano, "Compensation of gravity on cold atoms by a linear optical potential," *Phys. Rev. Research*, vol. 2, p. 013068, Jan. 2020.

[41] D. Gochnauer, T. Rahman, A. Wirth, and S. Gupta, “Interferometry in an Atomic Fountain with ytterbium Bose-Einstein condensates,” *Atoms*, vol. 9, p. 58, Aug. 2021.

[42] R. Roy, A. Green, R. Bowler, and S. Gupta, “Rapid cooling to quantum degeneracy in dynamically shaped atom traps,” *Phys. Rev. A.*, vol. 93, p. 043403, Apr. 2016.

[43] J. Stenger, S. Inouye, A. P. Chikkatur, D. M. Stamper-Kurn, D. E. Pritchard, and W. Ketterle, “Bragg spectroscopy of a bose-einstein condensate,” *Phys. Rev. Lett.*, vol. 82, pp. 4569–4573, Jun. 1999.

[44] C. Kasik, “Constructing a saturated absorption spectroscopy system for laser locking,” research experiences for undergraduates paper, University of Washington, 2018.

[45] R. Maruyama, *Optical trapping of ytterbium atoms.* PhD thesis, University of Washington, 2003.

[46] R. C. Tolman and T. D. Stewart, “The electromotive force produced by the acceleration of metals,” *Phys. Rev.*, vol. 8, pp. 97–116, Aug. 1916.

[47] T. Rahman, A. Wirth-Singh, A. Ivanov, D. Gochnauer, E. Hough, and S. Gupta, “Bloch oscillation phases investigated by multipath stückelberg atom interferometry,” *Phys. Rev. Res.*, vol. 6, p. L022012, Apr. 2024.

[48] C. Zener, “Non-Adiabatic Crossing of Energy Levels,” *Proc. R. Soc. London A*, vol. 137, p. 696, 1932.

[49] E. C. G. Stuckelberg, “Theory of inelastic collisions between atoms,” *Helvetica Physica Acta*, vol. 5, p. 369, 1932.

[50] W. Oliver, Y. Yu, J. Lee, K. Berggren, L. Levitov, and T. Orlando, “Mach-zehnder interferometry in a strongly driven superconducting qubit,” *Science*, vol. 310, p. 1653, Dec. 2005.

[51] T. Ota, K. Hitachi, and K. Muraki, “Landau-zener-stückelberg interference in coherent charge oscillations of a one-electron double quantum dot,” *Science Reports*, vol. 8, p. 5491, Apr. 2008.

[52] K. Hughes, J. Burke, and C. Sackett, “Suspension of atoms using optical pulses, and application to gravimetry,” *Phys. Rev. Lett.*, vol. 102, p. 150403, Apr. 2009.

[53] M. Robert-de Saint-Vincent, J.-P. Brantut, C. J. Borde, A. Aspect, T. Bourdel, and P. Bouyer, “A quantum trampoline for ultra-cold atoms,” *Europhys. Lett.*, vol. 89, p. 10002, Jan. 2010.

[54] J. Hecker-Denschlag, J. E. Simsarian, H. Haffner, C. McKenzie, A. Browaeys, D. Cho, K. Helmerson, S. Rolston, and W. D. Phillips, “A Bose-Einstein condensate in an optical lattice,” *J. Phys. B.*, vol. 35, p. 3095, Jul. 2002.

[55] K. McAlpine, D. Gochnauer, and S. Gupta, “Excited-band Bloch oscillations for precision atom interferometry,” *Phys. Rev. A.*, vol. 101, p. 023614, Feb. 2020.

[56] A. Zenesini, D. Ciampini, O. Morsch, and A. E., “Observation of Stückelberg oscillations in accelerated optical lattices,” *Phys. Rev. A*, vol. 82, p. 065601, Dec. 2010.

[57] S. Shevchenko, S. Ashhab, and F. Nori, “Landau–zener–stückelberg interferometry,” *Phys. Rep.*, vol. 492, p. 1, Mar. 2010.

[58] N. Vitanov, “Transition times in the Landau-Zener model,” *Phys. Rev. A*, vol. 59, p. 988, Feb. 1999.

[59] O. Ivakhnenko, S. Shevchenko, and F. Nori, “Nonadiabatic landau–zener–stückelberg–majorana transitions, dynamics, and interference,” *Phys. Rep.*, vol. 995, p. 1, Nov. 2023.

[60] L. Deng, E. W. Hagley, J. Deschlag, J. Simsarian, M. Edwards, C. Clark, K. Helmerson, S. L. Rolston, and W. D. Phillips, “Temporal, matter-wave-dispersion talbot effect,” *Phys. Rev. Lett.*, vol. 83, p. 5407, Dec. 1999.

[61] F. L. Moore, J. C. Robinson, C. F. Bharucha, B. Sundaram, and M. G. Raizen, “Atom optics realization of the quantum δ-kicked rotor,” *Phys. Rev. Lett.*, vol. 75, pp. 4598–4601, Dec. 1995.

[62] F. Fitzek, J.-N. Kirsten-Siemß, E. M. Rasel, N. Gaaloul, and K. Hammerer, “Accurate and efficient bloch-oscillation-enhanced atom interferometry,” *Phys. Rev. Res.*, vol. 6, p. L032028, Aug. 2024.

[63] S. Kling, T. Salger, C. Grossert, and M. Weitz, “Atomic bloch-zener oscillations and stückelberg interferometry in optical lattices,” *Phys. Rev. Lett.*, vol. 105, p. 215301, Nov. 2010.

[64] S. R. Wilkinson, C. F. Bharucha, M. C. Fischer, K. W. Madison, P. R. Morrow, Q. Niu, B. Sundaram, and M. G. Raizen, “Experimental evidence for non-exponential decay in quantum tunnelling,” *Nature*, vol. 387, pp. 575–577, Jun. 1997.

[65] P. Cladé, M. Andia, and S. Guellati-Khélifa, “Improving efficiency of bloch oscillations in the tight-binding limit,” *Phys. Rev. A*, vol. 95, p. 063604, Jun. 2017.

[66] Y. Castin and R. Dum, “Bose-Einstein Condensates in Time Dependent Traps,” *Phys. Rev. Lett.*, vol. 77, p. 5315, Dec. 1996.

[67] M. Glück, A. R. Kolovsky, and H. J. Korsch, “Wannier–stark resonances in optical and semiconductor superlattices,” *Physics Reports*, vol. 366, pp. 103–182, Feb. 2002.

[68] G. Tino and M. Kasevich, *Atom Interferometry, Proceedings of the International School of Physics “Enrico Fermi”*. IOS Press, 2014.

[69] M. Kozuma, L. Deng, E. Hagley, J. Wen, R. Lutwak, K. Helmerson, S. Rolston, and W. Phillips, “Coherent splitting of bose-einstein condensed atoms with optically induced bragg diffraction,” *Phys. Rev. Lett.*, vol. 82, p. 871, Feb. 1999.

[70] S. Gupta, A. E. Leanhardt, A. D. Cronin, and D. E. Pritchard, “Coherent Manipulation of Atoms with Standing Light Waves,” *Cr. Acad. Sci. IV-Phys*, vol. 2, p. 479, Apr. 2001.

[71] M. Cadoret, E. de Mirandes, P. Clade, S. Guellati-Khelifa, C. Schwob, F. Nez, L. Julien, and F. Biraben, “Combination of Bloch Oscillations with a Ramsey-Borde Interferometer: New Determination of the Fine Structure Constant,” *Phys. Rev. Lett.*, vol. 101, p. 230801, Dec. 2008.

[72] G. McDonald, C. Kuhn, S. Bennetts, J. Debs, K. Hardman, M. Johnsson, J. Close, and N. Robins, “80$\hbar k$ momentum separation with Bloch oscillations in an optically guided atom interferometer,” *Phys. Rev. A*, vol. 88, p. 053620, Nov. 2013.

[73] Z. Pagel, W. Zhing, R. H. Parker, C. T. Olund, N. Y. Yao, C. Yu, and H. Muller, “Symmetric Bloch oscillations of matter waves,” *Phys. Rev. A*, vol. 102, p. 053312, Nov. 2020.

[74] M. Gebbe, S. Abend, S. Jan-Niclas, M. Gersemann, H. Ahlers, H. Müntinga, S. Herrmann, N. Gaaloul, C. Schubert, K. Hammerer, C. Lämmerzahl, W. Ertmer, and E. Rasel, "Twin-lattice atom interferometry," *Nature Communications*, vol. 12, p. 2544, May 2021.

[75] P. Clade, S. Guellati-Khelifa, F. Nez, and F. Biraben, "Large Momentum Beam Splitter Using Bloch Oscillations," *Phys. Rev. Lett.*, vol. 102, p. 240402, Jun. 2009.

[76] H. Muller, S. Chiow, S. Herrmann, and S. Chu, "Atom Interferometers with Scalable Enclosed Area," *Phys. Rev. Lett.*, vol. 102, p. 240403, Jul. 2009.

[77] B. Plotkin-Swing, D. Gochnauer, K. McAlpine, E. Cooper, A. Jamison, and S. Gupta, "Three-Path Atom Interferometry with Large Momentum Separation," *Phys. Rev. Lett.*, vol. 121, p. 133201, Sept. 2018.

[78] L. Lim, J. Fuchs, and G. Montambaux, "Mass and Chirality Inversion of a Dirac Cone Pair in Stückelberg Interferometry," *Phys. Rev. Lett.*, vol. 112, p. 155302, Apr. 2014.

[79] T. Wilkason, M. Nantel, J. Rudolph, Y. Jiang, B. Garber, H. Swan, S. Carman, M. Abe, and J. Hogan, "Atom Interferometry with Floquet Atom Optics," *Phys. Rev. Lett.*, vol. 129, p. 183202, Oct. 2022.

[80] T. A. Zheng, Y. A. Yang, M. S. Safronova, U. I. Safronova, Z.-X. Xiong, T. Xia, and Z.-T. Lu, "Magic wavelengths of the yb $(6s^2\ {}^1s_0 - -6s6p\ {}^3p_1)$ intercombination transition," *Phys. Rev. A*, vol. 102, p. 062805, Dec. 2020.

[81] I. Ushijima, M. Takamoto, and H. Katori, "Operational magic intensity for sr optical lattice clocks," *Phys. Rev. Lett.*, vol. 121, p. 263202, Dec. 2018.

[82] A. Aeppli, A. Chu, T. Bothwell, C. J. Kennedy, D. Kedar, P. He, A. M. Rey, and J. Ye, "Hamiltonian engineering of spin-orbit–coupled fermions in a wannier-stark optical lattice clock," *Science Advances*, vol. 8, p. eadc9242, Oct. 2022.

[83] M. Abramowitz and I. A. Stegun, *Handbook of Mathematical Functions ed*, ch. 20. New York: Dover, 1970.

[84] T. R. Carver, "Mathieu's functions and electrons in a periodic lattice," *American Journal of Physics*, vol. 39, pp. 1225–1230, Oct. 1971.

[85] R. Coïsson, G. Vernizzi, and X. Yang, "Mathieu functions and numerical solutions of the mathieu equation," in *2009 IEEE International Workshop on Open-source Software for Scientific Computation (OSSC)*, pp. 3–10, 2009.

[86] I. Kovacic, R. Rand, and S. Mohamed Sah, "Mathieu's equation and its generalizations: Overview of stability charts and their features," *Applied Mechanics Reviews*, vol. 70, p. 020802, Feb. 2018.

[87] M. Holthaus, "Floquet engineering with quasienergy bands of periodically driven optical lattices," *Journal of Physics B: Atomic, Molecular and Optical Physics*, vol. 49, p. 013001, Nov. 2015.

[88] M. Arzamasovs and B. Liu, "Tight-binding tunneling amplitude of an optical lattice," *European Journal of Physics*, vol. 38, p. 065405, Oct. 2017.

[89] Y. Jia, S. Du, and A. A. Seshia, "Twenty-Eight Orders of Parametric Resonance in a Microelectromechanical Device for Multi-band Vibration Energy Harvesting," *Scientific Reports*, vol. 6, p. 30167, Jul. 2016.

[90] L. Huang, S. M. Soskin, I. A. Khovanov, R. Mannella, K. Ninios, and H. B. Chan, "Frequency stabilization and noise-induced spectral narrowing in resonators with zero dispersion," *Nature Communications*, vol. 10, p. 3930, Sept. 2019.

[91] B. Dubetsky and M. A. Kasevich, "Atom interferometer as a selective sensor of rotation or gravity," *Phys. Rev. A*, vol. 74, p. 023615, Aug. 2006.

[92] J. K. Stockton, K. Takase, and M. A. Kasevich, "Absolute geodetic rotation measurement using atom interferometry," *Phys. Rev. Lett.*, vol. 107, p. 133001, Sept. 2011.

[93] L. Badurina, E. Bentine, D. Blas, K. Bongs, D. Bortoletto, T. Bowcock, K. Bridges, W. Bowden, O. Buchmueller, C. Burrage, J. Coleman, G. Elertas, J. Ellis, C. Foot, V. Gibson, M. Haehnelt, T. Harte, S. Hedges, R. Hobson, M. Holynski, T. Jones, M. Langlois, S. Lellouch, M. Lewicki, R. Maiolino, P. Majewski, S. Malik, J. March-Russell, C. McCabe, D. Newbold, B. Sauer, U. Schneider, I. Shipsey, Y. Singh, M. Uchida, T. Valenzuela, M. v. d. Grinten, V. Vaskonen, J. Vossebeld, D. Weatherill, and I. Wilmut, "Aion: an atom interferometer observatory and network," *Journal of Cosmology and Astroparticle Physics*, vol. 2020, p. 011, May 2020.

[94] MAGIS-100 Collaboration, “Matter-wave atomic gradiometer interferometric sensor (magis-100),” *Quantum Science and Technology*, vol. 6, p. 044003, Jul. 2021.

[95] B. Canuel, A. Bertoldi, L. Amand, E. Pozzo di Borgo, T. Chantrait, C. Danquigny, M. Dovale Álvarez, B. Fang, A. Freise, R. Geiger, J. Gillot, S. Henry, J. Hinderer, D. Holleville, J. Junca, G. Lefèvre, M. Merzougui, N. Mielec, T. Monfret, S. Pelisson, M. Prevedelli, S. Reynaud, I. Riou, Y. Rogister, S. Rosat, E. Cormier, A. Landragin, W. Chaibi, S. Gaffet, and P. Bouyer, “Exploring gravity with the MIGA large scale atom interferometer,” *Scientific Reports*, vol. 8, p. 14064, Sept. 2018.

[96] M.-S. Zhan, J. Wang, W.-T. Ni, D.-F. Gao, G. Wang, L.-X. He, R.-B. Li, L. Zhou, X. Chen, J.-Q. Zhong, B. Tang, Z.-W. Yao, L. Zhu, Z.-Y. Xiong, S.-B. Lu, G.-H. Yu, Q.-F. Cheng, M. Liu, Y.-R. Liang, P. Xu, X.-D. He, M. Ke, Z. Tan, and J. Luo, “Zaiga: Zhaoshan long-baseline atom interferometer gravitation antenna,” *International Journal of Modern Physics D*, vol. 29, p. 1940005, Mar. 2020.

[97] B. Canuel et al., “Elgar—a european laboratory for gravitation and atom-interferometric research,” *Classical and Quantum Gravity*, vol. 37, p. 225017, Oct. 2020.

[98] TVLBAI Proto-Collaboration, “Long-Baseline Atom Interferometry.” arXiv, Apr. 2025.

[99] F. A. Narducci, A. T. Black, and J. H. Burke, “Advances toward fieldable atom interferometers,” *Advances in Physics: X*, vol. 7, p. 1946426, Mar. 2022.

[100] E. R. Moan, R. A. Horne, T. Arpornthip, Z. Luo, A. J. Fallon, S. J. Berl, and C. A. Sackett, “Quantum rotation sensing with dual sagnac interferometers in an atom-optical waveguide,” *Phys. Rev. Lett.*, vol. 124, p. 120403, Mar. 2020.

[101] Y.-J. Wang, D. Z. Anderson, V. M. Bright, E. A. Cornell, Q. Diot, T. Kishimoto, M. Prentiss, R. A. Saravanan, S. R. Segal, and S. Wu, “Atom michelson interferometer on a chip using a bose-einstein condensate,” *Phys. Rev. Lett.*, vol. 94, p. 090405, Mar. 2005.

[102] L. Qi, Z. Hu, T. Valenzuela, Y. Zhang, Y. Zhai, W. Quan, N. Waltham, and J. Fang, “Magnetically guided cesium interferometer for inertial sensing,” *Applied Physics Letters*, vol. 110, p. 153502, Apr. 2017.

[103] J. Rudolph, W. Herr, C. Grzeschik, T. Sternke, A. Grote, M. Popp, D. Becker, H. Müntinga, H. Ahlers, A. Peters, C. Lämmerzahl, K. Sengstock, N. Gaaloul, W. Ertmer, and E. M. Rasel, "A high-flux bec source for mobile atom interferometers," *New Journal of Physics*, vol. 17, p. 065001, Jun. 2015.

[104] Y. Shin, M. Saba, T. A. Pasquini, W. Ketterle, D. E. Pritchard, and A. E. Leanhardt, "Atom interferometry with bose-einstein condensates in a double-well potential," *Phys. Rev. Lett.*, vol. 92, p. 050405, Feb. 2004.

[105] X. Zhang, R. Del Aguila, T. Mazzoni, N. Poli, and G. Tino, "Trapped-atom interferometer with ultracold Sr atoms," *Phys. Rev. A*, vol. 94, p. 043608, Oct. 2016.

[106] V. Xu, M. Jaffe, C. Panda, S. Kristensen, L. Clark, and H. Muller, "Probing gravity by holding atoms for 20 seconds," *Science*, vol. 366, p. 745, Nov. 2019.

[107] P. Cladé, S. Guellati-Khélifa, C. Schwob, F. Nez, L. Julien, and F. Biraben, "A promising method for the measurement of the local acceleration of gravity using bloch oscillations of ultracold atoms in a vertical standing wave," *Europhysics Letters*, vol. 71, p. 730, Aug. 2005.

[108] D. Carney, P. C. E. Stamp, and J. M. Taylor, "Tabletop experiments for quantum gravity: a user's manual," *Classical and Quantum Gravity*, vol. 36, p. 034001, Jan. 2019.

[109] D. Carney, H. Müller, and J. M. Taylor, "Using an atom interferometer to infer gravitational entanglement generation," *PRX Quantum*, vol. 2, p. 030330, Aug. 2021.

[110] M. Jaffe, *Atom Interferometry in an Optical Cavity.* PhD thesis, University of California, Berkeley, 2018.

[111] C. D. Panda, M. Tao, M. Ceja, A. Reynoso, and H. Müller, "Atomic gravimeter robust to environmental effects," *Applied Physics Letters*, vol. 123, p. 064001, Oct. 2023.

[112] C. Henkel, P. Krüger, R. Folman, and J. Schmiedmayer, "Fundamental limits for coherent manipulation on atom chips," *Applied Physics B*, vol. 76, pp. 173–182, Feb. 2003.

[113] R. Piccon, S. Sarkar, J. Gomes Baptista, S. Merlet, and F. Pereira Dos Santos, "Separating the output ports of a bragg interferometer via velocity selective transport," *Phys. Rev. A*, vol. 106, p. 013303, Jul. 2022.

[114] E. Peik, M. Ben Dahan, I. Bouchoule, Y. Castin, and C. Salomon, "Bloch oscillations of atoms, adiabatic rapid passage, and monokinetic atomic beams," *Phys. Rev. A*, vol. 55, pp. 2989–3001, Apr. 1997.

[115] Z. Geiger, K. Fujiwara, K. Singh, R. Senaratne, S. Rajagopal, M. Lipatov, T. Shimasaki, R. Driben, V. Konotop, T. Meier, and D. Weld, "Observation and Uses of Position-Space Bloch Oscillations in an Ultracold Gas," *Phys. Rev. Lett.*, vol. 120, p. 213201, May 2018.

[116] B. Young, M. Kasevich, and S. Chu, "- precision atom interferometry with light pulses," in *Atom Interferometry* (P. R. Berman, ed.), pp. 363–406, San Diego: Academic Press, 1997.

[117] M. Kasevich and S. Chu, "Measurement of the gravitational acceleration of an atom with a light-pulse atom interferometer," *Applied Physics B*, vol. 54, pp. 321–332, May 1992.

[118] K. Mehling, M. Holland, and C. LeDesma, "High-Precision Phase Control of an Optical Lattice with up to 50 dB Noise Suppression." arXiv:2504.13264 [physics], Apr. 2025.

[119] F. Fitzek, *Theory of Atom Interferometry based on Bragg Diffraction and Bloch Oscillations.* PhD thesis, Leibniz University Hannover, 2024.

[120] X. Chai, J. L. Tanlimco, E. Nolasco-Martinez, X. Liang, E. Q. Simmons, E. Zhu, R. Sajjad, H. Mas, S. N. Halawani, and D. M. Weld, "Continuously trapped matter-wave interferometry in magic Floquet-Bloch band structures." arXiv:2506.11881 [physics], Jun. 2025.

[121] E. Okon and C. Callender, "Does quantum mechanics clash with the equivalence principle—and does it matter?," *European Journal for Philosophy of Science*, vol. 1, pp. 133–145, Jan. 2011.

[122] G. Tino, L. Cacciapuoti, S. Capozziello, G. Lambiase, and F. Sorrentino, "Precision gravity tests and the einstein equivalence principle," *Progress in Particle and Nuclear Physics*, vol. 112, p. 103772, Mar. 2020.

[123] S. Schlamminger, K.-Y. Choi, T. A. Wagner, J. H. Gundlach, and E. G. Adelberger, "Test of the equivalence principle using a rotating torsion balance," *Phys. Rev. Lett.*, vol. 100, p. 041101, Jan. 2008.

[124] P. Touboul, G. Métris, M. Rodrigues, Y. André, Q. Baghi, J. Bergé, D. Boulanger, S. Bremer, P. Carle, R. Chhun, B. Christophe, V. Cipolla, T. Damour, P. Danto, H. Dittus, P. Fayet, B. Foulon, C. Gageant, P.-Y. Guidotti, D. Hagedorn, E. Hardy, P.-A. Huynh, H. Inchauspe, P. Kayser, S. Lala, C. Lämmerzahl, V. Lebat, P. Leseur, F. m. c. Liorzou, M. List, F. Löffler, I. Panet, B. Pouilloux, P. Prieur, A. Rebray, S. Reynaud, B. Rievers, A. Robert, H. Selig, L. Serron, T. Sumner, N. Tanguy, and P. Visser, "Microscope mission: First results of a space test of the equivalence principle," *Phys. Rev. Lett.*, vol. 119, p. 231101, Dec. 2017.

[125] X.-C. Duan, X.-B. Deng, M.-K. Zhou, K. Zhang, W.-J. Xu, F. Xiong, Y.-Y. Xu, C.-G. Shao, J. Luo, and Z.-K. Hu, "Test of the universality of free fall with atoms in different spin orientations," *Phys. Rev. Lett.*, vol. 117, p. 023001, Jul. 2016.

[126] B. J. Venema, P. K. Majumder, S. K. Lamoreaux, B. R. Heckel, and E. N. Fortson, "Search for a coupling of the earth's gravitational field to nuclear spins in atomic mercury," *Phys. Rev. Lett.*, vol. 68, pp. 135–138, Jan. 1992.

[127] B. Mashhoon, "Gravitational couplings of intrinsic spin," *Classical and Quantum Gravity*, vol. 17, p. 2399, Jun. 2000.

[128] N. K. Pavlis, S. A. Holmes, S. C. Kenyon, and J. K. Factor, "The development and evaluation of the earth gravitational model 2008 (egm2008)," *Journal of Geophysical Research: Solid Earth*, vol. 117, p. 406, Apr. 2012.

[129] J. R. Williams, C. A. Sackett, H. Ahlers, D. C. Aveline, P. Boegel, S. Botsi, E. Charron, E. R. Elliott, N. Gaaloul, E. Giese, W. Herr, J. R. Kellogg, J. M. Kohel, N. E. Lay, M. Meister, G. Müller, H. Müller, K. Oudrhiri, L. Phillips, A. Pichery, E. M. Rasel, A. Roura, M. Sbroscia, W. P. Schleich, C. Schneider, C. Schubert, B. Sen, R. J. Thompson, and N. P. Bigelow, "Pathfinder experiments with atom interferometry in the Cold Atom Lab onboard the International Space Station," *Nature Communications*, vol. 15, p. 6414, Aug. 2024.

[130] V. Ménoret, P. Vermeulen, N. Le Moigne, S. Bonvalot, P. Bouyer, A. Landragin, and B. Desruelle, "Gravity measurements below $10^{-9}g$ with a transportable absolute quantum gravimeter," *Scientific Reports*, vol. 8, p. 12300, Aug. 2018.